Electrochemical Properties and Stability of Surface Layer on Lithium and Magnesium Metal Anodes

March, 2018

Hiroko Kuwata

Mie University

Contents

Contents

General Introduction

Requirement of rechargeable batteries with high energy density

Global warming which is a serious environmental issue gets even worse annually while counterplans are performed around a lot of countries of the world. The greenhouse emission resulting in the global warming is drained form various countries, and mostly occupied by the carbon dioxide (CO_2) because of using fossil fuels. In Japan, Ministry of the Environment reported that the amount of CO_2 emission was 1.4 G ton in 2013, increased in 10.8 % compared with the amount of CO_2 in 1990 [1]. Since a target of the amount of CO_2 in 2030 registered in the United Nations Framework Convention on Climate Change was established to 3.8 % decreasing by the 2005 ration [1], we must make efforts to decrease the CO_2 emission. In order to suppress the global warming, each department tackles the CO_2 decreasing. In the department of transportation, Hybrid vehicle (HV), Electric vehicle (EV) and Fuel cell hybrid vehicle (FCV) etc., called Eco-friendly cars have received increased attentions as Next-Generation Automobiles with superior energy efficiency. Particularly, EV contributes to the environmental issue because it relies on lithium-ion batteries instead of the fossil fuels. Fig. 1 shows a schematic representative of standard lithium-ion batteries [2]. The lithium-ion batteries are consisted by a graphite negative electrode and lithium

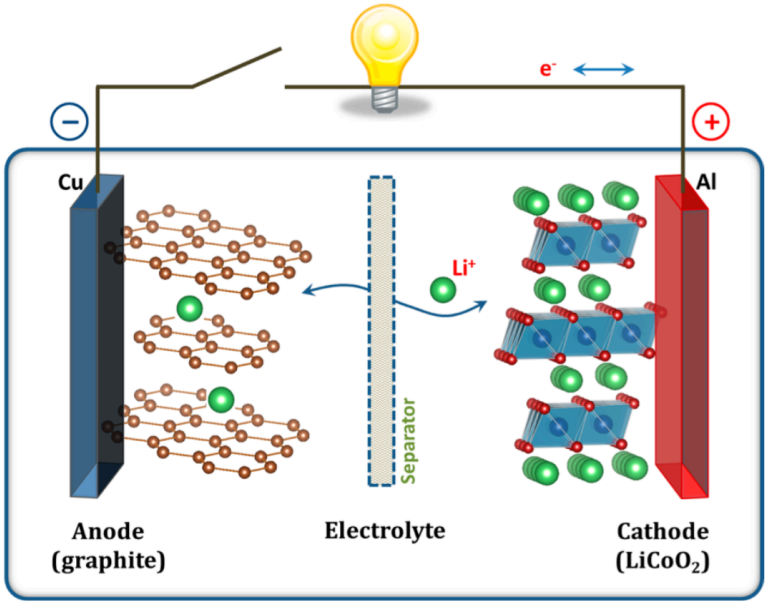

Fig. 1 Schematic representative of standard lithium-ion battery [2]

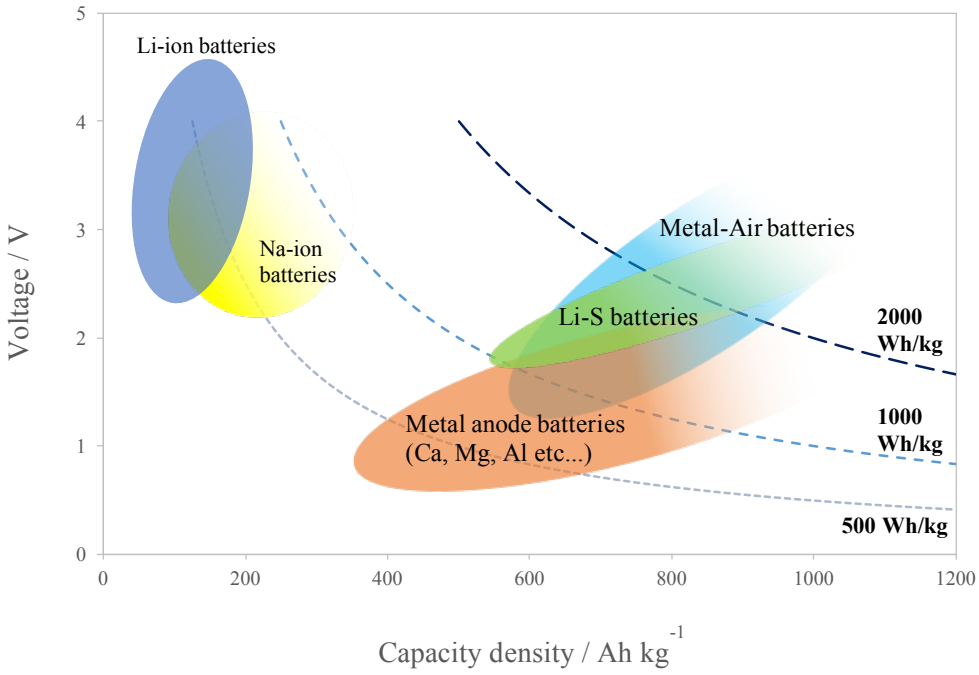

Fig. 2 Roadmap for beyond lithium-ion batteries [3]

transition metal oxide positive electrode, have energy density of approx. 240 Wh kg^{-1}.

However, as a technological problem for more popularization of the EV, the EV is able to drive only short distance per charging its batteries. According to the Battery roadmap 2013 reported by New Energy and Industrial Technology Development Organization (NEDO), it was considered that rechargeable batteries with energy density of > 700 Wh kg^{-1} are necessary to obtain the driving distance of 700 km by EV [3]. It suggests beyond lithium-ion batteries with high energy density are required for alternatively commercialized lithium-ion batteries.

One of approaches for the rechargeable batteries with high energy density is usage of metal anodes active materials taking highly theoretical capacity. A schematic representative of roadmap for the beyond lithium-ion batteries is shown in Fig. 2 [3]. The batteries of > 700 Wh kg^{-1} are rechargeable batteries with metal anode, Lithium-Sulfer battery and Lithium-Air battery, which consists of metal anode materials. Table I shows theoretical specific and volumetric capacity of the metal anodes. Especially, lithium (Li) metal and magnesium (Mg) metal are ideal anode active materials as the beyond lithium-ion batteries [4].

Li metal anode

Lithium metal is an ideal anode active material for rechargeable batteries because it has high energy density (3861 mAh g^{-1}, 2061 mAh cm^{-3}) and very negative reductive

Table I theoretical specific and volumetric capacity

Material	Specific capacity (mAh g^{-1})	Volumetric capacity (mAh cm^{-3})	Electrode potential (V vs. SHE)
Li	3861	2061	-3.05
Na	1165	1128	-2.71
Mg	2205	3832	-2.38
Ca	1337	2077	-2.87
Al	2980	8043	-1.67
C	372	841	-2.98～-2.82

potential (-3.05 V vs. SHE). In addition, the Li metal electrode provides 10 times higher specific capacity than that of graphite electrode for lithium ion batteries. Hence, the Li metal is expected as beyond lithium ion batteries.

The lithium metal anode has been studied by researchers since it was reported that the Li was stable in the non-aqueous electrolytes in the 1950s [5]. A lot of studies were conducted for lithium batteries, and the primary systems were commercialized in the late 1960s and 1970s. In the mid 1970s, the rechargeable lithium batteries were introduced by Whittingham [6]. It was demonstrated by cathode materials of a transition-metal oxide or chalcogenide which can be reversible lithium insertion: MnO_2, MoS_2 or TiS_2. Although the cathode materials showed sufficiently cycling performance, the Li metal of the anode materials has problems in cycling of deposition/dissolution process. One is formation of a whisker-shaped deposit in the cycling, another is formation of an isolated lithium deposit in the cycling. Fig. 3 shows the surface morphology of the whisker-shaped lithium deposit, called “dendrite lithium” and a schematic representative of the isolated lithium deposit, called “dead lithium” [7, 8]. The dendrite is easily formed in the lithium deposition process, grows toward the cathode materials, resulting in the short-circuit of the batteries. The dead lithium is formed by the dissolution process of the deposited lithium in the cycling, resulting in the reduction of the cycle life of the Li anode. Since both of the problems proceed from the formation of uneven deposit: dendritic lithium, it is necessary to prevent the dendritic growth of the lithium for commercializing a rechargeable battery containing a Li metal anode.

The surface morphology of the electrodeposited lithium is basically dependent

(a)

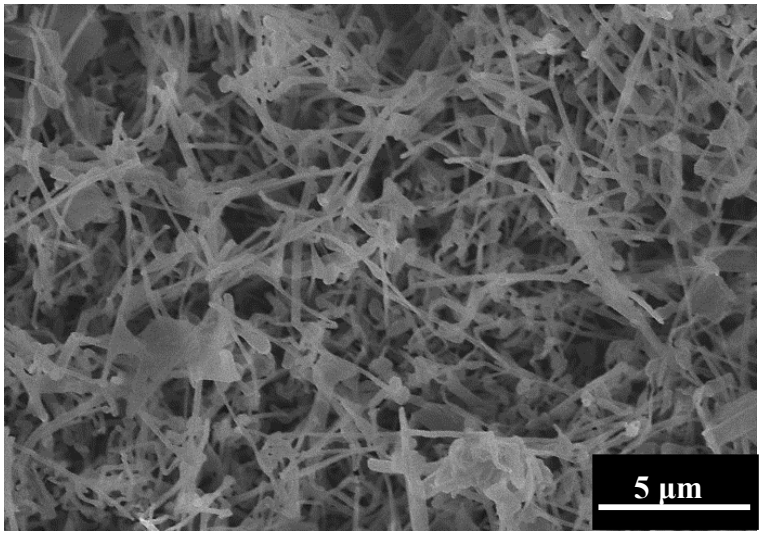

(b)

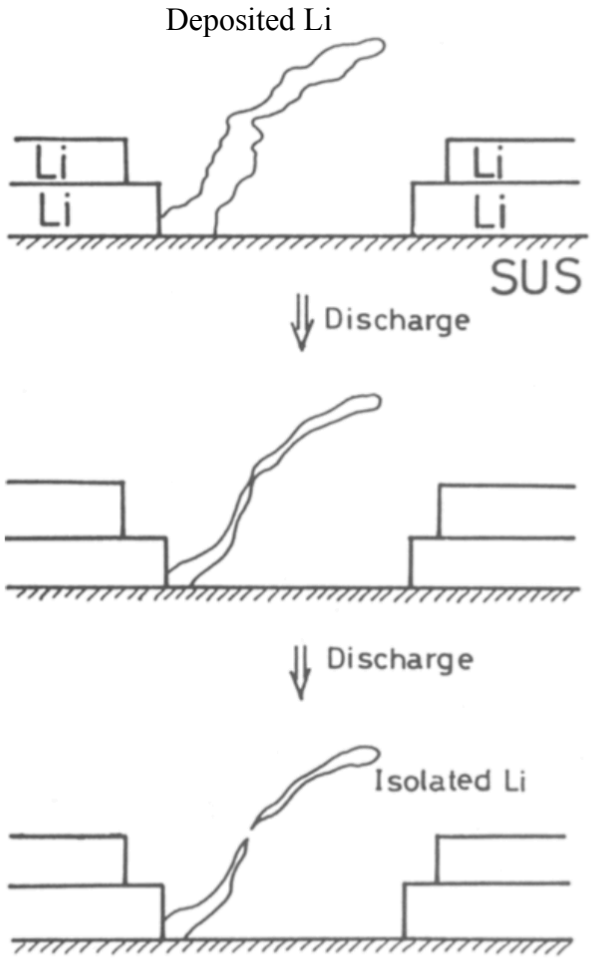

Fig. 3 SEM image of dendritic lithium (a) and schematic representative of dead(isolated) lithium (b) [7]

upon the kinetics of the deposition process [9] and the preferred crystal growth mode [10]. Especially the electrochemical reaction at the lithium / electrolyte solution interphase is the dominant process to determine the surface morphology, because lithium easily decomposes the electrolyte solution by its highly reductive ability, and forms surface film, called Solid electrolyte interphase (SEI) layer [11, 12]. A schematic representative of SEI layer model is shown in Fig. 4. The SEI layer consists of organic and inorganic compounds such as polymer, Li_2O and Li_2CO_3, and has only ionic conductivity because electrolyte solution is continuously decomposed if the SEI layer has electron conductivity. In other words, the SEI layer protects the electrolyte solution from the decomposition by highly reductive ability such as Li. Therefore, many analytical studies concerning the characterization of the SEI layer were carried out using various analytical techniques, such as FTIR [13-16], XPS [17-19], AFM [20-23] and so forth.

The SEI layer is also formed on the graphite electrode for lithium-ion batteries, plays an important role for lithiation/delithiation during charge/discharge process. The graphite electrode using ethylene carbonate (EC) -based electrolyte solution demonstrated reversible lithiation/delithiation, whereas the electrode using propylene carbonate (PC) -based electrolyte solution showed no-lithiation [24]. It is considered that the EC-based electrolyte solution forms effective SEI layer which suppresses more decomposition of the electrolyte solution under 1 V vs. Li/Li^+. However, the formation of SEI layer is caused by an irreversible capacity. Thus, electrolyte additives forming a stable SEI layer which suppresses decomposition of the electrolyte solution and prevents growth of surface film were investigated by researchers.

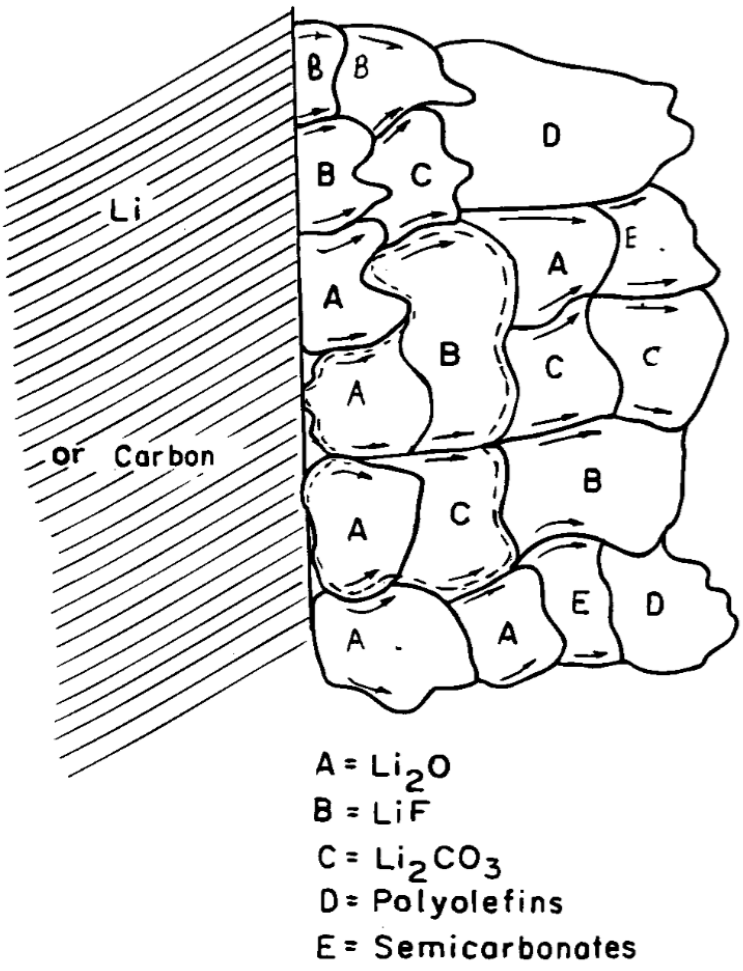

Fig. 4 Schematic representative of SEI layer model [12]

This approach was also applied to the lithium / electrolyte solution interphase for suppression of dendritic lithium. In order to form the stable SEI layer, various organic and inorganic electrolyte additives were investigated. A stable SEI layer of Li_2CO_3 is formed under the presence of CO_2 resulting in the decrease of the interfacial impedance and the improvement the cycling performance. Shiraishi et al. reported that the HF could be a good film formation additive to obtain a very smooth Li surface and showed improved cycling efficiency [25]. Typical film forming additives such as vinylene carbonate (VC), fluoroethylene carbonate (FEC), and ethylene sulfate (ES) developed for graphite negative electrode of lithium ion batteries, are also investigated. Mogi et al. reported that the FEC forms smooth surface morphology of electrodeposited lithium [21]. The VC forms a polymeric species and improves the cycling efficiency of lithium deposition and dissolution [26-28]. Sano et al. added VC and ES to a room temperature ionic liquid (RTIL) electrolyte and found the improved cycling performance [29]. Ding et al. obtained very smooth surface morphology of the electrodeposited lithium by adding small amount of $CsPF_6$ [30, 31]. Wang et al. added 1,3-dioxolane (DOL) to LiFSI-2tetraethylene glycol dimethyl ether (G4) and found a highly reversible dendrite-free lithium deposit [32]. Although these studies were performed for dendrite suppression, it is not well clarified that the relationship between the essential dendrite-free lithium deposit and the SEI layer.

Mg metal anode

Multivalent battery systems of less noble metal, such as aluminum, calcium and magnesium, have advantages in energy density. The Al has highly volumetric capacity of 8046 mAh•cm^{-3} because the Al ion is trivalent. Nevertheless, the standard electrode potential is -1.676 V vs. SHE, and limited of practical use. In contrast, the Ca has high volumetric capacity of 2077 mAh•cm^{-3} and the standard electrode potential of Ca/Ca^{2+} is -2.87 V vs. SHE, close to that of Li/Li^{+}. However, the deposition / dissolution process of calcium occurs on high temperature >50 ℃ [33]. The Mg provides also high volumetric capacity (3832 mAh•cm^{-3}), 1.9 time higher than that of Li, and the magnesium deposition / dissolution occurs at room temperature. Additionally, Mg metal anodes does not form the dendrite under the same condition of lithium deposition [34]. Fig. 5 shows surface morphologies of deposited magnesium and lithium in the same condition. Hence the magnesium batteries have received increased attention as beyond-lithium ion batteries because of improved safety by non-dendrite formation despite the standard electrode potential of Mg/Mg^{2+} 0.6 V higher potential than that of Li (-2.37 V vs. SHE).

There still remains a lot of challenges in utilization of the magnesium metal as a negative electrode, especially the choice of the electrolyte solution is critical to develop a practical battery system. The conventional ionic electrolyte solutions, such as magnesium perchlorate (ClO_4^-) or magnesium hexafluorophosphate (PF_6^-) dissolved in carbonate-based solvents, does not show the reversible deposition/dissolution of the

(a)

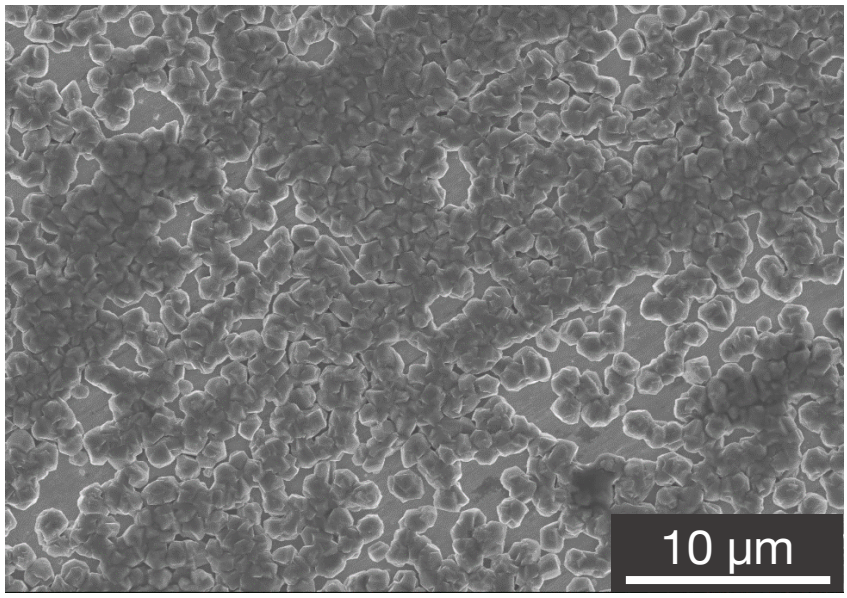

(b)

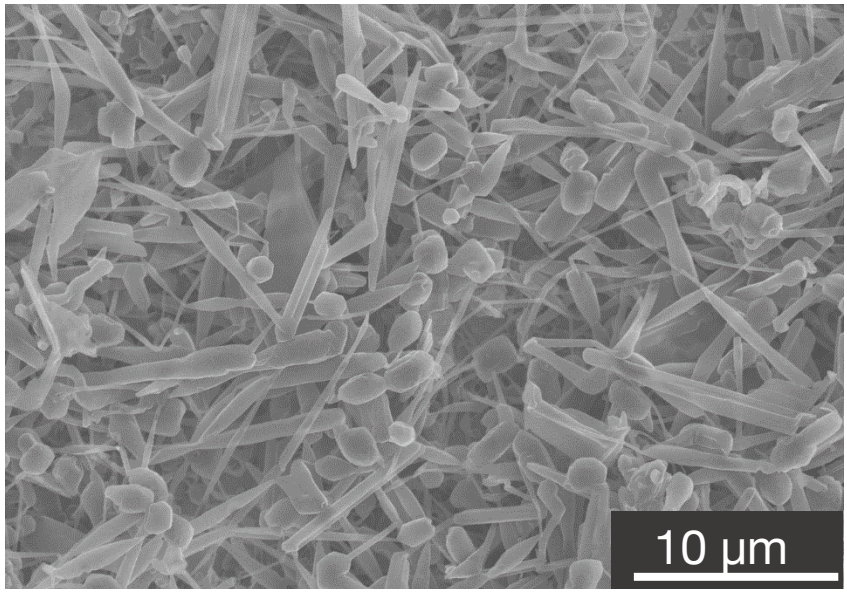

Fig. 5 SEM images of deposited Mg (a) and Li (b)
at 1 C cm^{-2} (1 mA cm^{-2}, 1000 sec)

magnesium metal, because a passivation layer is easily formed at the surface of the electrode [35, 36]. Therefore, the electrolyte design to avoid the formation of the passivation layer is necessary to utilize the advantage of the magnesium metal anode.

In 1920s, it was reported that the magnesium was electrodeposited by Grignard reagent in the ether solutions [37]. Then the Grignard reagent is well-known as the electrolyte solutions for the reversible magnesium deposition. In 1990s, Gregory *et al.* reported that electrolyte solutions, consist of the Grignard reagent and aluminum halides, were found to give Mg deposits with high purities of 99.99% [38]. Especially, the organomagensium chlorides were superior to the magnesium obtained from the organomagnesium bromides or iodides. However, the organomagnesium chlorides electrolyte solutions were insufficiently anodic stability (<1.5 V) for rechargeable magnesium batteries.

Based on his work, a development of the Grignard reagent-based electrolyte solution was carried out by Aurbach *et al*. in late 1990s and 2000s [35, 36, 39-43]. They used organohaloaluminate-based electrolyte solution, and demonstrated the high reversibility of magnesium deposition/dissolution. In addition, they also presented wider electrochemical window than previous studies (< 2.2 V), and showed that the very 1st prototype of the rechargeable magnesium battery using Mo_6S_8 Chevrel phase as a cathode active material [40]. Moreover, they optimized composition of the electrolyte solution, these electrolyte solutions show excellent reversibility and wide potential window > 3 V [44, 45]. Derived from the reaction in the organohaloaluminate-based electrolyte solutions, one is the exist of Lewis acid, another is the formation of the

electrochemically active products. It was reported that the Lewis acids of the organohaloaluminate-based electrolyte solutions contributed to the highly coulombic efficiency [38, 40]. Additionally, in an attempt to analyze the electrochemically active products, an inactive dimer complexes $(Mg_2(\mu\text{-}Cl)_3 \cdot 6THF)(EtAlCl_3)$ was formed in the electrolyte solutions [46, 47]. Even though these electrolytes have shown the stability of electrochemical oxidation and the high reversibility of magnesium deposition/dissolution, the organohaloaluminate-based electrolytes have corrosive properties at high electrode potential due to the halides [47, 48], especially the presence of chlorides in either/both cations and anions of the electrolytes. The corrosive properties could come about the dissolution of the active materials or current collector. Thus, the discovery of halide-free another electrolyte solution with wide electrochemical window is necessary for the rechargeable magnesium batteries.

Recently, the electrolyte solutions of chloride-free designs are discovered as alternate electrolyte solutions for the magnesium metal anode. Mohtadi *et al*. has reported that the electrolytes based on $Mg(BH_4)_2$ demonstrated reversible magnesium deposition/dissolution [49]. Furthermore, the high coulombic efficiency (94%) was observed in the electrolyte solution of $Mg(BH_4)_2$ in dimethoxyethane (DME) with $LiBH_4$ for an additive. On the other hand, the electrolyte solution had less stability of electrochemical oxidation (< 2.3 V). Electrolyte solution using magnesium bis(trifluoromethansulfonyl)amide: $Mg(TFSA)_2$ are also found as halide-free system for rechargeable magnesium batteries [50-52]. The conventional ionic electrolyte solution is fabricated by $Mg(TFSA)_2$ dissolved in ether-based solvents. The ionic electrolyte

solutions showed the magnesium deposition/dissolution process and the wide anodic electrochemical window (> 4 V vs Mg). The ionic electrolyte solutions take the place of the organohaloaluminate-based electrolyte solution at a glance, however the electrolyte solutions still have problems; high over potential > 1.0 V and poor coulombic efficiency < 60% at room temperature in the magnesium deposition / dissolution process.

Alloy-based anodes

A lot of R&Ds have carried out to study for the high capacity batteries as beyond lithium ion batteries. In negative electrode, lithium metal is a promising anode active material because of its highly theoretical capacity (>3400 $mAh \cdot g^{-1}$) and low standard electrode potential (-3.05 V vs. SHE) [4]. Nevertheless, the lithium easily forms dendrite deposit in the charging process [53], researchers were plagued by the dendrite formation resulting in the safety issue. The magnesium metal does not form the dendrite-shape deposits, however the choice of the electrolyte is limited because the organohaloaluminate-based electrolyte solutions have the safety issues, and the conventional electrolyte solutions shows high overpotential in the magnesium deposition / dissolution process. Hence, researches shifted to alloy-based anodes which are higher equilibrium potential than the potential of lithium and magnesium deposition.

In 1980s, the alloy-based anodes containing Al, Sn, and Si received increased

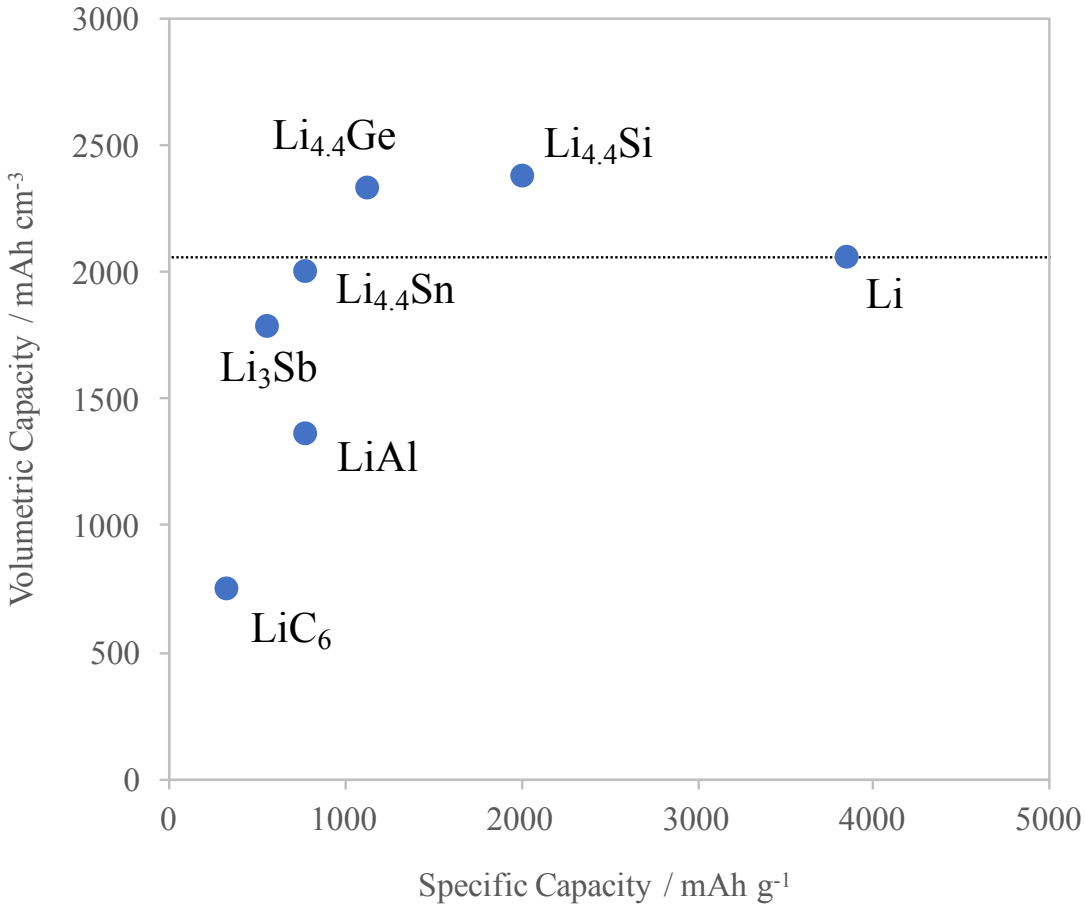

Fig. 6 Comparison with specific and volumetric capacity between alloy-based anode and lithium metal [58,59]

attention as new negative electrode materials for rechargeable lithium batteries because the volumetric capacity is higher than or as same as that of Li metal [54-57]. Fig. 6 shows a comparison with specific and volumetric capacity between alloy-based anode and lithium metal [58, 59]. Nevertheless, the alloy-based anodes have large volume changes, and carried out for the pulverization of the particle, resulting in a rapid capacity fade.

In order to improve the cycling performance of the alloy anode with high specific capacity, several approaches for the electrode design were tried. The simple and the most practical approach is utilization of new binder material such as carboxyl methyl cellulose (CMC) -styrene butadiene rubber (SBR) [60], alginate [61], poly acrylic acid (PAA) [62], polyimide [63] and so forth. Since these binder materials show high adhesive properties compared with polyvinylidenfluoride (PVdF), the active material particles are able to maintain electrical contact with conductive carbon and current collector even after pulverization of the particles. Another approach is micro- and nanostructural control using 1D or 2D nanomaterials [64-66], which show isotropic volume expansion to release the internal stress.

The electrode/electrolyte interphase is important aspect for the cycleability of the alloy anode, as well. Since redox potential of the anodes are typically <1.0 V vs. Li, SEI layer is formed during the charge/discharge process. In addition, since the surface area of the anode continuously changes accompanied with the volume expansion/shrinkage during the charge/discharge process, the SEI layer needs to be physically flexible. Several research group reported the spectroscopic study of the SEI

layer on the Si anode using FEC or VC as electrolyte additives [67-72]. Even with these characterization of the SEI layer, the required physical properties of the SEI layer is still not understood yet.

The alloy-based anodes are studied not only for Li ion batteries but also for Mg ion batteries [73-75]. Arthur et al. has reported that Mg intermetallic compounds of Sb and Bi phase, especially Mg_3Bi_2 anode showed highly cycling performance at 1 C rate in room temperature [73]. Singh et al. reported Mg was inserted to Sn at 0.002 C rate in room temperature, and found the Mg_2Sn anode [74]. Periyapperuma et al. showed Mg_2Pb phase is formed at sputtered Pb at 1/50C rate in 60 ℃ [75].

In the first place, the alloy-based anodes for magnesium-ion batteries is less reported compared with those anodes for the lithium-ion batteries, because of the passivation layer and a strongly ionic interaction with the Mg^{2+} ion. Since the passivation layer has no conductivity of Mg^{2+} cation in Mg battery system, the electrode / electrolyte interphase ought to keep a condition of no passivation layer. In addition, difficulty of smooth Mg^{2+} insertion/extraction in host compounds is due to the ionic interactions. Hence it suggests that the passivation layer and the bulk stability is due to different C rate and temperature for the magnesium insertion/extraction.

Outline of this study

In this thesis, surface analytical studies were performed for clarification of the relationship between stability of surface film and electrochemical properties so that I aim to obtain guidelines for utilization of metal anodes of the rechargeable lithium and magnesium batteries. The surface analyses were carries out by *in situ* FTIR spectroscopy and XPS spectroscopy, because the *in situ* FTIR and XPS are suitable tool for analysis of electrode / electrolyte interphase. Especially, the *in situ* FTIR spectroscopy can be catch a decomposition and formation process of materials at a voltage. In this thesis, the *in situ* FTIR spectroscopies were analyzed for decomposition process of electrolyte solutions and formation process of the surface film. The XPS spectroscopies were conducted for the analyses of the surface film. Furthermore, I expanded knowledges obtained by the surface analyses of the metal anodes to alloy-based anodes for the beyond lithium-ion batteries, and also aim to propose the material design guidelines for negative electrode / electrolyte solution interphase with good cycling performance.

In Chapter 1, the relationship between the SEI layer on the lithium metal and surface morphology of lithium deposit were investigated by using a standard electrolyte solution: 1 M $LiPF_6$ in Ethylene carbonate (EC) : Diethyl carbonate (DEC) (1:1 vol.%) and additives for lithium-ion batteries. In a graphite negative electrode for commercialized lithium-ion batteries, it is well known that the stable SEI layer formed by additives affected to improvement of the cycling performance [76, 77]. Hence, I

focused on the additives which form the stable SEI layer, examined how the SEI layer affect to the surface morphology of deposited lithium. Electrolyte solution of using the FEC as the additive maintained uniform surface morphology like the as-prepared lithium electrode. In addition, the XPS spectra for the electrolyte with the FEC additive showed a weak peak corresponding to LiF, which is formed by decomposed the electrolyte solution. Therefore, I obtained a knowledge that is necessary to suppress the decomposition of PF_6 anion and formation of the SEI layer. Furthermore, I constructed a new surface analysis method for the electrode / electrolyte interphase by *in situ* FTIR spectroscopy.

In Chapter 2, the effect of surface film was analyzed in the magnesium deposition / dissolution process. I performed a comparative study about the electrochemical properties by using two electrolyte solutions: the organohaloaluminate-based electrolyte solution and the conventional ionic electrolyte solution utilized a $Mg(TFSA)_2$ salts, discussed the relationship between the surface morphology and the surface film on the magnesium. The organohaloaluminate-based electrolyte solution showed a low overpotential of approximately 0.4 V in the magnesium deposition / dissolution process, demonstrated high coulombic efficiency of approx. 100 %. On the other hand, the ionic conventional electrolyte showed high overpotential of > 1 V, was poor coulombic efficiency of approx. 60 %. The electrolyte decomposition process was analyzed with *in situ* FTIR using the organohaloaluminate-based electrolyte solution and the conventional ionic electrolyte solution. The *in situ* FTIR spectra of the ionic electrolyte solution suggests that TFSA anion is decomposed at a positive potential above the

potential of the magnesium deposition. The XPS spectra of the magnesium immersed in the conventional ionic electrolyte showed a surface film formation by decomposed the TFSA anion. Hence, it was revealed that the decomposition of the electrolyte solution needs to be suppressed for the smooth electrochemical deposition / dissolution process of the magnesium metal.

In Chapter 3, the relationship between the surface layer on the lithium alloy-based anodes and cycling performance was investigated at the alloy-based anode electrode / electrolyte solution interphase. From chapter 1, suppression of the SEI layer is necessary to prevent the decomposition of the PF_6 anion. However, the $LiPF_6$ electrolyte solutions were decomposed not only solvents but also Li salts. In this study, I used $LiBH_4$ salt which has highly reductive stability. The *in situ* FTIR spectra showed the surface film is less formed in a 2 M $LiBH_4$ in THF electrolyte solution. The electrochemical properties were carried out for the investigation of the SEI layer effects in the lithium insertion/extraction (charging/discharging) process. Cycling tests of charging-discharging process were performed by half cells. Bismuth (Bi) powder with equilibrium potential of 0.8 V vs. Li/Li^+ was used as alloy-based anode active material, the lithium metal was used as counter electrode. After ten cycles of a 1C rate, the $LiPF_6$ electrolyte showed reversible capacity of 100 mAh g^{-1}. Aftert forty-five cycles of a 1 C rate, the electrolyte had poor reversible capacity of < 10 mAh g^{-1}. On the other hand, the reversible capacity of the Bi electrode using the $LiBH_4$ electrolyte was a theoretical capacity of 384 mAh g^{-1} after ten cycles. In addition, the capacity was 384 mAh g^{-1} even over forty-five cycles. Therefore, I showed the prevention of new SEI layer

formation in the lithium insertion/extraction process relates to the prolonged cyclability at high rate.

In Chapter 4, the effects of the surface stability on the magnesium intermetallic compounds and the bulk stability of materials were examined. The Mg_3Bi_2 and the Mg_3Sb_2 of the magnesium intermetallic compounds have same crystal structure. It was reported that the Mg_3Bi_2 shows reversible magnesium insertion/extraction in the conventional electrolyte solution using $Mg(TFSA)_2$, whereas the Mg_3Sb_2 were poor cyclability in the EAC electrolyte solution. From chapter 2, I found the formation of passivation layer prevents the smooth reaction in the magnesium deposition/dissolution process. Moreover, the diffusion of Mg^{2+} ion in host compounds is difficult because the Mg^{2+} ion has strongly ionic interaction. Hence, I consider that the differences were affected by the surface stability and the bulk condition of the Mg_3Bi_2 and the Mg_3Sb_2. Surface stability of the Mg_3Bi_2 and the Mg_3Sb_2 were investigated by time dependence changes using XRD. The XRD patterns of the Mg_3Bi_2 stored in air had a peak corresponding to bismuth, while the Mg_3Sb_2 maintained the same pattern in the air. It suggests that the Mg_3Bi_2 scarcely forms passivated layer at the surface of itself. Rietveld refinement results and the electron density distribution by MEM analysis showed Mg_3Bi_2 is relatively weak interaction between Mg cation and Bi anion at 2*d* site. Therefore, I think the activity of the Mg_3Bi_2 and the Mg_3Sb_2 is affected to not only the surface stability but also the bulk stability.

Chapter 1

Surface Layer and Morphology of Lithium Metal Electrodes

1-1. Introduction

Lithium metal has been considered as the ideal negative electrode material for these battery chemistries, because of its low equilibrium potential －3.05 V vs. SHE and high specific capacity >3800 $mAhg^{-1}$ [53]. However, rechargeable battery system using the lithium negative electrode has never been successfully commercialized due to the dendritic growth of lithium during the charging process. The lithium dendrite leads the internal short circuit of the cell resulting in the safety incidents, therefore the surface morphology control of the electrodeposited lithium is essential to utilize the lithium metal for practical battery systems.

The surface morphology of the electrodeposited lithium is basically dependent upon the kinetics of the deposition process [9] and the preferred crystal growth mode [10]. Especially the electrochemical reaction at the lithium-electrolyte interphase is the dominant process to determine the surface morphology. Therefore many analytical studies concerning the characterization of solid-electrolyte interphase (SEI) layer [11] were carried out using various analytical techniques, such as FTIR [13-16], XPS [17-19], AFM [20-23] and so forth.

In order to form the stable SEI layer, various organic and inorganic electrolyte additives were investigated. HF could be a good film formation additive to obtain a very smooth Li surface and showed improved cycling efficiency [25]. Typical fim forming additives such as vinylene carbonate (VC), fluoroetylence carbonate (FEC), and ethylene sulfate (ES) developed for graphite negative electrode of lithium ion batteries, are also investigated.

Despite of these works, it is not well understood that how these additives form the SEI layers and how the SEI affects to the surface morphology of the lithium metal yet. In the present study, an ethylene carbonate (EC)-based electrolyte solution was chosen as a normal electrolyte, because the EC-based electrolyte solution forms a good SEI layer on the graphite anode. I investigated the influence of the film-forming additives FEC, VC and LiBOB in the EC-based electrolyte solution. The SEI films on the lithium negative electrode were characterized using XPS and ATR-FTIR.

1-2. Experimental

A commercial electrolyte solution: 1 mol dm^{-3} $LiPF_6$ EC:DEC 1:1 vol.% (Kishida, battery grade) was used as the normal electrolyte solution in the present work. FEC, VC and LiBOB purchased from Kishida, were mixed into the normal electrolyte as the electrolyte additives in the argon filled glove box. The water content of the electrolyte solutions were < 10 ppm.

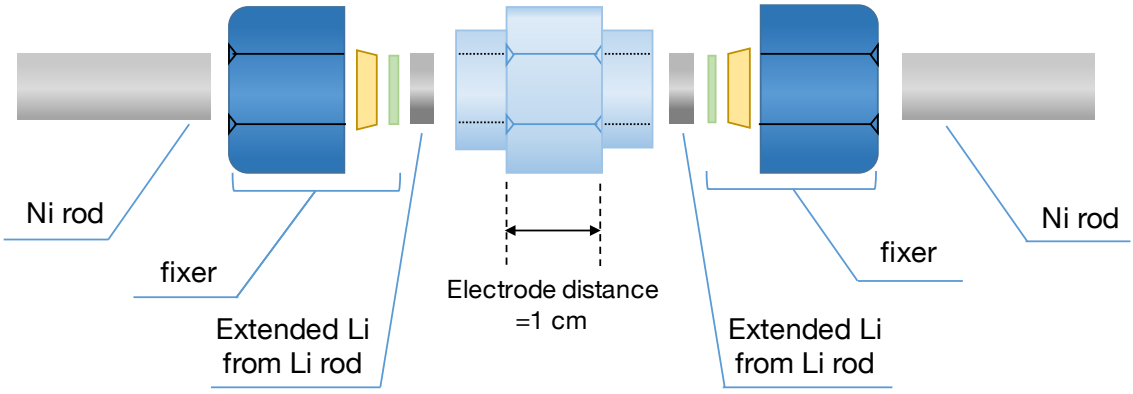

Fig. 1-1 A schematic representative of the two-electrode Swagelok cell.

Li deposition tests were conducted, using a two-electrode symmetric Swagelok cell. The distance between the two-electrode is 10.0 mm as shown in Fig. 1-1. Li metal electrodes were used as the working electrode and the counter electrode. In order to remove the Li_2CO_3 native film, a piece of Li metal was cut off from a Li rod (Honjo metal), and sandwiched between two sheets of a polypropylene (PP). Then the Li metal was pressed to form a sheet using a stainless steel hand roller. The Li sheet was punched and layered with Ni substrate to use as the electrode.

Galvanostatic Li deposition tests were carried out with time control mode. The Li deposition amount was determined to 10 $C \cdot cm^{-2}$ (1 $mAcm^{-2}$ for 10,000 sec.). After the electrodeposition of Li, the cell was disassembled and the electrode was rinsed with anhydrous DEC to remove the electrolyte salts. The rinsed electrodes were dried in vacuum for 5 minutes at room temperature. The obtained electrode was sealed in an airtight sample holder and transferred to Scanning Electron Microscope (SEM) for surface morphology observation.

The characterization of the SEI layer was conducted using XPS (ESCA-3400, Shimadzu) equipped with Mg K α X-ray anodes (Acceleration voltage 10 kV, Emission currents 20 mA) and argon sputtering gun. The argon sputtering of the samples were carried out to collect the depth information of SEI layer. The sample installation of the XPS measurement was carried out using a transfer vessel, which allows to insert the Li metal into the XPS chamber without exposing in air. The surface of the lithium metal was also analyzed by ATR-FTIR spectroscopy using a conventional FTIR spectrometer (Nicolet iS50R, Thermo Scientific) with a single reflection diamond ATR accessory

(Golden Gate ATR, Specac). The Li metal was placed on the diamond crystal in the Ar filled glovebox and pressed with an anvil with environmental chamber to avoid the air exposure of the sample.

1-3. Results and Discussion

1-3-1. Surface morphology and SEI layer in the additive-free electrolyte solution

SEM images of the electrodeposited lithium metal negative electrodes from an additive-free electrolyte solution (1 mol·dm^{-3} $LiPF_6$ EC:DEC = 1:1 vol.%), are shown in Fig. 1-2. During the early stage of the deposition process: 1 C·cm^{-2}, the lithium negative electrode maintained a smooth surface morphology Fig. 1-2 (b), similar to the as-prepared one shown in Fig. 1-2 (a). No uneven deposit is observed on the electrode even in the magnified image Fig. 1-2 (e). On the other hand, the lithium negative electrode after the electrodeposition process for 10 C·cm^{-2} had an uneven surface covered with aggregated lithium particles as shown in Fig. 1-2 (c). The aggregated particles consist of round-shaped particles and rods as shown in the magnified image: Fig. 1-2 (f). The result suggests that the roughness of the lithium negative electrodes gradually increases during the deposition process. Furthermore, the aggregated lithium particles could be the preferred site of the whisker-shaped lithium deposition, because the resistance of the fresh SEI layer on the deposited lithium is different from that of the preformed SEI layer before the electrodeposition. As a consequence, the local current density gets varied,

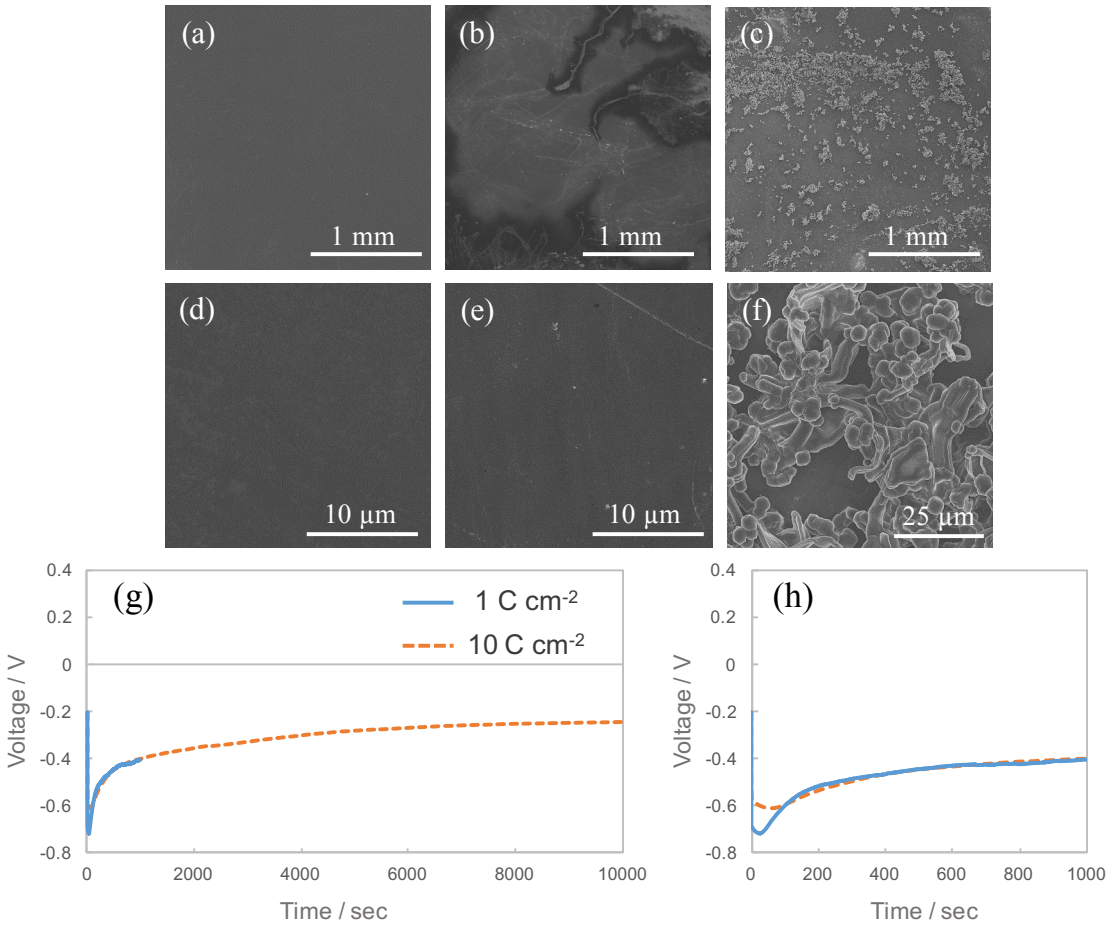

Fig. 1-2 The SEM images of the as-prepared lithium (a), the electrodeposited lithium for 1 C·cm^{-2} (b), and the electrodeposited lithium for 10 C·cm^{-2} (c). The magnified images of (a), (b) and (c) are (d), (e) and (f) respectively. The voltage profiles of the electrodeposition process are shown in (g): 1 C·cm^{-2} deposition (blue) and 10 C·cm^{-2} deposition (orange). The focused profiles for early stage of the deposition process are shown in (h).

and the dendritic lithium can easily be formed. The result suggests that the roughness of the lithium negative electrodes gradually increases during the deposition process.

Fig. 1-2 (g) shows the potential profiles of the galvanostatic electrodeposition process above, and the focused profiles for the early stage of the deposition process are shown in Fig. 1-2 (h). In both cases, the cell voltage initially dropped down and then continuously shifted to more positive value, during the deposition process. Even though the minimum voltage values were slightly different, these cells showed almost same voltage profiles after the 100 sec of the initial deposition process. I assume it was probably due to the slight difference of the surface condition of the electrodes before the deposition test. However, once the lithium deposition occurs, the surface conditions of the lithium electrodes get almost equal. Consequently, these two potential profiles overlapped each other during the following deposition process. Considering the SEM images in Fig. 1-2, the continuous potential shift during the lithium deposition process could be owing to the increase of the surface area by the uneven lithium deposition.

Since the surface condition significantly affects to the deposition as discussed in the above section, the SEI composition on the lithium negative electrode was investigated by XPS. Fig. 1-3 shows XPS spectra of the surface film on the Li foil immersed in the electrolyte solution: 1 mol dm^{-3} $LiPF_6$ EC:DEC 1:1 vol.%. The C 1s XPS spectra in Fig. 1-3 (a) show that a thick layer of lithium alkyl carbonates ($LiOCO_2R$) is one of the main components of the SEI layer, because the two strong peaks corresponding to $LiOCO_2R$ at 287.0 eV and C-H at 284.5 eV remained even after the argon sputtering for 40 minutes. The F 1s spectra (b) show a strong peak assigned to $Li_xPO_yF_z$ at 688.0 eV with small

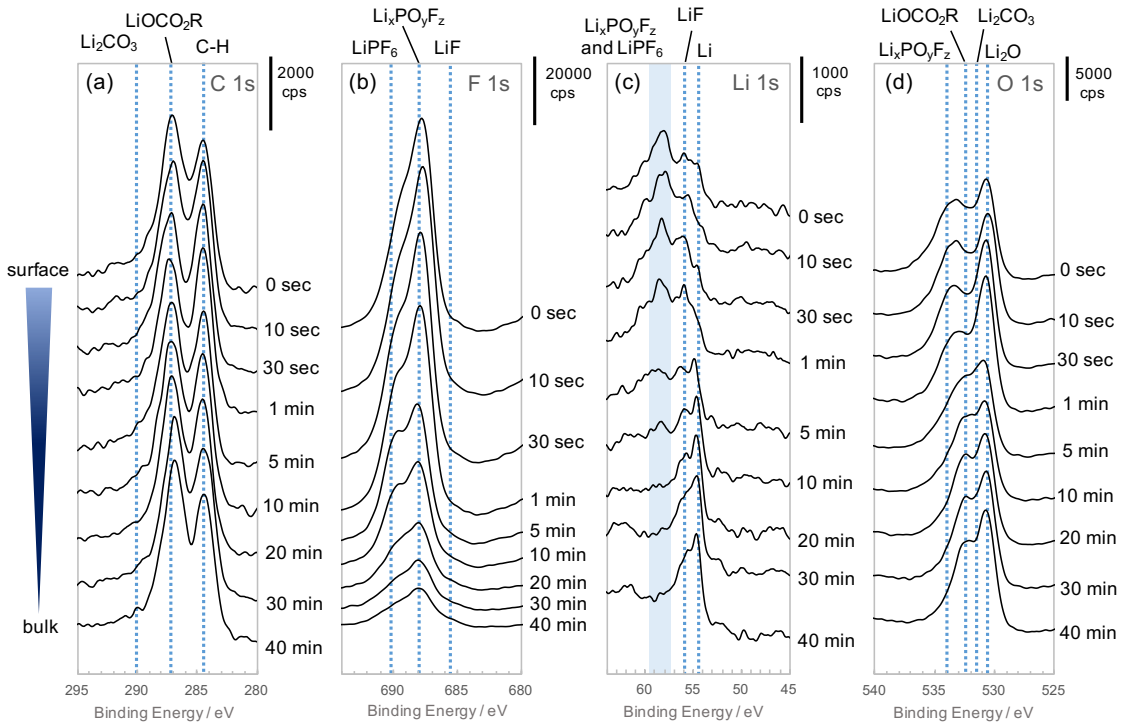

Fig. 1-3 The XPS spectra of lithium metal immersed in the normal electrolyte solution: 1 mol·dm^{-3} $LiPF_6$ EC:DEC 1 : 1 vol. %. The spectrum at the top of each graph represents the surface of the sample. The following spectra were taken after the argon sputtering for each sputtering time noted at the right side of the graph.

amount of the $LiPF_6$ and LiF. Contrarily to the F 1s XPS spectra, the $Li_xPO_yF_z$ mostly disappeared after 10 minutes of the argon sputtering process. It suggests that the fluorinated species mainly exist on the top of the SEI layer. The peaks corresponding to the $Li_xPO_yF_z$ are observed around 58.5 eV in the Li 1s spectra (c), and at 534.0 eV in the O 1s spectra (d) respectively. The Li 1s and the O 1s spectra also suggest that Li_2O could exist even in the bulk Li foil as an impurity phase, because the peak at 530.5 eV corresponding to Li_2O still remains even after the pure lithium metal is disposed by the argon etching process. To summering the XPS analysis result, the SEI layer on the lithium negative electrode, mainly consists of $LiOCO_2R$ and some $Li_xPO_yF_z$ species are formed at the top of the lithium.

1-3-2. Surface morphology changes by the electrolyte additives

In order to form a stable SEI layer to eliminate the lithium dendrite formation, I investigated the effect of the electrolyte additives used as SEI former for lithium-ion batteries. Fig. 1-4 shows the series of SEM images of the lithium metal deposited for 10 $C \cdot cm^{-2}$ from the electrolyte solution containing 5 vol. % FEC (a), (d), (g), 5 vol. % of VC (b), (e), (h) and 1 wt. % of LiBOB (c), (f), (i). Compared with the additive free electrolyte solution discussed in the previous section, all the electrodes maintained relatively smooth surface even after the 10 $C \cdot cm^{-2}$ of the electrodeposition. It shows that the film-forming additives are effective to stabilize the surface morphology of the electrodeposited lithium metal. Especially the FEC maintained very uniform surface morphology like the as-prepared lithium electrode as shown in Fig. 1-4 (a). It indicates

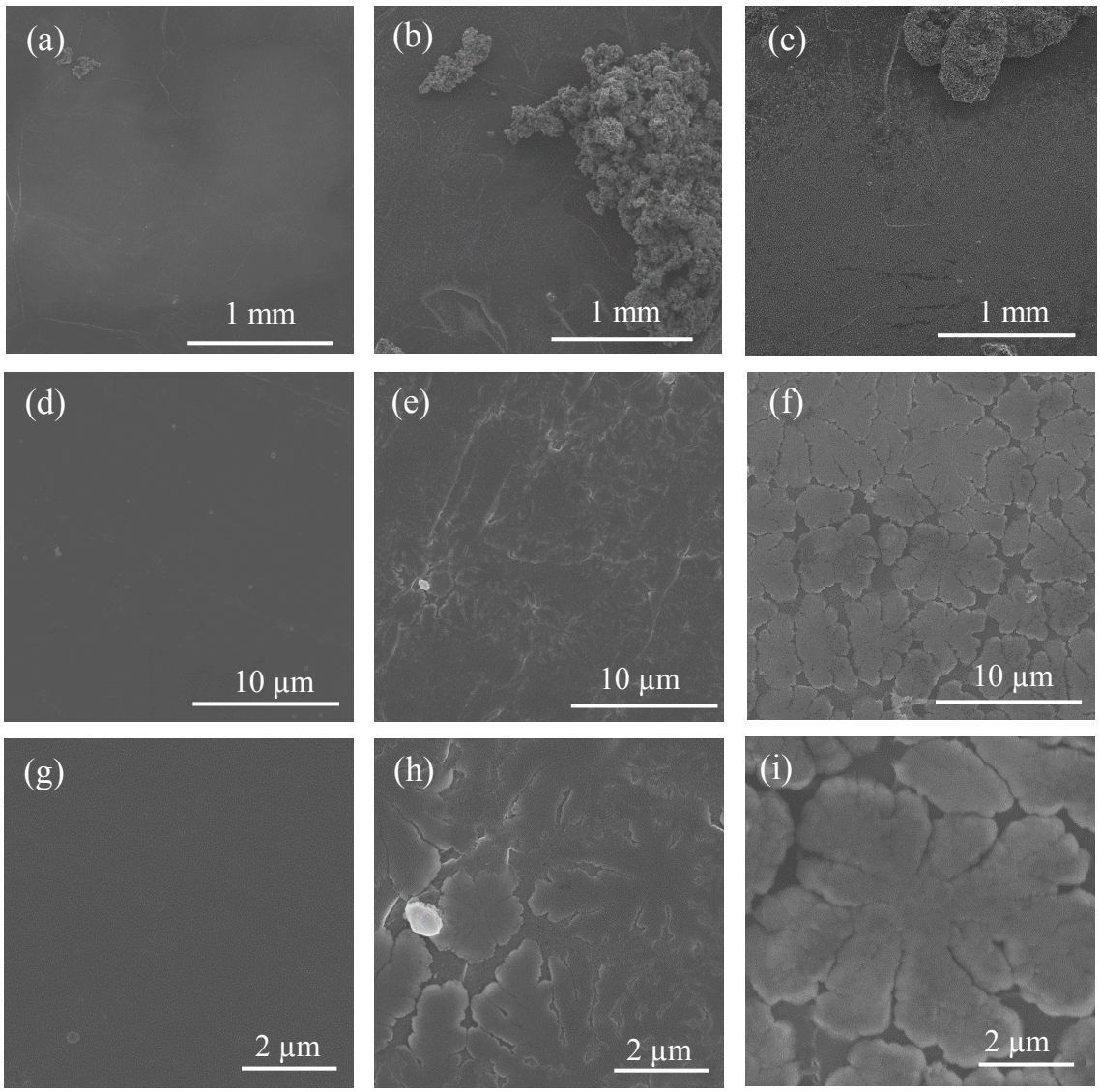

Fig. 1-4 The SEM images of the lithium negative electrode after 10 C cm^{-2} of electrodeposition at 1 mA cm^{-2} in the electrolyte solution containing the various film forming additives: 5vol.% of FEC (a), (d), (g), 5vol.% of VC (b), (e), (h) and 1 wt.% LiBOB (c), (f), (i).

the FEC forms a stable and uniform SEI layer, which enables the smooth deposition of lithium.

The lithium metal deposited in the electrolyte solution containing 5 vol.% of VC also shows uniform morphology as shown in Fig. 1-4 (b), (e) and (h), however it partially has dendritic growth of the lithium as shown in Fig. 1-4 (b). The magnified image showed a very unique morphology like seaweed as shown in Fig. 1-4 (e) and (h). I assume the seaweed-like morphology is due to the mechanical properties of the SEI layer, because the electrolyte solution containing VC is known to forms a rigid SEI [21]. The rigid SEI layer seems to limit direction of the particle growth and initiate the in-plane 2D growth of the deposited particles, as a consequence the typical dendrite growth seems to be delayed.

An electrolyte solution containing LiBOB also showed a similar morphology to the VC. The SEM images of the lithium negative electrode deposited from the electrolyte solution containing LiBOB are shown in Fig. 1-4 (c), (f) and (i). The solution also formed the seaweed-like lithium deposit as shown in Fig. 1-4 (f). It indicates that the LiBOB also forms a rigid SEI layer, which delays the formation of the dendritic lithium, however I assume the SEI layer is not as hard as SEI formed by VC, because the lithium 2D growth layer is thicker.

1-3-3. SEI layer in the electrolyte solutions containing additives

Since the discussions in the previous section suggested that the morphology of the deposited lithium is highly dependent upon the surface layer, a series of XPS

measurements were conducted to characterize the SEI layer formed in each electrolyte.

The XPS spectra of a lithium foil immersed in the electrolyte solution containing FEC are shown in Fig. 1-5. The C 1s spectra in Fig. 1-5 (a) have two main peaks corresponding to the $LiOCO_2R$ which is similar to the C 1s XPS spectra of the additive-free electrolyte discussed in the previous section. The $LiOCO_2R$ should also be the main component of the SEI layer formed in the electrolyte solution containing FEC because it remains even after the 40 minutes of Ar etching process as well as the additive-free electrolyte solution. The F 1s spectra shown in Fig. 1-5 (b) also show a peak corresponding to $Li_xPO_yF_z$, however the peak intensity was relatively weak compared with the additive-free one. It clearly shows that the decomposition of the PF_6^- anion was eliminated by the FEC. In the Li 1s spectra in Fig. 1-5 (c), a relatively strong peak assigned to LiF was observed while a peak corresponding to $Li_xPO_yF_z$ or $LiPF_6$ was mostly disappeared. These results suggest that the LiF in the SEI was formed not by the decomposition of the PF_6^- anion but by the decomposition of FEC. In the O 1s spectra, the peak intensity of a peak assigned to $Li_xPO_yF_z$ is also weak, compared to that of the additive-free electrolyte, as a consequence, the peak corresponding to the $LiOCO_2R$ is sharpen. This result is in good agreement with the spectra of C 1s, F 1s and Li 1s.

Thus I conclude that the FEC molecules are the direct source of the SEI layer rather than EC. The SEI formed by the FEC seem to be compact and uniform, as a consequence the decomposition of EC and PF_6^- is prevented. In addition, I assume that the suppression of the $Li_xPO_yF_z$ improves the uniform current distribution resulting in the smooth morphology of the deposited lithium.

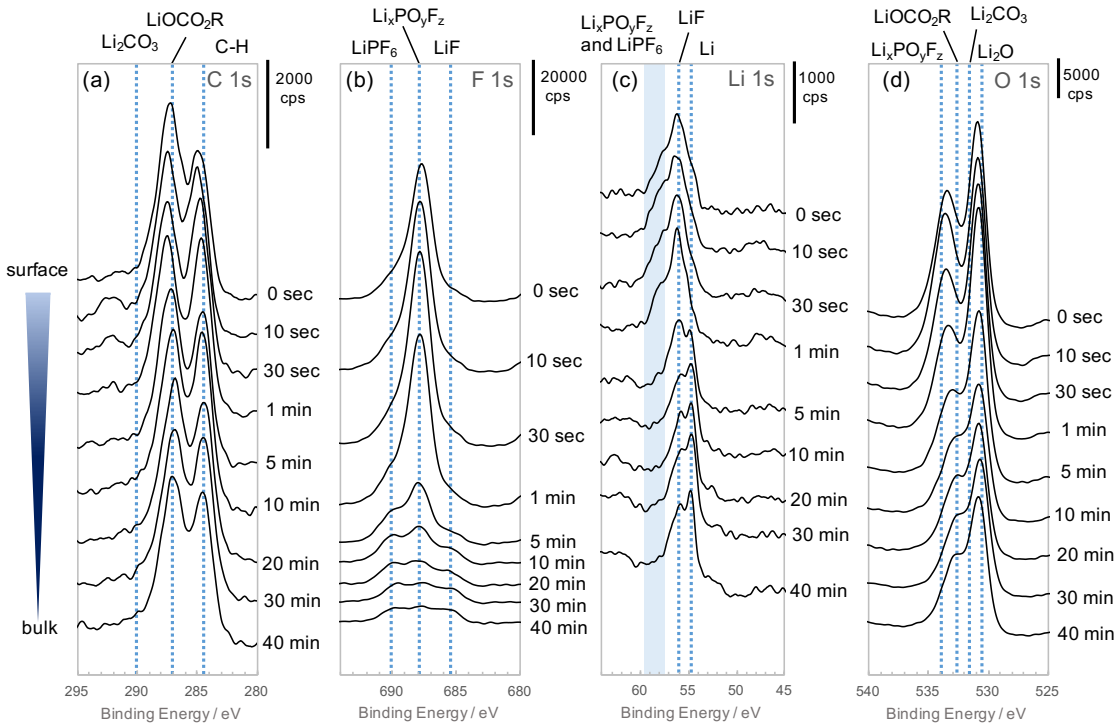

Fig. 1-5 The XPS spectra of lithium metal immersed in the normal electrolyte solution: 1 mol·dm^{-3} $LiPF_6$ EC:DEC 1 : 1 vol. % containing 5 vol. % of FEC. Same as the Fig. 2, the spectrum at the top of each graph represents the surface of the sample. The following spectra were taken after the argon sputtering for each sputtering time noted at the right side of the graph.

The vinylene carbonate (VC) forms a unique SEI layer compared with FEC. Figure 1-6 shows the XPS spectra of lithium foil immersed in the electrolyte solution containing 5 vol.% VC. A very strong peak at 287.0 eV of the C 1s spectrum and the peak at 535.5 eV in the O 1s spectrum suggests the formation of polycarbonate species at the very surface of the SEI layer. After 1 min of the argon sputtering process, a typical C 1s peak assigned to the $LiOCO_2R$ was observed. Again the main component of the SEI layer seems to be the $LiOCO_2R$. The F 1s spectra shown in Fig. 1-6 (b) have a strong peak corresponding to $Li_xPO_yF_z$. Since the peak intensity of the $Li_xPO_yF_z$ increases after 10 seconds of the argon sputtering, the typical SEI composing species such as $Li_xPO_yF_z$ and $LiOCO_2R$ beneath the thin polycarbonate layer. The Li 1s spectra also show that the $Li_xPO_yF_z$ and the $LiOCO_2R$ is the main product of the SEI Fig. 1-6 (c). In the Li 1s spectra, Li metal and Li_2O were detected after 5 minutes of the argon sputtering, suggesting that the SEI layer formed in the electrolyte containing VC is relatively thick. In addition, the O 1s spectra are in good agreement with above discussion.

The SEI layer formed in the VC containing electrolyte consists of the polycarbonate layer at the top of the surface and the thick organic and inorganic layer consists of the $LiOCO_2R$ and the $Li_xPO_yF_z$ beneath the polycarbonate layer. The SEI components under the top polycarbonate layer are very similar to the SEI layer for the additive-free electrolyte. Thus I suspect that the EC is still the main source to form the SEI layer, considering a proposed SEI formation mechanism reported by Ushirogata et al [78]. Furthermore, the top polycarbonate layer probably improves the mechanical properties of the SEI layer resulting in the delay of the dendrite formation and enhancement of the in-

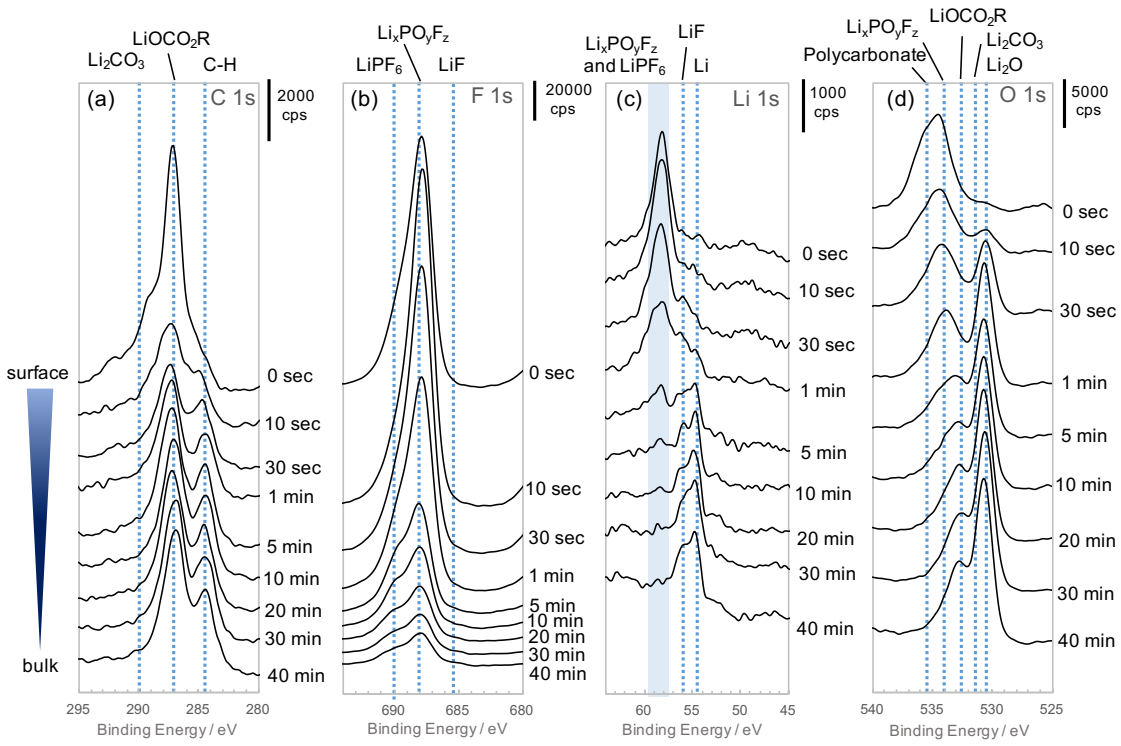

Fig. 1-6 The XPS spectra of lithium metal immersed in the normal electrolyte solution: 1 mol·dm^{-3} $LiPF_6$ EC:DEC 1 : 1 vol. % containing 5 vol. % of VC. The spectrum at the top of each graph represents the surface of the sample. The following spectra were taken after the argon sputtering for each sputtering time noted at the right side of the graph.

plane 2D growth of the lithium metal.

Fig. 1-7 shows the XPS spectra of the lithium metal immersed in the electrolyte solution containing 1 wt. % LiBOB. The SEI layer formed in the LiBOB containing electrolyte also has a similar polycarbonate species to the SEI formed by VC at the top of the SEI layer as shown in Fig. 1-7 (d). A strong peak at 287.3 eV in C 1s spectra represents the polycarbonate layer, which was also observed in the case of the VC containing electrolyte. Beneath the polycarbonate layer, $LiOCO_2R$ and $Li_xPO_yF_z$ are observed in C 1s, F 1s and Li 1s spectra as shown in Fig. 1-7 (a), (b) and (c). Notably the peak intensities of the $Li_xPO_yF_z$ in the F 1s spectra were very strong at the surface of the SEI layer, however the peak intensity immediately decreased after 1 minute of the argon sputtering. It shows that the SEI layer has high content of $Li_xPO_yF_z$ but the thickness of the $Li_xPO_yF_z$ layer is thin, suggesting that the BOB^- anion eliminates the decomposition of the PF_6^- anion.

It is known that the BOB^- forms a compact SEI layer at 1.7 V vs. Li, and the SEI layer prevents the co-intercalation of propylene carbonate (PC) into the graphite [79]. I think the LiBOB forms the very similar compact SEI layer, which suppresses the decomposition of the PF_6^- anion and the formation of $Li_xPO_yF_z$. The Li 1s and the O 1s spectra were very similar to the XPS spectra for the electrolyte solution containing VC.

Thus the electrolyte solution containing LiBOB also forms a top polycarbonate layer, which reinforces the mechanical properties of the SEI layer, resulting in the in-plane 2D growth of the lithium metal. Beneath the polycarbonate layer a thin $Li_xPO_yF_z$ layer exists and the $LiOCO_2R$ layer forms the matrix of the SEI layer.

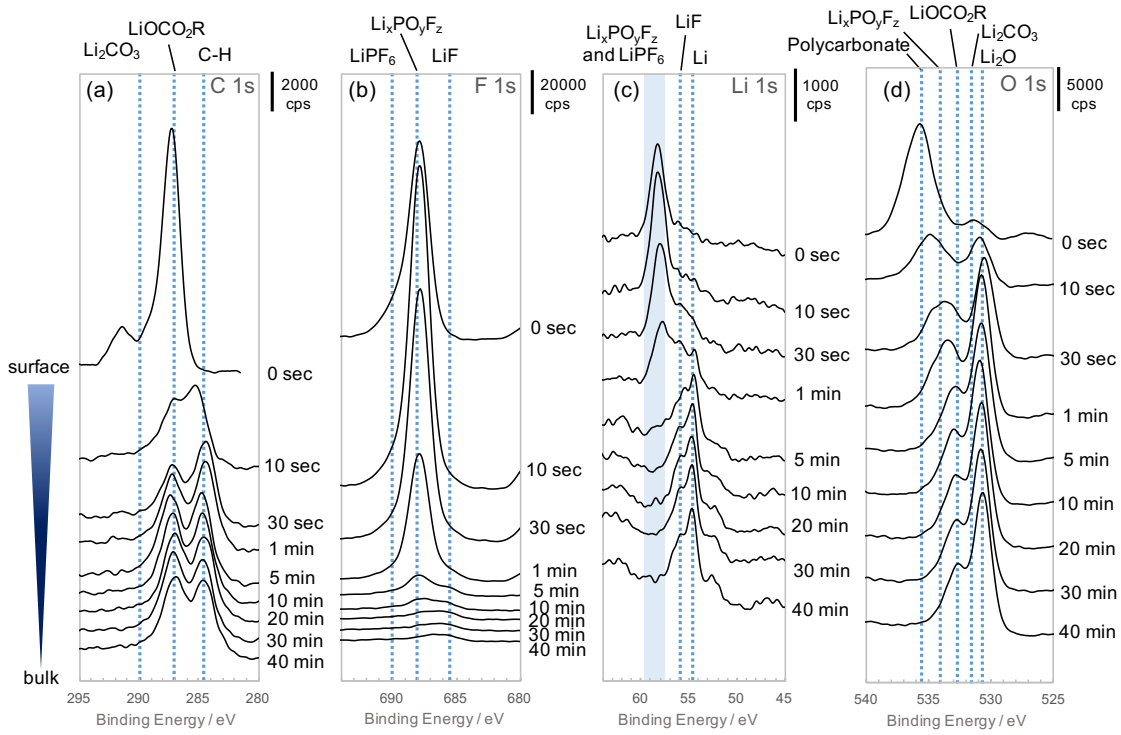

Fig. 1-7 The XPS spectra of lithium metal immersed in the normal electrolyte solution: 1 mol·dm^{-3} $LiPF_6$ EC:DEC 1 : 1 vol. % containing 1 wt. % of LiBOB. The spectrum at the top of each graph represents the surface of the sample. The following spectra were taken after the argon sputtering for each sputtering time noted at the right side of the graph. The B 1s spectra are omitted, because no clear peak was observed in all the B 1s spectra.

The ATR-FTIR spectra in Fig. 1-8 were in good agreement with the above discussions. Obviously the electrolyte solutions containing VC and FEC form more $LiOCO_2R$ and Li_2CO_3 compared with the additive-free electrolyte, suggesting that the both electrolyte additives form stable SEI layer based on organic species. However, the absorption peak corresponding to the $Li_xPO_yF_z$ observed around the wavenumber 880 cm^{-1} is mostly disappeared in the case of the electrolyte solution containing FEC while the lithium metal immersed in the additive-free electrolyte solution clearly formed it. The results also suggest that the top polycarbonate layer improves the mechanical properties of the SEI layer.

1-3-4. The influence of the SEI layer to the surface morphologies

Overall the surface morphology of the electrodeposited lithium can be improved be using the film-forming additives. All the lithium negative electrodes deposited from the electrolyte solutions containing the electrolyte additive: FEC, VC or LiBOB showed relatively uniform morphology compared with the lithium deposited from the additive-free electrolyte. The result clearly suggests that the SEI formed by the electrolyte additives significantly affects to the morphology of the deposited lithium metal.

In the case of the electrolyte solution containing FEC showed the smoothest morphology among the electrolytes solutions used in the present work. The SEI formed by the FEC mainly consists of $LiOCO_2R$. I observed the existence of the $LiOCO_2R$ in all the cases, however the electrolyte solution containing FEC formed less $Li_xPO_yF_z$ than other film forming additives. It shows the FEC eliminates the decomposition of the PF_6^-

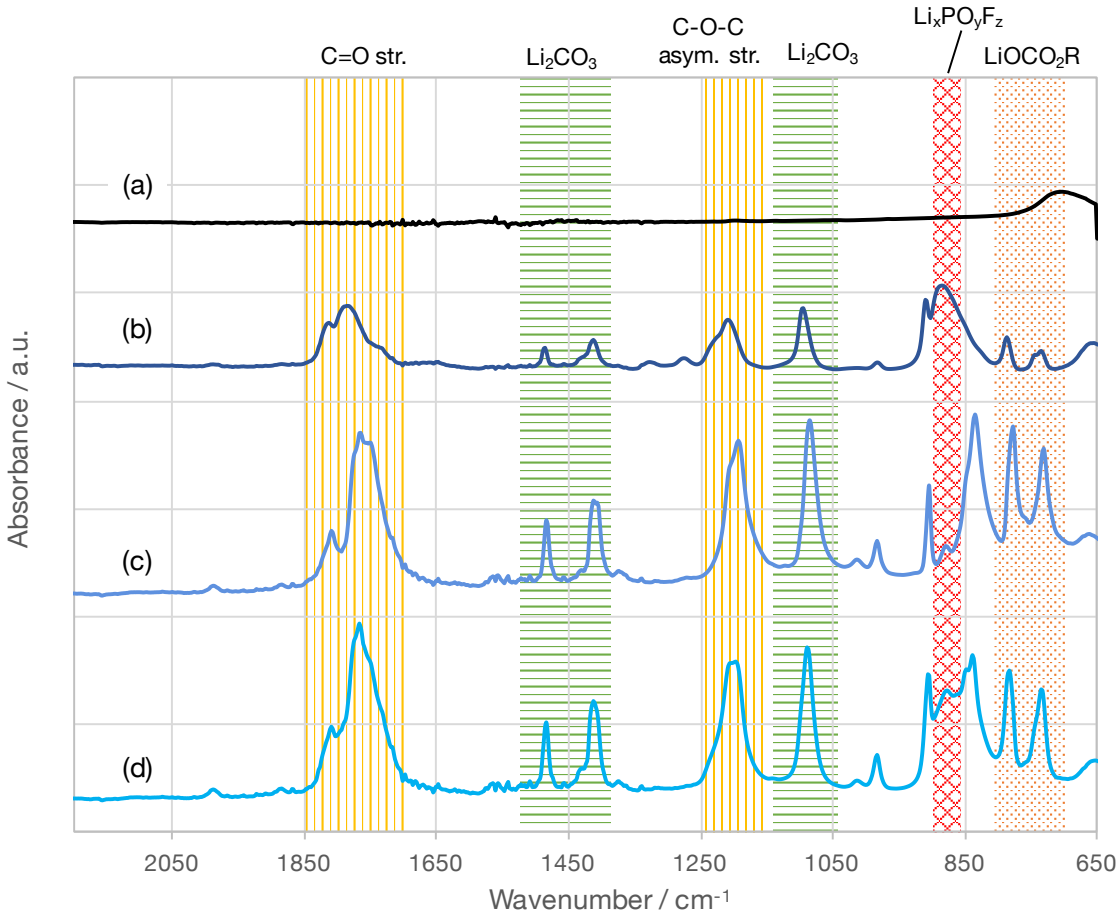

Fig. 1-8 The ATR-FTIR spectra for the surface as prepared lithium metal (a), the lithium metal immersed in the additive-free electrolyte solution (b), the electrolyte solution containing FEC (c) and VC (d).

anion. The $LiOCO_2R$ in the SEI could show similar physical properties such as Li ion conductivity to the bulk electrolyte solution, while $Li_xPO_yF_z$ is inactive for the Li ion conduction. Therefore, I think the suppression of the $Li_xPO_yF_z$ formation is effective to make uniform current distribution. The flexibility of the SEI layer formed in the electrolyte containing FEC contributes to the uniform deposition of lithium as already reported [21].

The electrolyte solution containing, VC or LiBOB form a relatively thick SEI layer having a polycarbonate layer at the top of the SEI layer. The polycarbonate layer probably improves the mechanical properties of the SEI layer, thus the dendritic growth of lithium was also suppressed and initiated the in-plane growth of the lithium metal.

1-4. Conclusion

In the present chapter, I investigated the relationship between the SEI layer and the surface morphology of the electrodeposited lithium. During the initial deposition process in an additive-free electrolyte solution, the lithium negative electrode maintains a very uniform surface morphology, however once the total deposition amount increases, the lithium electrode starts to form agglomerated particles of the dendritic lithium. The electrolyte additives FEC, VC and LiBOB eliminate the dendritic growth of the lithium during the electrodeposition process, because these additives form stable SEI layer at the surface of the lithium negative electrodes.

In order to understand the role of the additives, XPS and ATR-FTIR analyses were carries out for the lithium negative electrodes immersed in the electrolyte solutions. The additive-free electrolyte solution forms an SEI layer composed of $LiOCO_2R$ and $Li_xPO_yF_z$. Since the electrolyte containing FEC suppresses the decomposition of the PF_6^- anion, the FEC containing electrolyte could form a thin and uniform SEI layer resulting in the uniform lithium deposition. I also carried out further analyses of the SEI layer formed by the electrolyte additives VC and LiBOB. Both electrolyte additives form SEI layers, having a polycarbonate layer at the top of the SEI layer. The polycarbonate layer improves the mechanical properties of the SEI layer and initiates in-plane 2D growth of the lithium particles.

Here I conclude that the electrolyte additives are basically effective to eliminate the dendritic growth of the lithium. Two different types of the SEI layers were actually detected, one is thin flexible SEI by FEC and another is thick and rigid SEI formed by VC and LiBOB. Regarding the morphology of the deposited lithium, I think the thin and flexible SEI layer formed in the electrolyte containing FEC is preferable to avoid the dendritic growth of lithium. Further investigations for the electrolyte additives and the interphase are necessary for the development of the practical lithium negative electrodes.

Chapter 2

Passivation Layer Formation of Magnesium Metal Negative Electrodes for Rechargeable Magnesium Batteries

2-1. Introduction

Grignard reagent such as ethyl magnesium bromide in tetrahydrofuran (THF), is well known as an electrolyte solution for rechargeable magnesium batteries. The electrolyte solutions show excellent reversibility and wide potential window > 3V [44, 45]. Kim et al. proved that the electrochemical active species in the organohaloaluminate-based electrolyte solution is magnesium dimer complex [46, 47]. Even with the electrochemical window, the organohaloaluminate-based electrolytes have corrosive properties at high electrode potential due to the halides contained in the structure [47, 48]. These corrosive properties make it difficult to use high voltage cathode, due to the increased risk of transition metal dissolution. Thus, it is very crucial to explore another electrolyte solution which has wide electrochemical window without corrosive properties.

Conventional ionic electrolyte solutions using magnesium bis(trifluoromethansulfonyl)amide: $Mg(TFSA)_2$ dissolved in ether-based solvents are discovered as alternate electrolyte solutions for the magnesium metal anode [50-52]. Ha et al. reported that corrosion of stainless steel and aluminum foil can be inhibited in

$Mg(TFSA)_2$-based ionic electrolyte solutions, however, limitations still exist. However, the ionic electrolyte solutions show very high over potential >1.0 V and poor coulombic efficiency < 60% at room temperature, suggesting that some side reaction is taking place besides the electrochemical deposition / dissolution of the magnesium metal, resulting in the partial passivation of the electrode surface.

In this study, I carried out a comparative study of the electrochemical deposition processes of magnesium metal in an organohaloaluminate-based electrolyte solution and a $Mg(TFSA)_2$-based electrolyte solution. I mainly focused on the characterization of the surface layer using *in situ* FTIR and XPS, and discussed the key parameter for the smooth deposition / dissolution process of the magnesium metal.

2-2. Experimental

2-2-1. Preparation of the Electrolyte solutions

In the present chapter, an organohaloaluminate-based electrolyte solution: 0.25 M $EtMgCl\text{-}2Et_2AlCl$ in THF (EAC electrolyte solution) and an ionic electrolyte solution: 0.5 M $Mg(TFSA)_2$ in butyl methyl triglyme (BuMeG3 electrolyte solution) were prepared. The EAC electrolyte solution was prepared by mixing a 2 M EtMgCl in THF (Sigma Aldrich), Et_2AlCl (Nippon Aluminum Alkyls) and anhydrous THF (Sigma Aldrich). The BuMeG3 electrolyte solution is prepared by dissolving the $Mg(TFSA)_2$ salt (Kishida) in BuMeG3 (Wako). The chemicals used for the EAC electrolyte solution were used

without further purification. On the other hand, the chemicals for the BuMeG3 electrolyte solutions were well dried before usage; the $Mg(TFSA)_2$ was dried under vacuum at 170 ºC for 8 hours. The BuMeG3 was dried with an activated molecular sieve to reduce the water content < 30 ppm.

2-2-2. Electrochemical Measurements

Cyclic voltammetries were executed using a three-electrode cell shown in Fig. 2-1. A platinum foil (Nilaco) was employed for the working electrode. The counter and reference electrode is a polished magnesium foil and wire (Nilaco) respectively. The magnesium foil was polished by slide glass to remove the native oxide layer at the surface of the electrode just before usage in an argon filled glove box, whose atmosphere is controlled < 0.1 ppm of water content. The potential range of the CV measurement for the EAC electrolyte solution was between -1.0 and 2.0 V vs. Mg quasi-reference electrode, at the sweep rate 25 mV sec^{-1}. In the case of the BuMeG3 electrolyte solution, the CV measurement was taken between -2.4 and 2.0 V vs. Mg quasi-reference electrode, at 1 mV sec^{-1} of the sweep rate.

The galvanostatic electrodeposition was carried out with the same three-electrode cell as the CV measurements. The deposition current was 0.5 mA cm^{-2} for 6000 sec. The total electric charge for the magnesium deposition was 3 C cm^{-2} of cathodic current. After the galvanostatic electrodeposition process, the cells were disassembled and the platinum electrodes were rinsed with anhydrous dimethoxyethane (DME, Sigma Aldrich). The characterization of the electrodeposited magnesium was carried out using X-ray

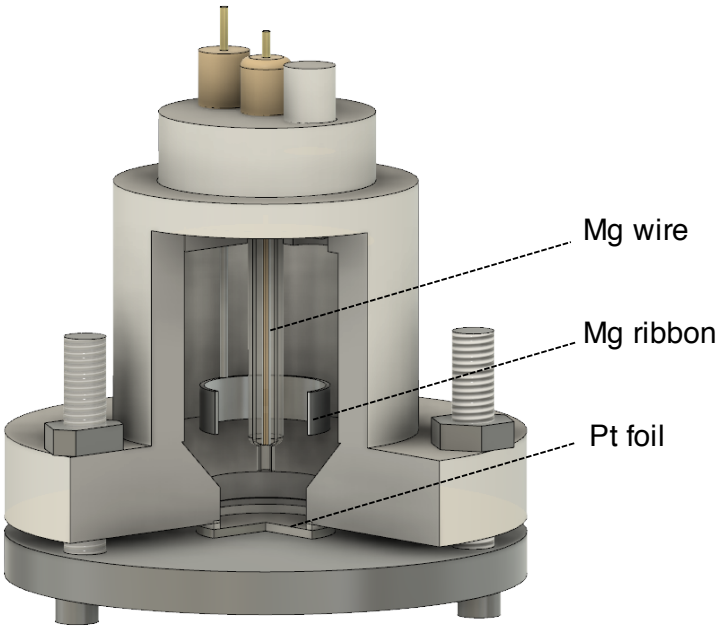

Fig. 2-1 Schematic representative of the three-electrode cell

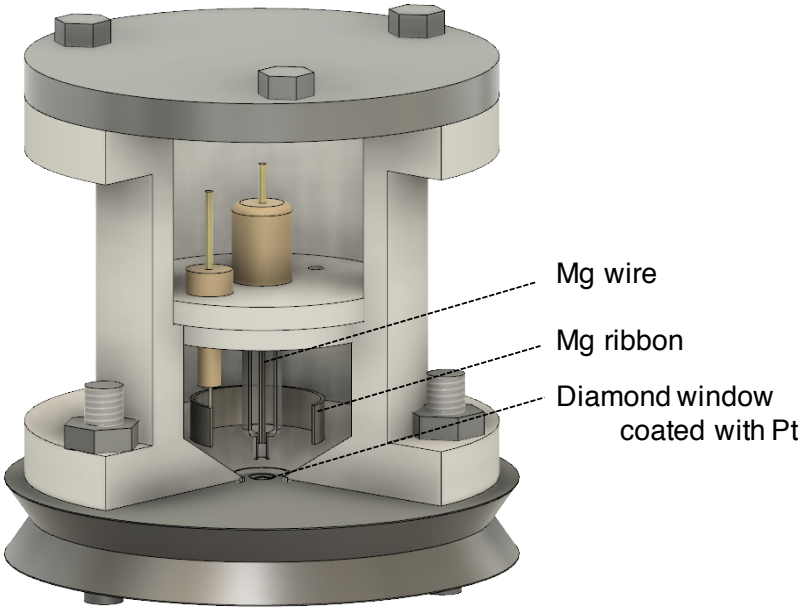

Fig. 2-2 Schematic representative of the diamond ATR-based in situ FTIR cell

diffraction (XRD, Rigaku, RINT2500). The surface morphologies of the electrodeposited magnesium were observed using a field emission SEM (Hitachi, S-4800).

2-2-3. Surface analyses

The surface analyses were carried out using *in-situ* FTIR spectroscopy and X-ray photoelectron spectroscopy (XPS). In order to obtain the *in situ* FTIR spectra, I developed a diamond ATR-based *in situ* FTIR cell as shown in Fig. 2-2. A standard laboratory FTIR spectrometer (Nicolet^{TM} iS^{TM}50 FTIR, ThermoFisher Scientific) with an MCT-detector was employed for the spectroscopic measurement. The Pt thin film electrode was deposited on a commercial diamond-ATR disc (DuraSamplIR, Smiths Detection) using DC sputtering coater, and the *in situ* FTIR measurement was carried out by an internal reflection geometry. The counter and the reference electrodes were magnesium foil and wire, same as the normal electrochemical measurements.

The in situ FTIR spectra were taken during CV measurements. The sweep rate of the CV is 0.2 mV sec^{-1} for both electrolyte solution. The potential range for the EAC electrolyte solution is between -0.4 and 1.2 V vs. Mg quasi-reference electrode. The potential range of the BuMeG3 electrolyte solution is between -1.4 and 1.2 V vs. Mg quasi-reference electrode. The lower potential limits of these CV measurements are set just above the onset electrode potential for the magnesium deposition.

Each FTIR spectrum was taken by the single beam mode with 512 of accumulation time. Subtractive normalized interfacial FTIR (SNIFTIR) spectrum was calculated by

$$\Delta R=(R_{n+1}-R_n)/R_n \quad (1)$$

where R_n is a reference reflective spectrum and R_{n+1} is a reflective spectrum at a target electrode potential. Typical SNIFTIR spectrum has positive and negative peaks; the positive peaks are corresponding to the disappeared species at the vicinity of the electrode during the measurements of two spectra. The negative peaks are corresponding to the newly formed species such as surface layer formed at the surface of the electrode. Adsorption and desorption process of the chemical species of the electrolyte solution at the surface of the electrode could also be appeared in the SNIFTIR spectra.

XPS was carried out to analyze the surface layer remained at the surface of the magnesium metal. Prior to the XPS measurements, the magnesium foils were also polished with slide glass in an argon filled glove box to remove the original passivation layer. Subsequently, the magnesium foils were immersed in either the EAC electrolyte solution or the BuMeG3 electrolyte solution for 24 hours. The magnesium samples were rinsed with DME and dried under vacuum.

The prepared samples were placed in a transfer vessel in the glove box. The vessel was connected with sample introduction chamber of the XPS and evacuated the chamber < 1.0 Pa for five minutes. The introduction chamber was subsequently filled with dried argon gas, then the sample were transferred into the introduction chamber. The XPS measurements were carried out with a standard XPS (Shimadzu. ESCA 3400) with Mg K α radiation. The emission current and the acceleration voltage of the X-ray Gun is 20 mA and 10 kV respectively. Depth profiles were taken by argon sputtering

with the ion gun of emission currents: 20 mA and acceleration voltage: 2 kV. The etching rate is > 40 Åmin^{-1} based upon SiO_2 and the etching time was 0, 10, 30, 30, 60, 300, 600, 1200, 1800 and 2400 sec.

2-3. Results and Discussion

2-3-1. Comparison of the electrochemical behavior of magnesium deposition-dissolution

Fig. 2-3 shows the cyclic voltammograms (CVs) of the magnesium deposition-dissolution processes in the EAC electrolyte solution and the BuMeG3 solution. The both CVs showed good agreement with results reported in elsewhere [52, 80]. In the case of the EAC electrolyte solution, the overpotential of CV was approximately 0.34 V, while the overpotential of the ionic electrolyte solution was 1.66 V; this value is extremely large for battery applications. Furthermore, the ionic electrolyte solution showed a poor coulombic efficiency of 60 % was observed for the ionic electrolyte solution, as illustrated in the inset of Fig. 2-3 (b), while the EAC electrolyte solution showed 99.7 % of the coulombic efficiency (inset of Fig. 2-3 (a)). The poor coulombic efficiency of the ionic electrolyte solution in Fig. 2-3 (b) suggests that the cathodic current is corresponding not only to the deposition of the magnesium metal but also to the reduction of the electrolyte solution. The low current density for the deposition/dissolution process in the ionic electrolyte solution suggests that the activity of the Mg^{2+} ion is low, compared with the

EAC electrolyte solution. Both of two oxidation peaks in the ionic electrolyte solution are corresponding to the dissolution of the magnesium metal. I think preferred orientation of the deposited magnesium particle could be a possible reason for two peaks, because the crystal growth or the electrodeposited magnesium metal along *c* axis: [001], is slower than that of *a*/*b* axis: [100] or [110], in previous report [34]. In this case two types of the magnesium metal particles having different preferred orientation, could have benn deposited. Another possibility is formation of inhomogeneous surface layer of the deposited magnesium. The deposited magnesium could be partially covered with high resistive layer via the reduction of the electrolyte solution. Further characterization of the deposited magnesium is necessary to understand the unique dissolution process of the magnesium metal.

Fig. 2-4 (a) and (b) show SEM images of the magnesium films deposited in the EAC electrolyte solution and the BuMeG3 solution. In the case of the EAC electrolyte solution, a dense magnesium film with a smooth surface morphology was deposited as shown in Fig. 2-4 (a). The magnified image shown in the inset of Fig. 2-4 (a), shows hexagonal-shaped grains, which probably reflects the hexagonal close packing structure of the magnesium metal [81]. On the other hand, the surface morphology of the magnesium deposited in the ionic electrolyte solution shows a surface morphology with aggregated spherical particles with small dimples. Furthermore, the deposited magnesium film is porous and not uniform, thus the Pt substrate is partially observed beneath the aggregated magnesium particles.

The XRD patterns of the magnesium films, deposited in the EAC electrolyte

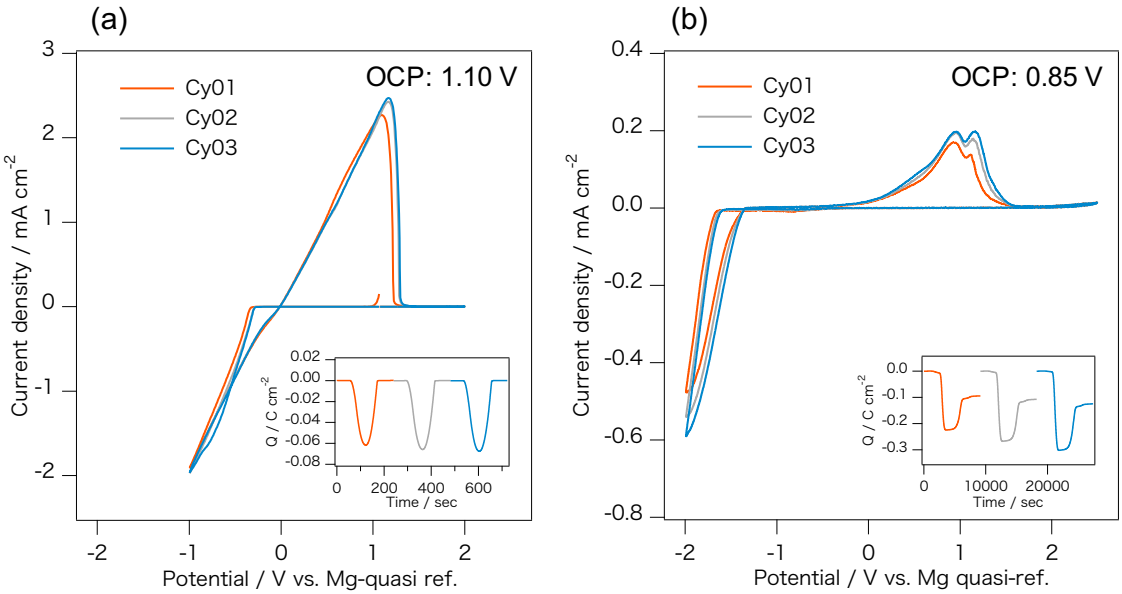

Fig. 2-3 Cyclic voltammograms for the deposition-dissolution processes of the Mg metals in the 0.25 M EtMgCl-2Et_2AlCl in THF (a) and the 0.5 M $Mg(TFSA)_2$ in BuMeG3 (b).

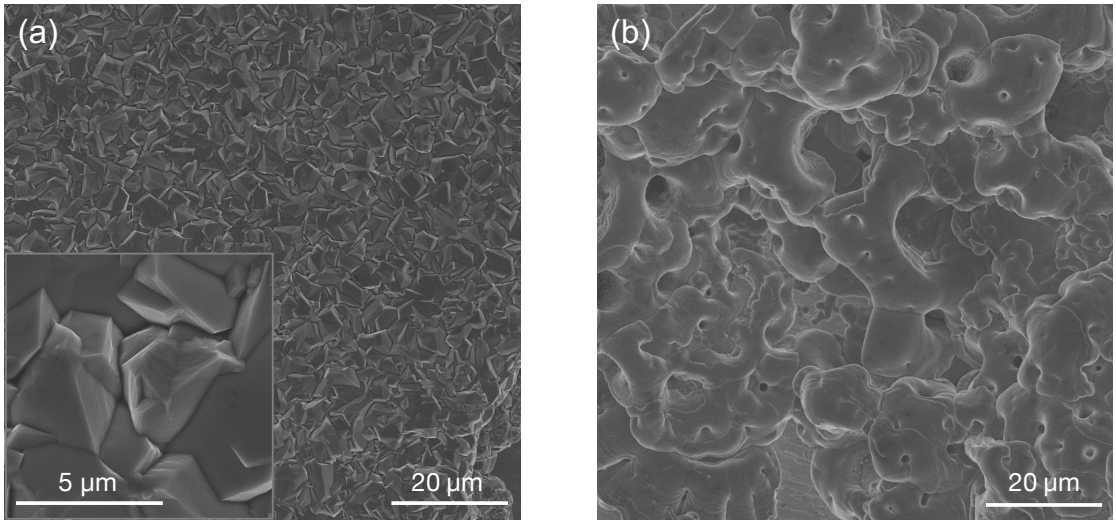

Fig. 2-4 SEM images of the Mg metals deposited on the Pt substrates in the 0.25 M EtMgCl-2Et_2AlCl in THF (a) and the 0.5 M $Mg(TFSA)_2$ in BuMeG3 (b).

solution and the BuMeG3 solution, are shown in the Fig. 2-5. Both of the diffraction patterns well matched with the simulated powder pattern of magnesium metal from the database (ICDD pdf 00-035-0821). Since the XRD pattern of the magnesium film deposited in the EAC electrolyte solution has sharp peaks, the electrodeposited magnesium film is highly crystalline. On the other hand, the XRD pattern of the electrodeposited magnesium film in the BuMeG3 solution had relatively broad peaks, suggesting that the deposited magnesium has poor crystallinity [82]. Furthermore, the XRD pattern of the magnesium metal deposited in BuMeG3 normalized with 101 reflection peaks observed at 36.5 º of 2 θ. It suggests that the amount of the deposited magnesium is not as much as that of EAC electrolyte solution, because of the low S/N ratio of the diffraction pattern. The poor coulombic efficiency with the small amount of deposited magnesium metal, suggests that some side reactions such as the reduction of the electrolyte solution, took place during the electrodeposition process in the BuMeG3 solution. The side reaction may hinder the smooth crystal growth process of the magnesium.

Generally, it is considered that the surface films are not formed at the surface for reversible magnesium deposition/dissolution process, because the magnesium metal easily forms passivation layer with no ionic conductive properties. The EAC electrolyte solution is a typical example of the passivation-free electrolyte solution, as a consequence the EAC electrolyte solution shows approx. 100% of the coulombic efficiency during the deposition/dissolution process. On the other hand, a surface layer is probably formed in the BuMeG3 electrolyte solution, because it shows poor coulombic efficiency.

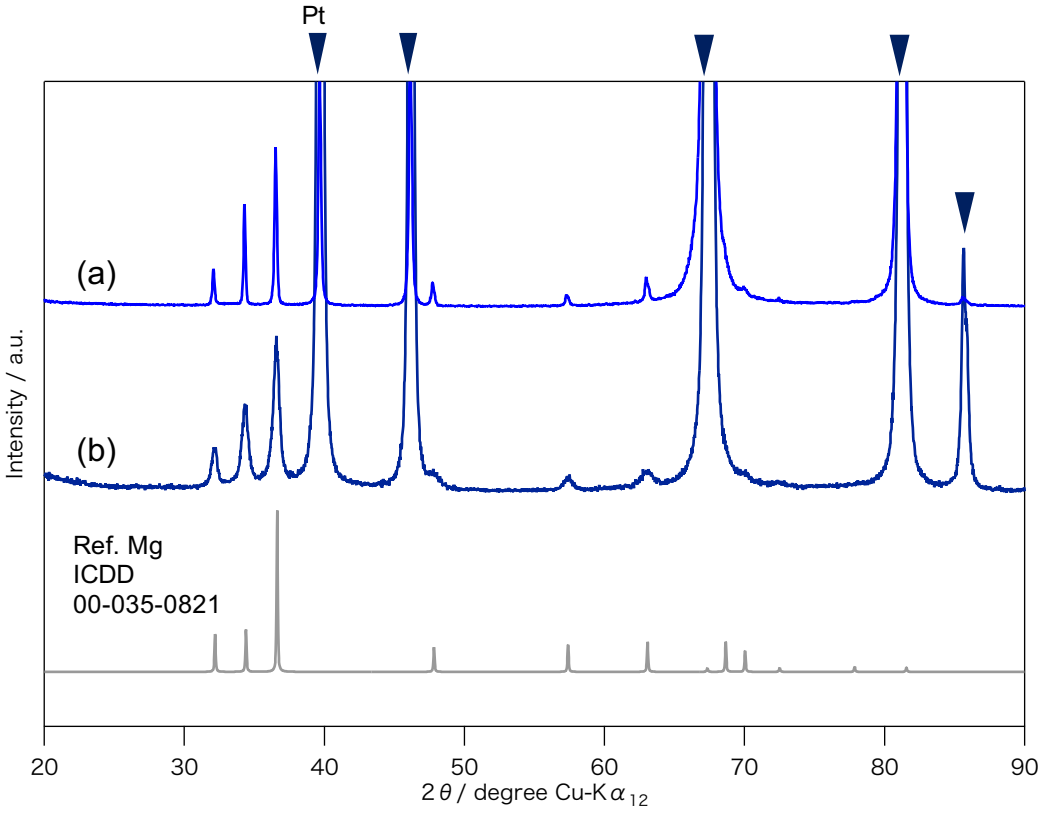

Fig. 2-5 X-ray diffraction patterns of the electrodeposited Mg metals on the Pt substrates in the 0.25 M EtMgCl-2Et_2AlCl in THF (a) and the 0.5 M $Mg(TFSA)_2$ in BuMeG3 (b) with a reference diffraction pattern (#ICDD 00-035-0821).

2-3-2. Investigation of the decomposed electrolyte solution during the reduction-oxidation process

In order to confirm the reduction process of the electrolyte solutions, I conducted *in situ* FTIR spectroscopy and XPS. Fig. 2-6 shows a series of *in situ* FTIR spectra of the EAC electrolyte solution during CV measurements. The CV measurement for the *in situ* FTIR was carried out between -0.4 and 1.2 V vs. Mg quasi-reference electrode, and the sweep rate was 0.2 mV sec^{-1}. The lower potential limit of CV needs to be above the onset electrode potential of magnesium deposition, because it is necessary to maintain the thickness of the working electrode enough thin. Otherwise, the incident infrared beam is reflected by the deposited magnesium metal, as a consequence, the evanescent wave the electrode/electrolyte interphase.

The *in situ* FTIR spectra observed strong peaks corresponding to the structural changes even at high electrode potential >0.5 V vs. Mg quasi-reference electrode. Several positive and negative peaks around 1078-860 cm^{-1} are corresponding to THF molecules. The positive peaks at 1062 and 1025 cm^{-1} are assigned to the antisymmetric and symmetric C-O-C stretching vibration, the positive peaks at 899 and 854 cm^{-1} are assigned to the CH_2 wagging vibration of THF. The negative peak observed at 1078 cm^{-1} is corresponding to the ν C-O-C stretching vibration of THF molecules at the surface of the electrode. These spectrum changes are continuously observed during the cathodic scan of the CV measurement, suggesting that the THF molecules continuously form a surface layer until the electrode potential reaches at -0.4 V vs. Mg quasi-reference electrode. A summary of the peak assignment for the *in situ* FTIR spectra for the EAC

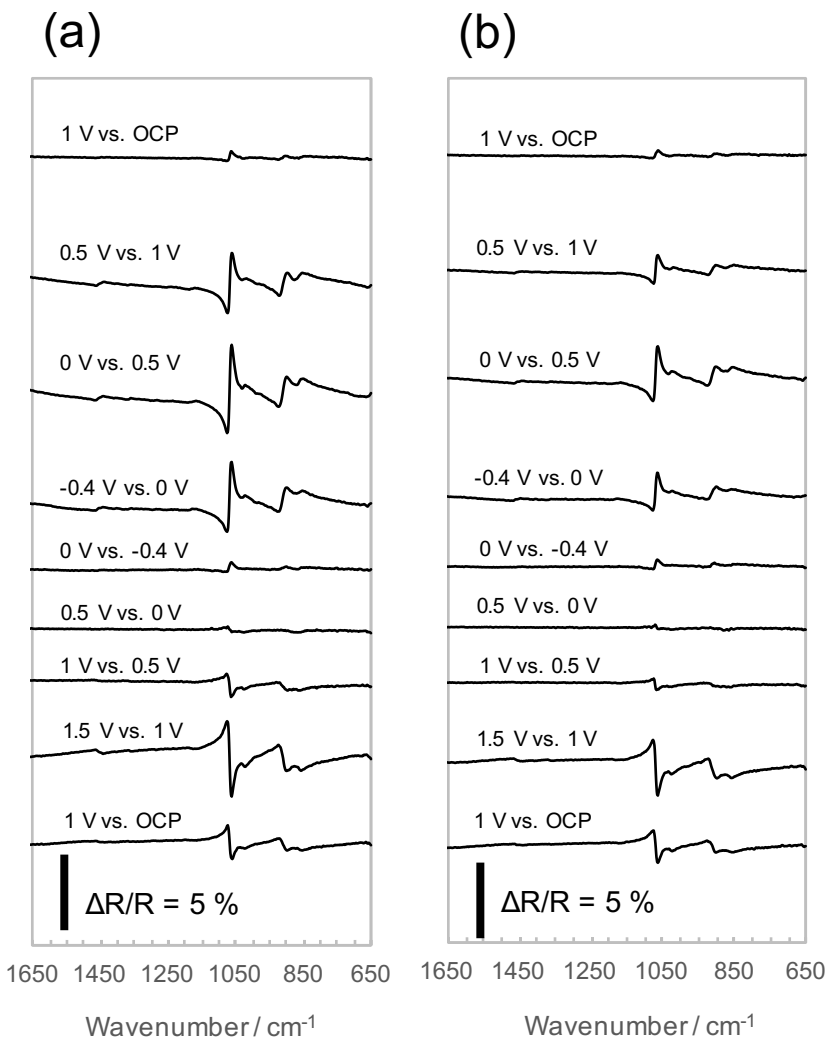

Fig. 2-6 *in situ* FTIR spectra of a CV measurement using a Pt thin film electrode formed on the diamond window in the 0.25 M EtMgCl-2Et_2AlCl in THF solution, between the open circuit potential (1.32 V vs. Mg quasi-reference electrode) and -0.4 V vs. Mg quasi-reference electrode, during the 1st CV cycle (a), and the 2nd cycle (b).

Table 2-I Summary of the peak assignments of the *in situ* FTIR spectra for the 0.25 M EtMgCl-2Et_2AlCl in THF solution during the 1st cathodic scan

cm^{-1}	
	Positive Peaks
1062	C-O-C asymmetric stretching vibration of free THF
1025	C-O-C asymmetric stretching vibration of solvated THF
899	C-H wagging vibration of THF
854	C-H wagging vibration of THF
	Negative Peaks
1074	C-O-C asymmetric stretching vibration of adsorbed THF
921	C-H bending vibration of adsorbed THF

electrolyte solution is shown in Table 2-I [83].

The *in situ* FTIR spectra for the 1st anodic scan are also shown in Fig. 2-6 (a). Since the *in situ* FTIR spectra at the beginning of the anodic scan did not show clear peaks, the adsorbed molecules seem to remain at the surface of the electrode. As the electrode potential reaches to more positive >1.0 V vs. Mg quasi-reference electrode, some spectrum changes were observed. The *in situ* FTIR spectrum at more positive electrode potential showed a flipped shape of the spectrum during the cathodic scan, thus I think the surface layer in the EAC electrolyte is based upon an adsorption or a structural reformation of the THF molecules at the vicinity of the electrode. Since the surface layer is not formed by the irreversible decomposition of the electrolyte solution, the EAC electrolyte maintains a dynamic reversible interphase. In the following CV cycle, almost same reversible spectra changes are detected as shown in Fig. 2-6 (b). The peaks are most clearly observed at -0.4 and 1.5 V vs Mg quasi-reference electrode during the cathodic and the anodic scan respectively. This overpotential for the reversible spectrum changes could be related with the formation process of the intermediate species of Mg deposition such as decomposed Mg dimer species reported in the past [46].

Fig. 2-7 shows SNIFTIR spectra of the electrolyte solution: 0.5 M $Mg(TFSA)_2$ in BuMeG3 during the CV measurement. In this case, the CV measurement was scanned between 1.2 and -1.4 V vs. Mg quasi-reference electrode, which is the electrode potential range just above the magnesium deposition occurs. The sweep rate of the CV measurement was 0.2 mV sec^{-1} as well. During the 1st cathodic scan, several positive and negative peaks were observed at 0 V vs. Mg quasi-reference electrode and more

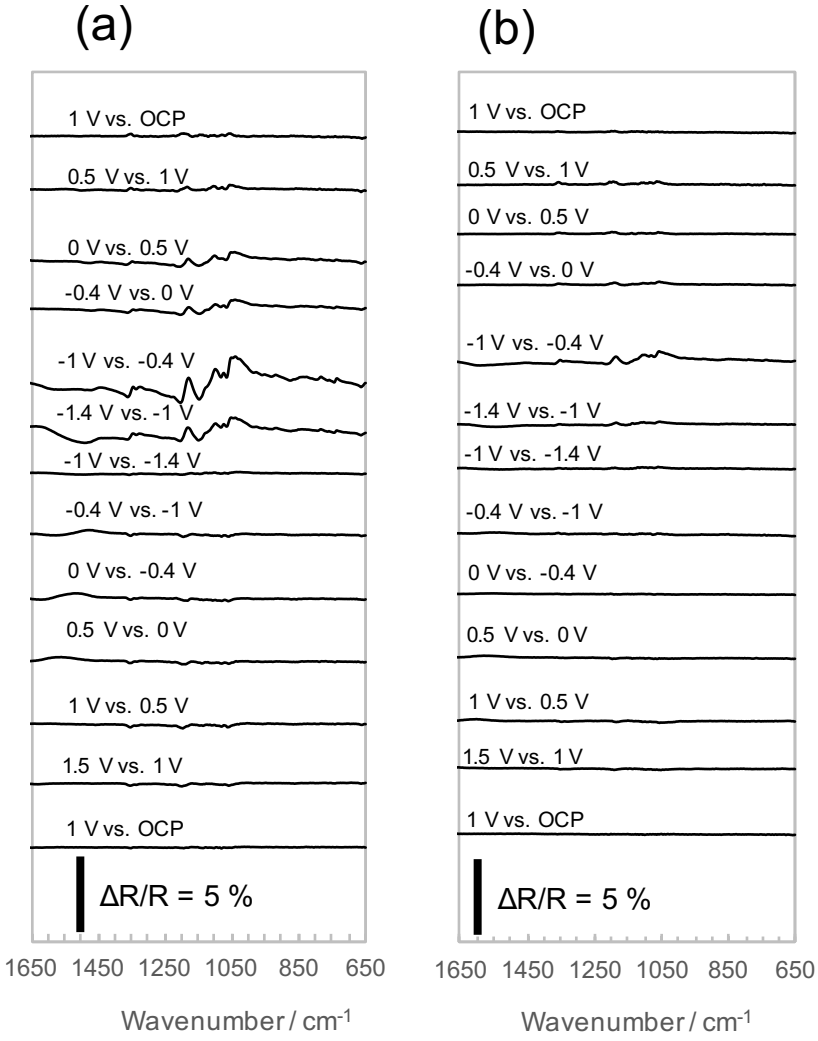

Fig. 2-7 *in situ* FTIR spectra of a CV measurement using a Pt thin film electrode formed on the diamond window in the 0.5 M $Mg(TFSA)_2$ in BuMeG3 solution, between the open circuit potential (1.15 V vs. Mg quasi-reference electrode) and -1.4 V vs. Mg quasi-reference electrode, during the 1st CV cycle (a), and the 2nd cycle (b).

Table 2-II Summary of the peak assignments of the *in situ* FTIR spectra for the 0.5 M $Mg(TFSA)_2$ in BuMeG3 solution during the 1st cathodic scan

cm^{-1}	
	Positive Peaks
1346	O=S=O bending vibration of the TFSA anion
1328	O=S=O bending vibration of the TFSA anion
1182	Antisymmetric CF_3 stretching vibration of the TFSA anion
1100	C-O-C antisymmetric stretching vibration of the BuMeG3
1051	S-N-S stretching vibration of the TFSA anion
1041	O=S=O symmetric stretching vibration of the TFSA anion
979	C-O-C symmetric stretching vibration of the BuMeG3
919	O=S=O symmetric stretching vibration of the TFSA anion
782	C-S stretching vibration of the TFSA anion
759	CF_3 bending vibration of the TFSA anion
736	CH_2 rocking vibration of the BuMeG3
	Negative Peaks
1361	O=S=O bending vibration of the decomposed TFSA anion
1209	Antisymmetric CF_3 stretching vibration of the decomposed TFSA anion
1149	C-O-C antisymmetric stretching vibration of the adsorbed / decomposed BuMeG3
1083	S-N-S stretching vibration of the decomposed TFSA anion
1066	O=S=O symmetric stretching vibration of the decomposed TFSA anion

negative electrode potential. The positive peaks at 1346, 1328, 1041, 919 cm^{-1} are assigned to SO_2 and the peaks at 1182, 759 cm^{-1} are assigned to CF_3 in TFSA anion respectively. Those peaks were continuously observed until the electrode potential reached to the lower potential limit. Table 2-II shows a summary of the peak assignments for the BuMeG3 electrolyte solution. Subsequently SNIFTIR spectra for the 1st anodic scan was taken, however, almost no clear peaks were observed during the anodic scan up to the open circuit potential suggesting that a stable surface layer was formed during the 1st cathodic scan. Furthermore, the SNIFTIR spectra for the 2nd CV measurement shows even more flat spectra both cathodic and anodic sweep. I think the surface layer on the Pt thin film electrode during the 1st cathodic scan is not like the surface layer so-called "solid electrolyte interphase (SEI) layer" but a "passivation layer", because the Pt thin film electrode seems to be mostly inactive. Since most of the peaks observed in the SNIFTIR spectra for the 1st cathodic scan in the BuMeG3 electrolyte are corresponding to the TFSA anion, the decomposed species should be remained as a surface film of the electrode. Moreover, I think the high overpotential for the magnesium deposition/dissolution process could be due to the passivation layer formed in the BuMeG3 electrolyte solution.

2-3-3. Characterization of the surface film on magnesium metal using XPS

XPS analyses for magnesium metal were carried out to characterize the surface layer. In order to take depth profiles of the surface layer on magnesium metal, an argon ion sputtering was subsequently carried out after each XPS measurement, thus several

stacked spectra are shown in one graph. In the XPS spectra, the top spectrum is corresponding to the very surface and the bottom as bulk. Fig. 2-8 shows the XPS spectra of an as-prepared magnesium foil. The magnesium foil was polished with a slide glass to remove the native passivation layer in an argon filled glove box before the XPS measurement. The Mg 2p spectra for the as-prepared magnesium foil have a broad peak, which obviously consists of two overlapped peaks at 49.6 eV and 51.0 eV. The two peaks at 49.6 eV and 51.0 eV are corresponding to magnesium metal and magnesium oxide respectively. The peak intensity of magnesium and magnesium oxide slightly increased by argon ion sputtering. The O 1s XPS spectra for the as-prepared magnesium foil are shown in Fig. 2-8 (b). Each spectrum also has two overlapped peaks at 531.2 eV and 532.8 eV, corresponding to magnesium oxide and C-O-C bond of organic species respectively. The peaks observed at 286.0 eV and 290.2 eV of C1s spectra are assigned to ether and carbonate respectively. Since the as prepared magnesium foil was polished just before the XPS measurement, the organic species at the surface should be the contamination from the glove box atmosphere. The surface organic species could be the reacted species of the solvent molecules such as THF or DME, evaporated in the glove box. Furthermore, it is obvious that the bulk magnesium foil contains considerable amount of MgO.

The XPS spectra of a magnesium foil immersed in the organohaloaluminate-based electrolyte solution: Ethyl magnesium chloride and diethyl Aluminum Chloride (EAC) electrolyte is shown in the Fig. 2-9. Overall the spectra are similar to the spectra for the as-prepared magnesium foil. The Mg 2p spectra of the magnesium also have two peaks;

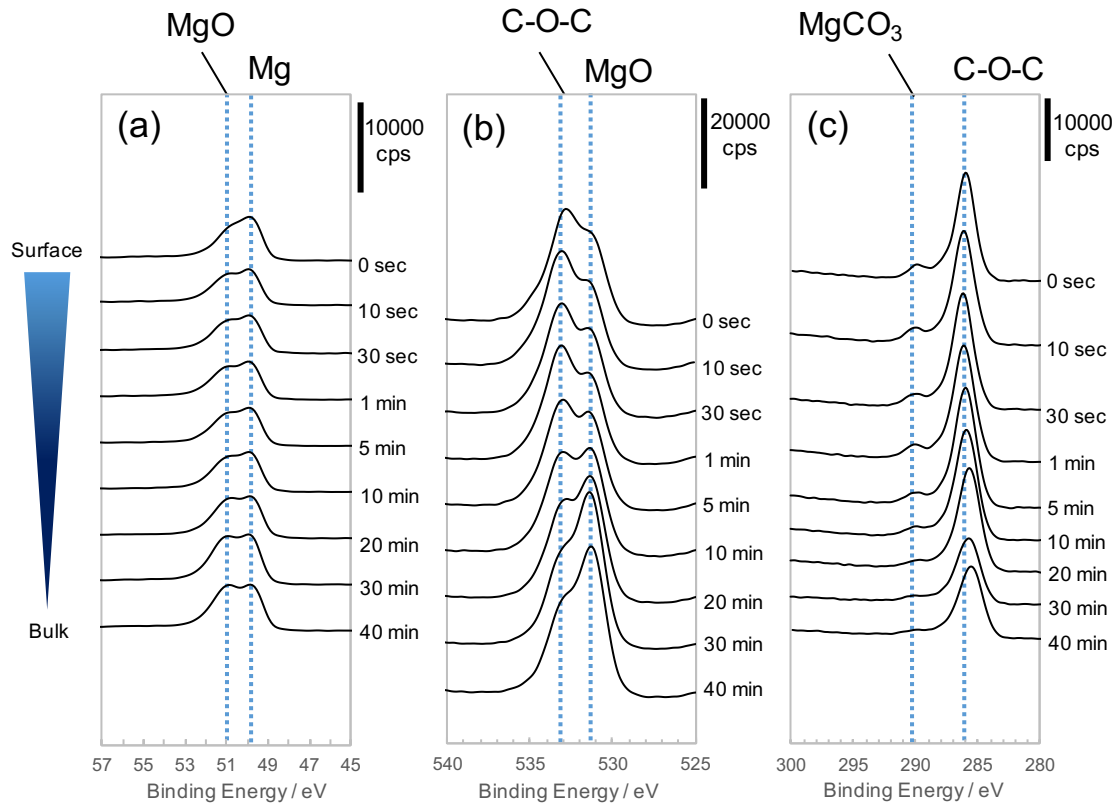

Fig. 2-8 Groups of the XPS spectra for the as prepared Mg metal; Mg 2p (a), O 1s (b), and C 1s (c). The spectrum at the top of the graph corresponds to the very surface of the sample. The following spectra were taken after the Ar ion beam sputtering. The sputtering time is noted at the right side of each spectrum.

one corresponding to magnesium metal at 49.6 eV, and another to magnesium oxide at 51.0 eV. The magnesium oxide was also detected in the O 1s XPS spectra at 531.2 eV. The peak corresponding to C-O-C bond is also observed at 532.8 eV. The C 1s XPS spectra also have peaks assigned to C-O-C bond, and a very small peak of magnesium carbonate. A broad peak is observed in the Cl 2p spectra at 199 eV, suggesting that a magnesium dimer complex formed in the EAC electrolyte adsorbed at the surface of the magnesium. However, the amount of the remaining Cl species is very small. Thus, I think that the XPS spectra do not show clear evidence of the decomposition of the EAC electrolyte at the surface of the magnesium metal, but they show some residual of the electrolyte. These results are in good agreement with the *in situ* FTIR spectra discussed in the previous section.

Fig. 2-10 shows the XPS spectra of a magnesium foil immersed in the ionic electrolyte solution: 0.5 M $Mg(TFSA)_2$ in BuMeG3. At glance, the Mg 2p spectra of the magnesium foil, immersed in the ionic electrolyte, are similar to that of the above two samples. Two peaks corresponding to magnesium metal and MgO are observed as well. Since MgF_2 should be observed around 51.9 eV in the Mg 2p spectra, the XPS peak for the MgO could be overlapped with MgF_2. O 1s spectra also have two overlapped peaks. One at 531.2 eV is corresponding to magnesium oxide, another at 532.8 eV is assigned to C-O-C bond of the solvent molecules. In this case the peak intensity of the C-O-C bond remains strong even after the long argon sputtering process. The C 1s spectra show new peak at 293.8 eV corresponding to C-F bond at the very surface of the magnesium foil. It suggests that the TFSA anion or its derivative is remaining as a residue of the

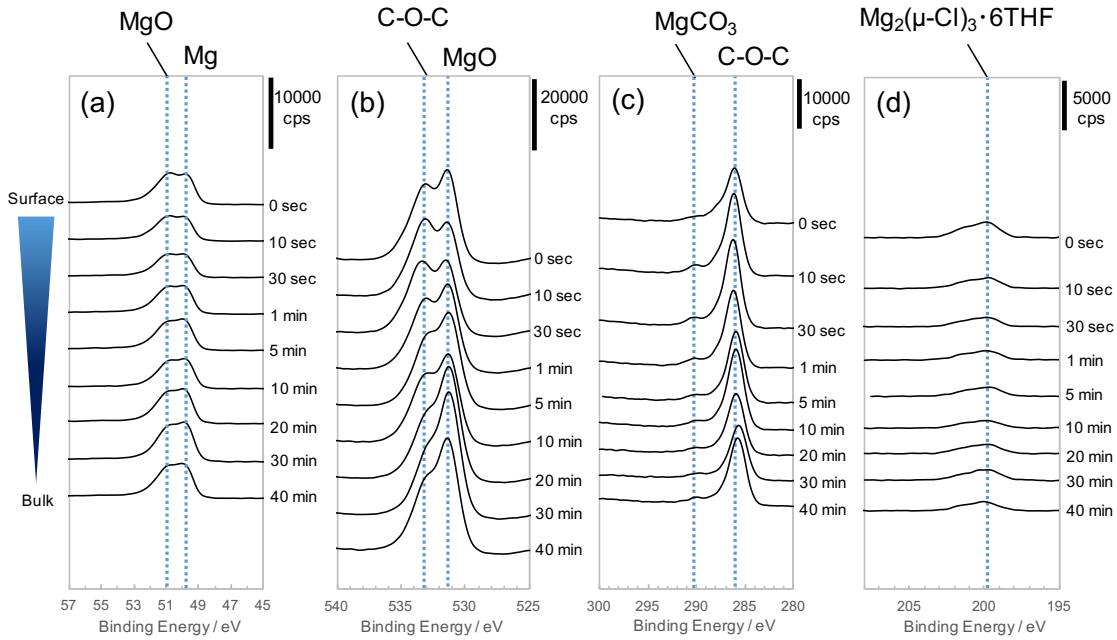

Fig. 2-9 Groups of the XPS spectra for the Mg metal immersed in the 0.25 M EtMgCl-2Et_2AlCl in THF; Mg 2p (a), O 1s (b), C 1s (c) and Cl 2p (d). The Ar ion beam sputtering times are noted at the right side of the graph.

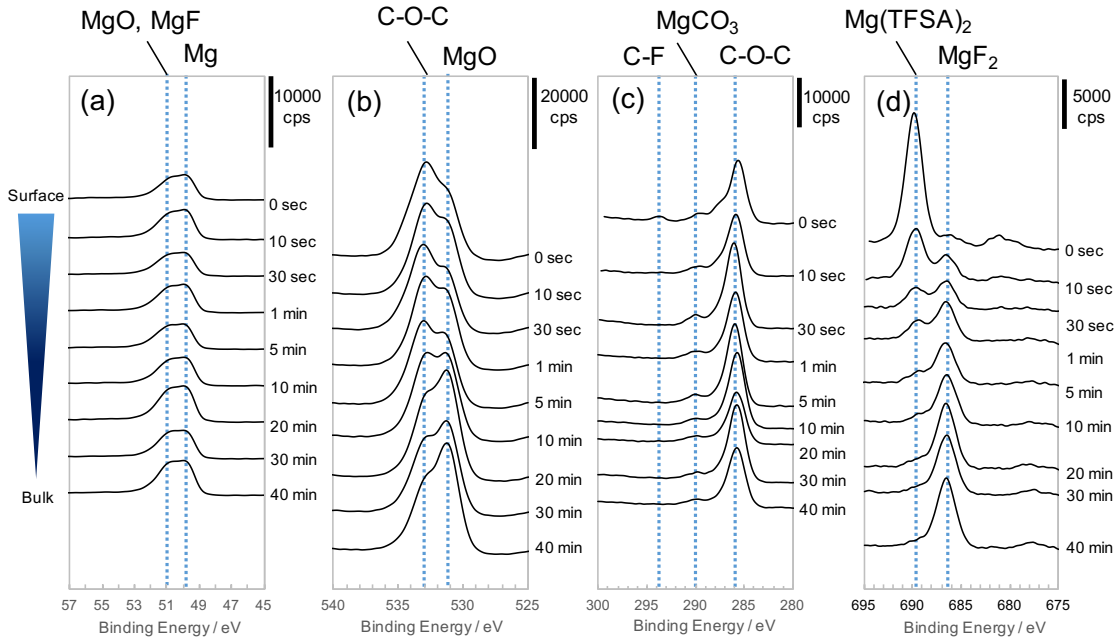

Fig. 2-10 Groups of the XPS spectra for the Mg metal immersed in the 0.5 M $Mg(TFSA)_2$ in BuMeG3; Mg 2p (a), O 1s (b), C 1s (c) and F 1s (d). The Ar ion beam sputtering times are noted at the right side of the graph.

ionic electrolyte solution. The F 1s XPS spectra shown in Fig. 2-10 (d), also have a strong peak corresponding to the TFSA anion at 689.5 eV. During the argon sputtering process, the peak at 689.5 eV gradually disappeared and another peak appeared at 686.2 eV. Though the typical F 1s XPS peak corresponding to MgF_2 should be appeared around 685.7 eV, I think the peak at 686.2 eV is probably corresponding to MgF_2, because many metal fluorides have peaks around 686.0 eV and fluorinated alkyl groups typically have peaks around 689 eV. The formation of MgF_2 clearly shows the decomposition of TFSA anion at the surface of the magnesium metal.

Through the comparison of the XPS spectra for the three samples, the MgF_2-based passivation layer formed via decomposition of the TFSA anion, causes the high overpotential of the deposition/dissolution process of magnesium metal due to the poor electric and ionic conductive properties of MgF_2 [84]. The decomposition of the electrolyte also hinders the crystal growth of the magnesium metal during the deposition process, resulting in the poor crystallinity. Thus, I think the decomposition of the electrolyte solution needs to be suppressed for the smooth electrochemical deposition/dissolution process of the magnesium metal.

2-4. Conclusion

In this chapter, I compared the electrochemical properties of magnesium metal using the EAC electrolyte solution and the ionic electrolyte solution. The EAC

electrolyte solution showed relatively low overpotential approximately 0.34 V, while the ionic electrolyte solution showed very high overpotential >1.5 V. The coulombic efficiency of the EAC electrolyte solution and the ionic electrolyte solution were 99.7 % and approximately 60 % respectively. The magnesium metal deposited in the ionic electrolyte solution showed poor crystallinity due to the reduction of the electrolyte solution during the deposition process. The passivated surface of the deposited magnesium metal via decomposition of the electrolyte solution, hinders the smooth crystal growth of the magnesium. The decomposition process of the electrolyte solutions was analyzed using *in situ* FTIR spectroscopy. The *in situ* FTIR spectra for the EAC electrolyte solution was highly reversible during the CV measurement, suggesting that the surface of the Pt electrode was not passivated. On the other hand, the *in situ* FTIR spectra for the ionic electrolyte solution showed several peaks only at the 1st cathodic scan and no peaks during the following scans. It shows that the electrode surface is passivated during the 1st cathodic scan. Furthermore, the XPS spectra for the magnesium metal immersed in the ionic electrolyte solution proved that TFSA anion in the ionic electrolyte solution was decomposed at the surface of the magnesium metal, resulting in the formation of MgF_2-based passivation layer. Therefore, the high overpotential of the magnesium deposition / dissolution process in the ionic electrolyte solution is caused by the formation of the passivation layer via decomposition of the TFSA anion. I think finding novel anion species with improved reductive stability such as monocarborane [85] is very crucial for further development of rechargeable magnesium batteries.

Chapter 3

Improved Cycling Performance of Intermetallic Anode by Minimized SEI Layer Formation

3-1. Introduction

Alloy anodes including intermetallic anode, such as Si, Sn, Sb or Al, have been widely studied to replace the standard graphite-based anode [54-57]. The biggest challenge of the alloy anode is its cycleability. Huge volume expansion/shrinkage during the lithiation/delithiation process leads the pulverization of the active material particles resulting in loss of the electric contact among active in the electrode.

In order to improve the cycling performance of the alloy anode with high specific capacity, several approaches for the electrode design were tried. The simple and the most practical approach is utilization of new binder material [60-63], which show high adhesive properties compared with polyvinylidenfluoride (PVdF). Another approach is micro- and nanostructural control using 1D or 2D nanomaterials [64-66], which show isotropic volume expansion to release the internal stress.

The electrode/electrolyte interphase is important aspect for the cycleability of the alloy anode, as well. Since redox potential of the anodes are typically <1.0 V vs. Li, solid electrolyte interphase (SEI) layer is formed during the charge/discharge process.

Several research group reported the spectroscopic study of the SEI layer on the Si anode using FEC or VC as electrolyte additives [67-72]. Even with these characterization of the SEI layer, the required physical properties of the SEI layer is still not understood yet.

In order to understand the influence of the SEI layer to the cycleability of the alloy anodes, I think the analogy of Mg-based system is useful, because the organohaloaluminate-based electrolyte solution of the Mg-based system does not form the typical SEI layer [86]. In addition, Arthur *et al.* reported that Mg_3Bi_2 intermetallic anode shows excellent cycleability even at high charge/discharge rate of 1C [73]. Here I conducted a comparative study of bismuth-based intermetallic anode in the lithium-based and magnesium-based system to discuss the role of the SEI layer. I also investigated the cycleability of the Li_3Bi intermetallic anode in 2 $molL^{-1}$ lithium borohydride ($LiBH_4$) in tetrahydrofuran (THF), as a model electrolyte solution of a less SEI system. In addition, a spectroscopic study using *in situ* FTIR was carried out to compare the SEI formation process in the conventional carbonate-based electrolyte solution to the $LiBH_4$-based electrolyte solution.

3-2. Experimental

3-2-1. Preparation of Bi composite electrode

The electrode slurry was prepared by mixing 85 wt.% of Bi powder (Alfa Aesar) and 10 wt.% of acetylene black (TIMCAL), 3.5 wt.% of carboxylmethyl cellulose

(Daicel FineChem) and 1.5 wt.% of styrene butadiene rubber (JSR) with adequate amount of distilled water. The slurry was coated on a copper foil, and dried at 80ºC in air for 2 hours. Subsequently the electrodes punched and vacuum dried at 150ºC for overnight.

3-2-2. Electrochemical measurements of Bi powder electrode

The electrochemical tests were conducted using a two-electrode cell (Tomcell Japan). A magnesium-based electrolyte solution: 0.25 mol dm^{-3} EtMgCl-Et_2AlCl THE by reported procedure [80]. A 1 mol dm^{-3} $LiPF_6$ EC:DEC 1:1 vol.% solution (Kishida) and a 2 mol dm^{-3} $LiBH_4$ THF (Aldrich) are employed for the lithium-based electrolyte solution. Galvanostatic cycling tests of the Bi composite electrodes were performed in the range of 0.0 − 0.6 V for Mg and 0.5 − 1.2 V for Li at room temperature.

3-2-3. in situ FTIR spectroscopy

In situ FTIR spectroscopy was carried out to detect the formation process of the SEI layer. An spectroelectrochemical cell based on diamond ATR (Smiths Detection) set up was employed for the *in situ* FTIR measurement. Detailed *in situ* FTIR set up is reported in chapter 2. As a working electrode, a Ni thin film electrode was coated on the diamond window using DC sputtering coater. The lithium foil was employed for the reference and the counter electrode.

The spectroelectrochemical measurements were carried out during CV measurements of the sweep rate at 0.2 mV sec^{-1}. The CV measurement for the conventional carbonate-based electrolyte was taken between 0.0 and 3.1 V vs. Li/Li^+.

Since the oxidation stability of the $LiBH_4$-based electrolyte is approximately, the potential range for the $LiBH_4$ electrolyte is between 0.0 and 1.7 V vs. Li/Li^+. Each FTIR spectrum was taken by the single beam mode. Subtractive normalized interfacial FTIR (SNIFTIR) spectrum was calculated by the following equation,

$$\Delta R=(R_{n+1}-R_n)/R_n \quad (1)$$

where R_n is a reference reflective spectrum and R_{n+1} is a reflective spectrum at a target electrode potential.

3-3. Results and discussion

3-3-1. Charge/discharge curves of Bi composite electrode

Fig. 3-1 shows charge/discharge curves of the Bi composite electrodes in the three-types of electrolyte solutions during three formation cycles at C/50 (Mg-based system) or C/20 (Li-based system). The Bi composite electrode in the Mg-based system (Fig. 3-1 (a)) shows high charge (magnesiation) capacity of approximately 385 $mAhg^{-1}$ and discharge (demagnesiation) capacity of 360 mAh g^{-1} at the initial cycle. The reversible capacity is in good agreement with the reported data. I think the irreversible capacity is mainly corresponding to the reduction of the native oxide layer at the surface of the Bi particles, because the Mg-based electrolyte solution does not form the SEI layer [86]. The large overpotential in the very beginning of the charging also indicates that the native oxide layer is reduced before the formation of the Mg_3Bi_2 intermetallics. After the

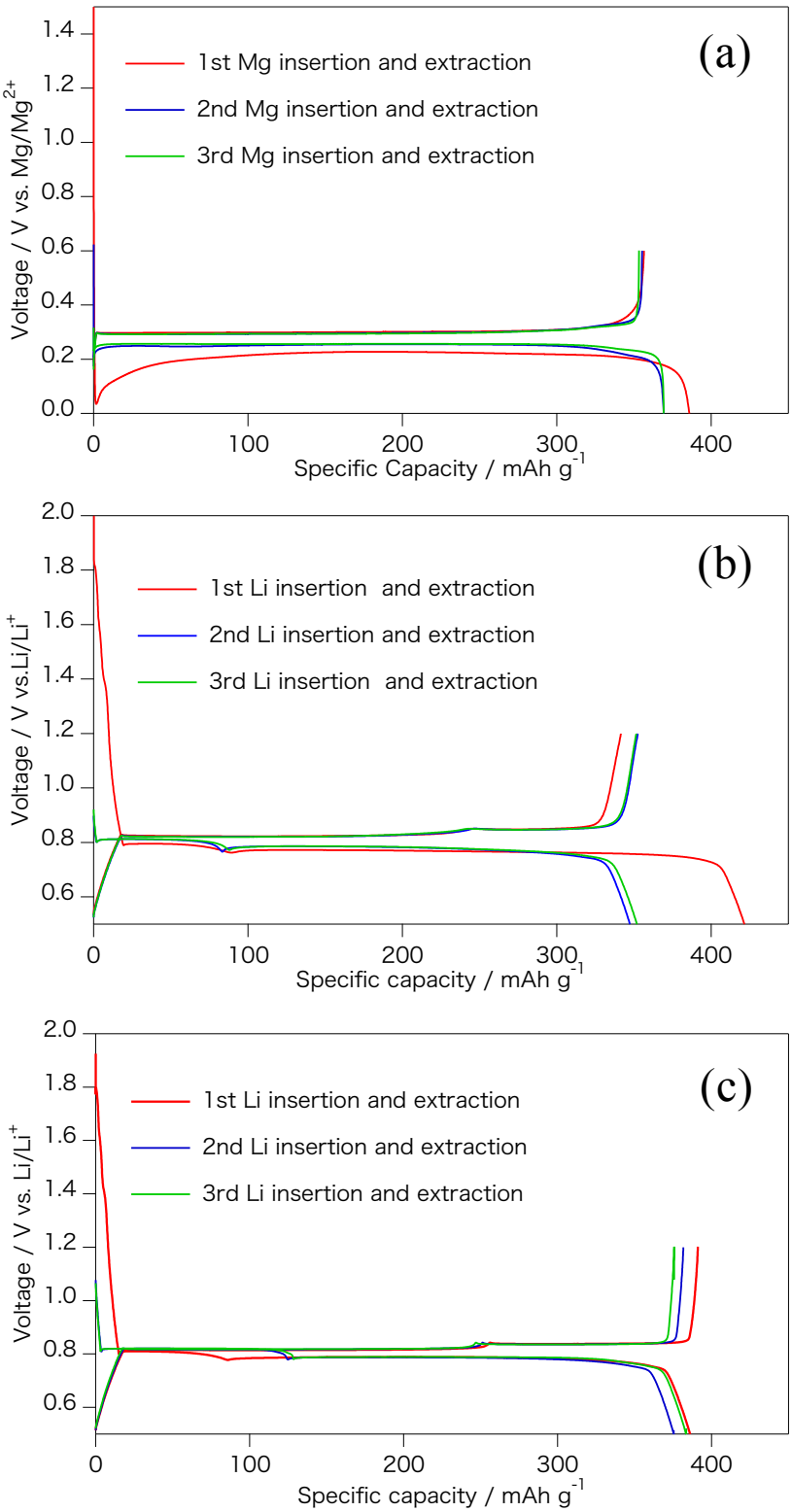

Fig. 3-1 Charging-Discharging profile of Bi-Mg_3Bi_2 at C/50 rate by using 0.25M EtMgCl-2Et_2AlCl in THF (a), Bi-Li_3Bi at C/20 rate by using 1 M $LiPF_6$ in EC:DEC (1:1vol%) (b) and 2 M $LiBH_4$ in THF (c).

reduction of the oxide layer, a voltage plateau appeared at approx. 0.22 V vs. Mg/Mg^{2+}. The charging voltage is relatively lower than the theoretical value at the initial cycle. It is probably due to the low surface area corresponding to the large particle size of the as prepared Bi electrode. The overpotential is, however, significantly decreased in the following cycles, because large volume change during the formation process of Mg_3Bi_2 leads the pulverization of the Bi particles.

Charge discharge curves of the Bi composited electrode in a conventional carbonate-based electrolyte solution and $LiBH_4$ electrolyte are shown in Fig. 3-1 (b) and (c) respectively. The charging curve of the Bi composite electrode in the conventional carbonate-based electrolyte solution has two plateaus. These two plateaus are corresponding to the two step lithiation processes of the Bi composite electrode. The 1st plateau is corresponding to the two-phase reaction of Bi and LiBi, and the 2nd plateau is corresponding to the LiBi-Li_3Bi two-phase reaction. The Bi composite electrode in the carbonate-based electrolyte solution exhibits charge capacity of 410 mAh g^{-1}, and discharge capacity of 330 mAh g^{-1} at the 1st cycle. The high irreversible capacity approximately 20% of the charged capacity suggests that electrolyte solution is reduced to form the SEI layer at the initial charging process. On the other hand, the Bi composite electrode in the $LiBH_4$–based electrolyte solution shows excellent coulombic efficiency of 100% with reversible capacity close to the theoretical capacity of the Bi: 384 mAh g^{-1} at the initial cycle. The high coulombic efficiency suggests that almost no side reaction takes place during the cycles. Hence, I think the electrochemical behavior of the $LiBH_4$-based electrolyte solution is similar to the Mg-based system rather than the conventional

carbonate containing $LiPF_6$.

3-3-2. Cycling performance of the Bi composite electrode

The cycling performances of the Bi composite electrodes in three electrolyte solutions are shown in Fig. 3-2. Even though, typical alloy or intermetallic anodes show poor cycleability due to the pulverization of the active materials, the Bi composite electrode in the Mg system maintained >90% of the reversible capacity after 45 cycles at the charge/discharge rate of 1C as shown in Fig. 3-2 (a). I think the good cycling performance of the Bi composite electrode in the Mg system is due to the high reduction stability of the electrolyte solution, because the surface film is not formed and the pulverized Bi particles still maintains their electrical contact with each other.

On the other hand, the Bi composite electrode in the Li-based system with the conventional carbonate-based electrolyte solution shows poor cycling performance as shown in Fig. 3-2 (b). The electrode initially showed reversible capacity of 270 mAh g^{-1}, but only maintained 77 mAh g^{-1} after 10 cycles, and <10 mAh g^{-1} after the 45^{th} cycle as shown in Fig. 3-2 (b). Fig 3-2 (c) shows the cycling performance of the Bi composite electrode in the $LiBH_4$-based electrolyte solution. The initial cycle showed reversible capacity of 386 mAh g^{-1} and maintained >95% of the reversible capacity even after the 45^{th} cycle. In the analogy of the Mg-based system, I attribute the excellent cycleability of the $LiBH_4$-based electrolyte solution largely to the electrode/electrolyte interphase, because the cell maintained high coulombic efficiency over 45 cycles, while the carbonate-based electrolyte solution typically showed low coulombic efficiency 80-95%

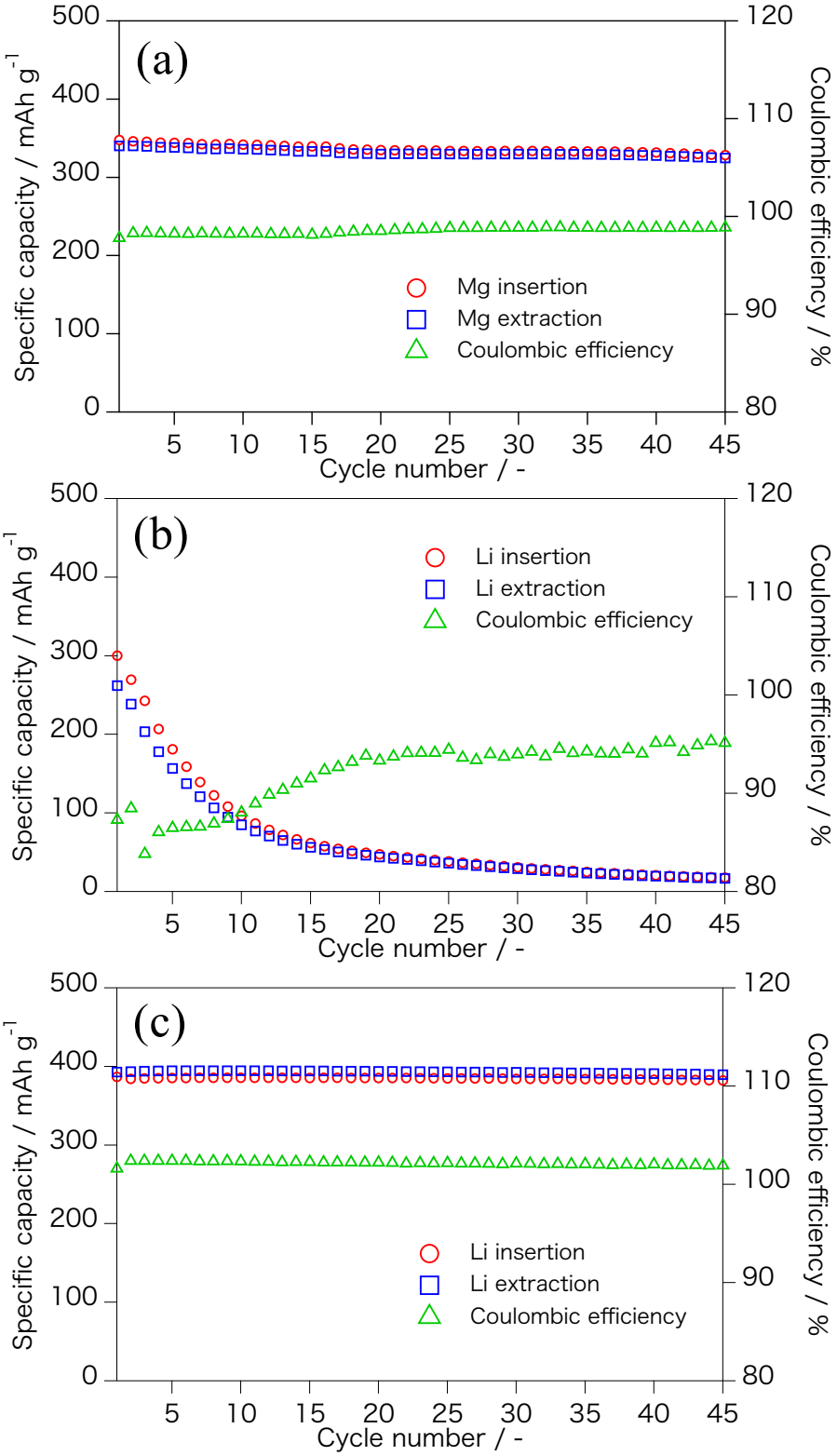

Fig. 3-2 Cycling performance of Bi-Mg_3Bi_2 at 1C rate by using 0.25M EtMgCl-$2Et_2AlCl$ in THF(a), Bi-Li_3Bi at 1C rate by using 1 M $LiPF_6$ in EC:DEC (1:1vol%) (b) and 2 M $LiBH_4$ in THF (c).

during all the 45 cycles.

Fig. 3-3 shows SEM images of the Bi powder (a) and the Bi composite electrodes after the cycling test (b)-(d). The Bi particles in the composite electrodes are severely pulverized after the 45 cycles in all the three electrolyte solutions. Especially the electrode cycled in the carbonate-based electrolyte solution has the smallest submicron sized particles, while the electrodes in the Mg-based electrolyte and the $LiBH_4$-based electrolyte maintains 1-5 μm size particles. I suspect the SEI layer formed in the carbonate-based electrolyte solution accelerates the pulverization of the Bi particles. Once the SEI layer is formed at the new surface of the pulverized particles, the interparticle electrical connection is broken and the electrically isolated particles, which lead the severe capacity fading of the electrode, are formed. The smaller particle size of the Bi composite electrode in the carbonate-based electrolyte solution suggests that the electrode has more isolated particles than the other two electrodes due to the formation of the SEI layer.

3-3-3. Surface analysis of decomposed electrolytes using in situ FTIR spectroscopy

In order to compare the SEI formation process in the two Li-based electrolyte solutions, I conducted *in situ* FTIR spectroscopy. Fig. 3-4 shows *in situ* FTIR spectra of Ni thin film electrode in the conventional carbonate-based electrolyte solution and the $LiBH_4$-based electrolyte solution. The SNIFTIR spectra for the carbonate-based electrolyte shows relatively weak peaks above 0.7 V vs. Li/Li^+ during the initial cathodic scan. All those positive and negative peaks are corresponding to the adsorbed EC and

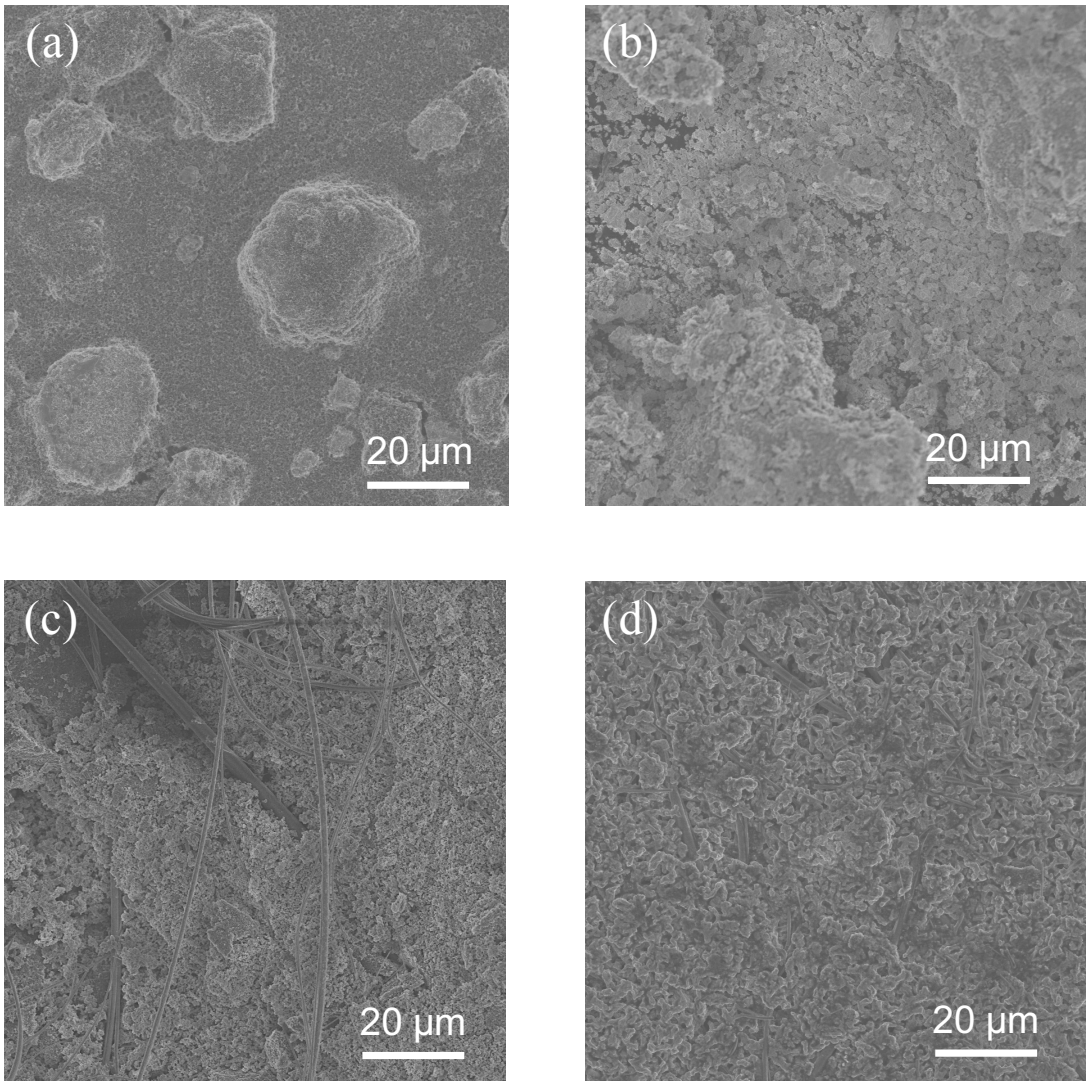

Fig. 3-3 The surface morphology the Bi powder (a) and the Bi composite electrodes after cycling test at 1C rate in 0.25 M EtMgCl-2Et_2AlCl in THF (b), 1 M $LiPF_6$ in EC:DEC (1:1 vol%) (c), and 2 M $LiBH_4$ in THF (d).

DEC molecules at the surface of the electrode. Subsequently, strong positive and negative peaks appeared <0.7 V vs. Li. The strong positive peaks at 1800, 1766 and 1735 cm^{-1} are assigned to the C=O stretching vibration in EC or DEC. The peaks at 1257 and 1155 cm^{-1} are assigned to the C-O asymmetric stretching vibration in EC or DEC. The peak at 1076 cm^{-1} is corresponding to C-O symmetric vibration in DEC, the peak at 842 cm^{-1} is corresponding to P-F stretching vibration in PF_6^- anion. The negative peaks at 1101 and 916 cm^{-1} are corresponding to the new products by decomposed EC or DEC, and the peak at 831 cm^{-1} is assigned to the decomposed PF_6^- anion. Negative peaks around 1400 cm^{-1} are corresponding to the carboxylate derivatives of the decomposed EC or DEC. A summary of the peak assignments for the $LiPF_6$ electrolyte is shown in Table 3-I [87]. The SNIFTIR spectra for the subsequent anodic scan showed only small peaks at 779, 842, and 1072 cm^{-1}, suggesting that the decomposed electrolyte solution <0.7 V vs. Li/Li^+ formed a stable SEI layer. In the following cycle, the SNIFTIR spectra showed several positive and negative peaks. The peak intensity of the SNIFTIR spectra >0.7 V vs. Li/Li^+ is relatively higher than the 1st cycle, while very strong peaks at low electrode potential <0.3 V vs. Li/Li^+ did not appear, because the surface of the Ni electrode is already stabilized with the SEI layer. All the positive peaks observed in the 2nd cycle, are assigned to either EC, DEC or PF_6^- anion in the electrolyte solution. Two broad negative peaks around 1400-1600 cm^{-1} are observed only at low electrode potential <0.3 V vs. Li/Li^+. The peaks are probably corresponding to the reduced products of the electrolyte solution at low electrode potential. The continuous decomposition of the electrolyte solution during the multiple cycles is in good agreement

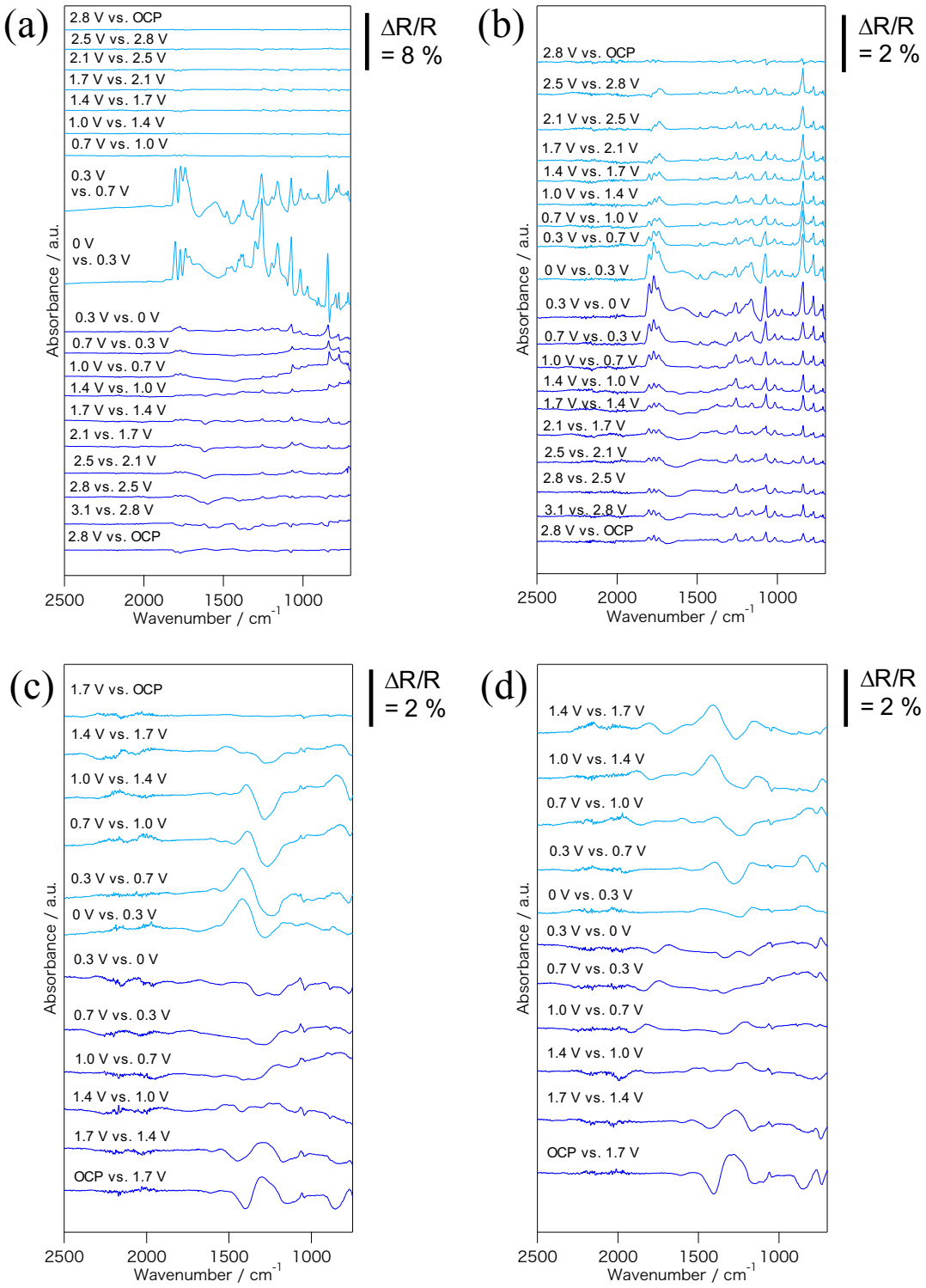

Fig. 3-4 *in situ* FTIR spectra of 1st cycle (a) and 2nd cycle (b) using 1 M $LiPF_6$ in EC:DEC, between the open circuit potential (3.11 V vs. Li/Li^+) and 0 V vs. Li/Li^+ (a), and 1st cycle (c) and 2nd cycle(d) using 2 M $LiBH_4$ in THF (d), between the open circuit potential (1.85 V vs. Li/Li^+) and 0 V vs. Li/Li^+.

with the continuous low coulombic efficiency of the Bi composite electrode in the carbonate-based electrolyte solution.

Fig. 3-4 (c) and (d) shows the SNIFTIR spectra of the $LiBH_4$-based electrolyte solution during CV measurement. A summary of the peak assignment for the $LiBH_4$-based electrolyte solution is shown in Table. 3-II. During the initial cathodic scan, a positive peak at 1400 cm^{-1} and a negative peak at 1260 cm^{-1} are continuously observed. Both of the two peaks are assigned to the lattice vibration of the crystalline $LiBH_4$ [88]. Furthermore, these two peaks subsequently flipped during the anodic scan >1.4 V vs. Li. Since the reversible spectrum change is also observed in the 2nd cycle as shown in Fig. 3-4 (d), I assume that the adsorbed BH_4^- anion at the surface of the electrode, forms an ordered pseudo-crystalline phase, which shows reversible phase transition upon the electrode potential. Further structural analyses are necessary to understand the dynamic behavior of the electrode/electrolyte interphase. Other peaks in the SNIFTIR spectra also showed the dynamic behavior of the THF molecules. The positive peak at 1060 cm^{-1} is assigned to C-O-C asymmetric stretching vibration of the THF molecules during the cathodic scan. The small negative peak approx. 30 cm^{-1} below the positive peak is corresponding to the adsorption of the THF molecules at the surface of the electrode. Both of these peaks also flip during the anodic scan and following cycle. Such reversible spectra changes during the cyclic voltammetry are obviously very different from the spectra observed in the carbonate-based electrolyte solution. Furthermore, the dynamic behavior of the electrode/electrolyte interphase, is typically observed in the electrolyte solution, which does not form the typical SEI layer like Mg-based system.

Table 3-I Summary of the peak assignments of the *in situ* FTIR spectra for 1 M $LiPF_6$ EC:DEC (1:1 vol.%) solution during cathodic scan

cm^{-1}	
	Positive Peaks
1800	C=O stretching vibration in EC
1766	C=O stretching vibration in EC
1735	C=O stretching vibration in DEC
1556	C-H bending vibration in EC
1471	C-H bending vibration in EC
1409	C-H bending vibration in adsorbed or solvated EC or DEC
1384	C-H bending vibration in EC
1380	C-H bending vibration in DEC
1295	C-O asymmetric stretching vibration in adsorbed or solvated DEC
1257	C-O asymmetric stretching vibration in DEC
1189	C-O asymmetric stretching vibration in adsorbed or solvated EC
1155	C-O asymmetric stretching vibration in EC
1076	C-O symmetric stretching vibration in DEC
1020	C-O symmetric stretching vibration in DEC
975	C-O symmetric stretching vibration in EC
906	C-H bending vibration in DEC
842	P-F stretching vibration in $LiPF_6$
798	C-H bending vibration in DEC
779	C-H bending vibration in EC
725	C-H bending vibration in adsorbed or solvated EC
719	C-H bending vibration in EC
	Negative peaks
1563-1344	Carboxylate derivatives of the decomposed EC or DEC
1101	C-O symmetric stretching vibration in decomposed DEC
916	C-H bending vibration in decomposed DEC
831	P-F stretching vibration in decomposed $LiPF_6$

Table 3-II Summary of the peak assignments of the *in situ* FTIR spectra for the 2 M $LiBH_4$ THF solution during cathodic scan

cm^{-1}	
	Positive Peaks
1400	Lattice vibration of the crystalline $LiBH_4$
1060	C-O-C asymmetric stretching vibration of free THF
835	C-H bending vibration of THF
	Negative peaks
1260	Lattice vibration of the crystalline $LiBH_4$
1025	C-O-C asymmetric stretching vibration of solvated THF
885	C-H bending vibration of THF
761	CH_2 bending vibration of THF

Therefore, I conclude that the $LiBH_4$-based electrolyte solution is a kind of the less-SEI system and the excellent cycling performance of the Bi composite electrode in the $LiBH_4$-based electrolyte solution is mainly due to the less SEI layer.

3-4. Conclusion

In the present chapter, I investigated how the SEI layer affects to the cycling performance of the intermetallic anode using the Bi composite electrode in the three electrolyte solutions. In the Mg-based system, the Bi composite electrode shows high overpotential in the initial charging process. The overpotential significantly decreased by the pulverization of the Bi particles in the following charge/discharge process with the reversible capacity approx. 360 $mAhg^{-1}$. The electrode maintains high coulombic efficiency >98%, without capacity fading during the 45 cycles. The electrode in the conventional carbonate-based electrolyte solution shows poor reversibility and severe capacity fading, suggesting the continuous electrolyte decomposition due to the volume change of the Bi particles. On the other hand, the electrode in the $LiBH_4$-based electrolyte solution shows the excellent cycling performance, with the high coulombic efficiency.

After the cycling test, the Bi particles in the composite electrodes are severely pulverized. The electrode cycled in the carbonate-based electrolyte solution especially has the smaller particle size compared with other electrodes. I suspect the SEI layer

formed at the surface of the pulverized particles initiates the electrical isolation of the particles in the electrode, resulting in the capacity fading.

In situ FTIR spectroscopy was carried out to confirm the SEI formation process in the carbonate-based electrolyte solution and the $LiBH_4$-based electrolyte solution. The carbonate-based electrolyte solution showed very strong peaks corresponding to the formation of the SEI layer at the electrode potential <0.7 V vs. Li/Li^+. The *in situ* FTIR spectroscopy also proved that the $LiBH_4$-based electrolyte solution does not form typical SEI layer. Based upon the present study, I propose that electrolyte solution which forms less SEI layer is preferred system for the improvement of the cycling performance of the intermetallic anodes.

Chapter 4

Surface and Bulk Instability of Magnesium-based Intermetallic Anode for Improved Reversibility

4-1. Introduction

The conventional ionic electrolyte solutions based on magnesium bis(trifluoromethanesulfonyl)amide ($Mg(TFSA)_2$) were reported as an alternative electrolyte solution of corrosive properties-free [50-52]. The electrolyte solutions deposit magnesium, however, high overpotential > 1 V during the magnesium deposition/dissolution process was observed in the electrolyte solutions. Therefore, another anode active materials with smooth oxidation/reduction reaction are need for development of rechargeable magnesium and magnesium-ion batteries.

A candidate of another anode active materials is magnesium intermetallic compound anodes. The magnesium intermetallic compound anodes have been studied by researchers. Electrodeposited bismuth (Bi), antimony (Sb) and $Bi_{1-x}Sb_x$ as magnesium alloy-based anodes were firstly reported by Arthur et al. [73]. The electrodeposited Bi and Sb formed Mg_3Bi_2 and Mg_3Sb_2 respectively. The Mg_3Bi_2 demonstrated highly reversible magnesium insertion/extraction process in the both electrolyte solutions: the organohaloaluminate-based electrolyte solution and the

conventional ionic electrolyte solution of $Mg(TFSA)_2$ in acetonitrile. Nevertheless, it was reported that the Mg_3Sb_2 demonstrated rapid capacity fade, the Mg_2Sn showed large irreversibility, the Mg_2Pb had poor coulombic efficiency. Thus, the Mg_3Bi_2 is the best anode active materials for magnesium-ion batteries.

The number of the magnesium intermetallic compound anodes for rechargeable magnesium and magnesium-ion batteries are limited by the passivation layer and a strongly ionic interaction with the Mg^{2+} ion. From chapter 2, the passivation layer formed on the active materials leads to the low reversible Mg^{2+} insertion and extraction process. In addition, difficulty of smooth Mg^{2+} insertion and extraction in host compounds is due to the ionic interactions. Therefore, the stability of the surface layer and the bulk structure affects the activity of magnesium intermetallic compounds.

In this chapter, I performed a comparative study of the Mg_3Bi_2 and the Mg_3Sb_2 which is same crystal structure. I focused on the surface of materials and the bulk stability of the Mg_3Bi_2 and Mg_3Sb_2, and investigated why the Mg_3Bi_2 shows good electrochemical properties in the conventional ionic electrolyte solution.

4-2. Experimental

4-2-1. Synthesis and characterization of Mg_3Bi_2 and Mg_3Sb_2

A Magnesium bismuth (Mg_3Bi_2) and a magnesium antimony (Mg_3Sb_2) powders were synthesized by conventional solid-state reaction. A stoichiometric amount of

magnesium powder, 10 wt.% of additional magnesium powder and bismuth powder or antimony powder were mixed in an agate mortar, then the powders were ball-milled by Planetary mills (PL-7 Premium Line, Fritsch Japan Co. Ltd.) for eight hours at 400 rpm. The powders were pelletized under 20 MPa for one minute, subsequently, the pellet was calcined at 550 ℃ for five hours under an argon atmosphere. In order to obtain the Mg_3Bi_2 or Mg_3Sb_2 powder, the calcined pellet was pulverized by the mortar. All operations were carried out in the argon-filled glovebox. X-ray diffraction patterns were obtained by Bruker D8 Advance equipped with Cu-Kα radiation. To avoid the water influence in air, the calcined powders were measured in a holder kept ambient atmosphere. The collected data was analyzed using Rietveld refinement with RIETAN-FP ver. 2.84. A stability of passivate layer on surface was investigated by time history of XRD measurement in air.

4-2-2. Electrochemical test of Mg_3Bi_2 and Mg_3Sb_2

Mg_3Bi_2 or Mg_3Sb_2 composite electrodes were prepared by mixing 80 wt.% of the active materials, 10 wt.% of acetylene black (Super P Li, TIMCAL) and 10 wt.% of poly imide binder (LV-042, TORAY) dissolved in anhydrous NMP. The black slurry was cast on a copper foil in the argon-filled glove box and dried at 80 ℃ in vacuum for 2 hours to remove the NMP. The electrodes were obtained after imide reaction in the argon atmosphere at 350 ℃ for 1 hour.

Electrochemical measurements were performed by a three-electrode cell with the composite electrode, a platinum foil counter electrode and a Ag/Ag^+ reference electrode

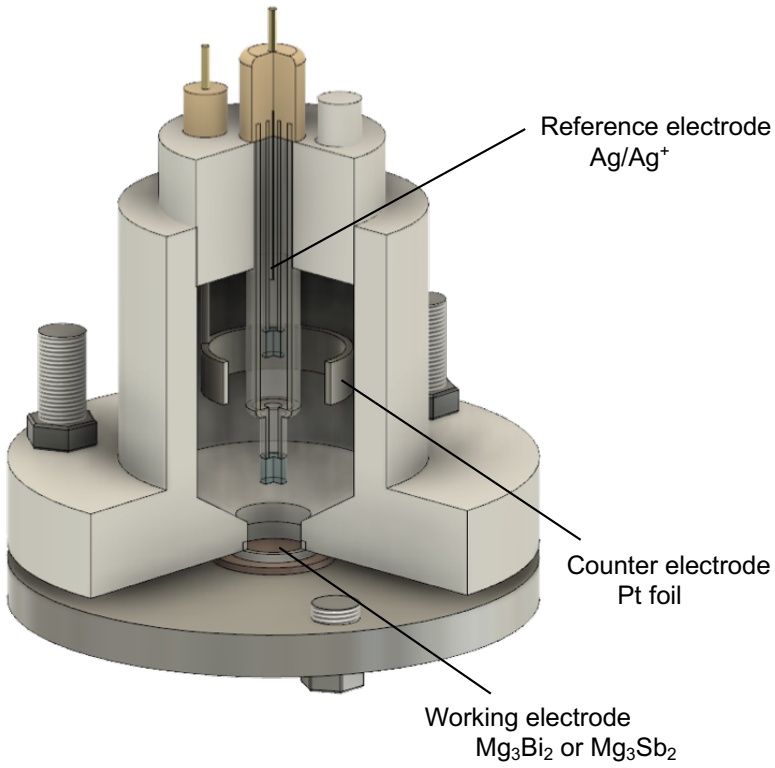

Fig. 4-1 Schematic representative of the three-electrode cell used in the chapter

(EC Frontier Co. Ltd.) as shown in Fig. 4-1. A silver wire inserted in 0.05 M $AgNO_3$ in acetonitrile was used as the Ag/Ag^+ reference electrode. A 1 M $Mg(TFSA)_2$ in acetonitrile(AN) (Kishida Co.) was used as conventional ionic electrolyte solution. Electrochemical properties were evaluated by cyclic voltammetry (CV). Measurement range of CVs was -2.4 – -1.5 V vs. Ag/Ag^+ reference electrode with sweep rate of 0.1 mV sec^{-1} at room temperature.

4-3. Results and Discussion

3-1. Synthesis and electrochemical test of Mg_3Bi_2 and Mg_3Sb_2

Fig. 4-2 shows X-ray diffraction patterns of the synthesized Mg_3Bi_2 and Mg_3Sb_2 powders normalized with 101 reflection. Both of the diffraction patterns well matched with the simulated powder pattern of Mg_3Bi_2 and Mg_3Sb_2 from database (Mg_3Bi_2: ICSD 659569, Mg_3Sb_2: ICSD 2142, Space group: *P*-3*m*1). The XRD patterns of the Mg_3Bi_2 and the Mg_3Sb_2 had a little orientation at 001 and 002 reflection peaks of *c* axis. Impurities peaks such as magnesium and bismuth or antimony were not observed in the diffraction patterns, suggesting that the Mg_3Bi_2 and Mg_3Sb_2 powders were successfully synthesized by solid-state reaction without electrochemical insertion of Mg^{2+} ion to bismuth or antimony.

Fig. 4-3 (a) and (b) show the cyclic voltammograms (CVs) of the Mg_3Bi_2 and Mg_3Sb_2 electrodes in a conventional ionic electrolyte solution of 1 M $Mg(TFSA)_2$ in

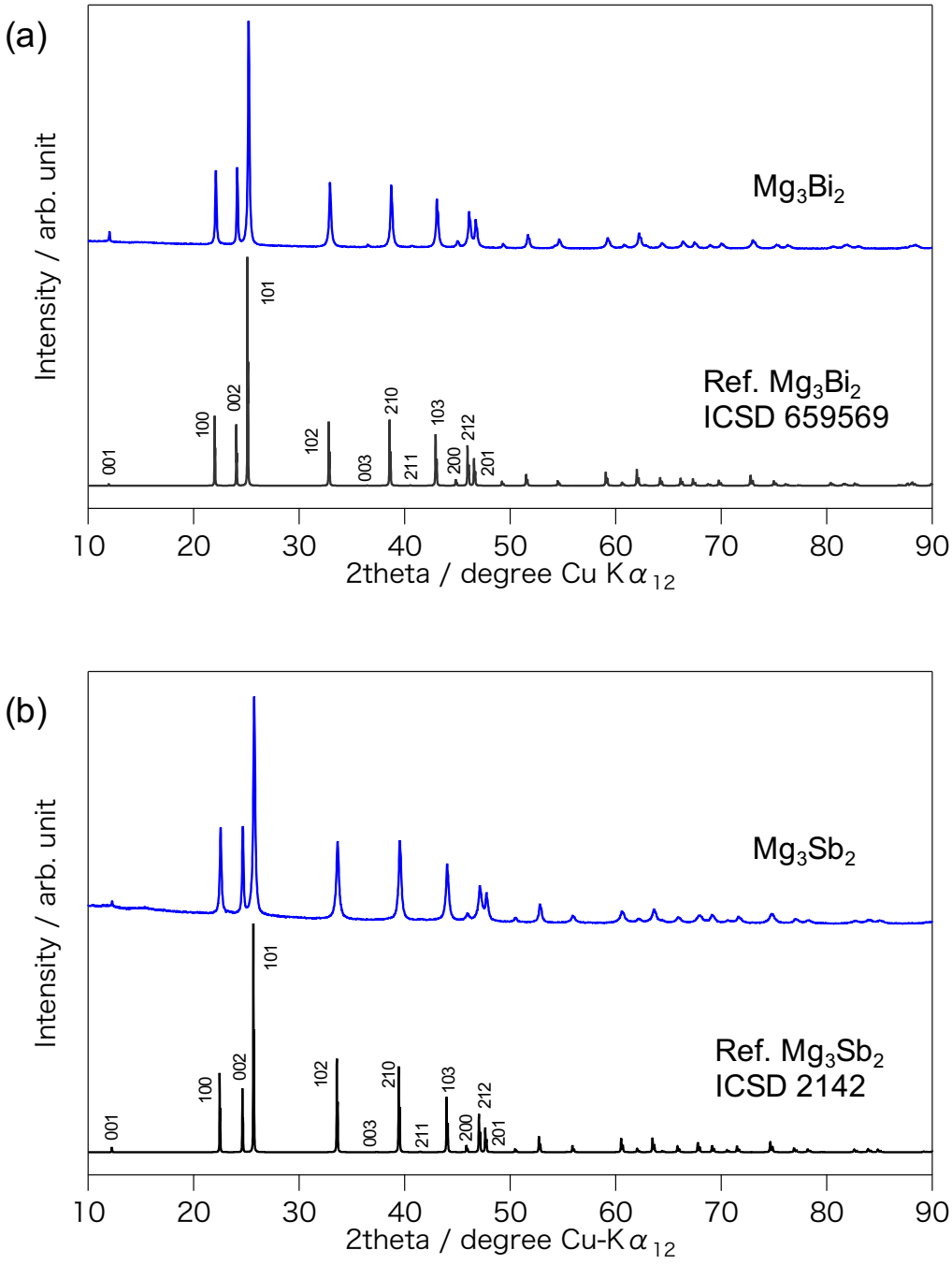

Fig. 4-2 XRD patterns of the Mg_3Bi_2 and Mg_3Sb_2. The patterns were normalized with101 reflection.

AN. The Mg_3Bi_2 electrode showed good agreement with previous report using electrodeposited bismuth electrode [73], and had a cathodic current at −2.13 V vs. Ag/Ag^+ reference electrode and an anodic current at −2.03 V vs. Ag/Ag^+ reference electrode. The cathodic and anodic current is corresponding to insertion and extraction reaction of Mg^{2+} ion. The Mg_3Bi_2 electrode showed high coulombic efficiency of 94.8 %, while the poor coulombic efficiency of 60 % was observed in the magnesium deposition/dissolution process [86]. In addition, a overpotential between Mg^{2+} ion insertion/extraction of the Mg_3Bi_2 electrode was approximately 0.05 V, whereas the high overpotential above 1 V between magnesium deposition/dissolution process was observed in the conventional ionic electrolyte solution [86]. It suggests that the cathodic and anodic reaction for Mg^{2+} ion of the Mg_3Bi_2 electrode is easily occurred in the conventional ionic electrolyte solution compared with the magnesium deposition/dissolution process. The CV of the Mg_3Sb_2 electrode in the 1 M $Mg(TFSA)_2$ in AN is shown in Fig. 4-3 (b). The Mg_3Sb_2 electrode had cathodic and anodic current assigned insertion and extraction of Mg^{2+} ion at −2.26 V and −1.00 V vs Ag/Ag^+ reference electrode respectively. However, the cathodic and anodic reaction of the Mg_3Sb_2 electrode were extremely smaller current density, lower coulombic efficiency of 18.0 % and higher overpotential approximately 0.27 V than that of the Mg_3Bi_2 electrode in the conventional ionic electrolyte solution. It was reported that the electrodeposited antimony using an EAC electrolyte solution showed rapidly poor cyclability [73], suggesting that an activity for an anode active material of the Mg_3Sb_2 is low in the both electrolyte solutions while the Mg_3Bi_2 and Mg_3Sb_2 have same structure

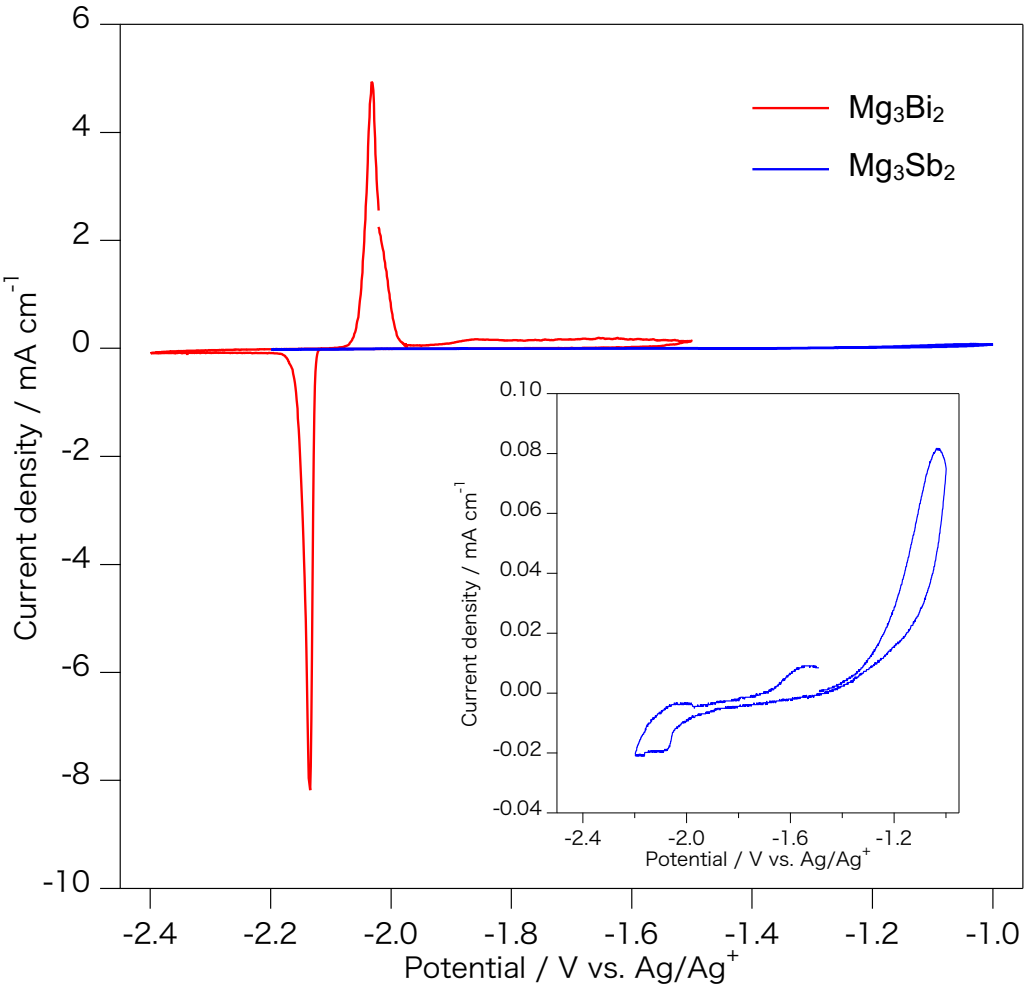

Fig. 4-3 CV of the Mg_3Bi_2 (red) and Mg_3Sb_2 (blue) electrode in the 1 M $Mg(TFSA)_2$ in AN. Scan rate was 0.1 mV sec^{-1}.

of the *P*-3*m*1 space group. I think the activity of the Mg_3Bi_2 and the Mg_3Sb_2 were affected by a passivation layer at surface and stability of the bulk. Especially, the passivation layer formed at surface is no ionic conductive properties in the magnesium rechargeable batteries. In the case of magnesium deposition/dissolution process, the conventional electrolyte solution using $Mg(TFSA)_2$ is easily decomposed, and formed a MgF_2-based passivation layer at the surface of magnesium [86]. The MgF_2-based passivation layer prevents smooth electrochemical deposition/dissolution process of the magnesium metal. However, the CV of Mg_3Bi_2 electrode in the conventional ionic electrolyte solution using $Mg(TFSA)_2$ exhibited high coulombic efficiency and small overpotential between insertion and extraction of Mg^{2+} ion. It is considered that passivation layer via decomposition of TFSA anion is scarcely formed at the surface of the Mg_3Bi_2 and the Mg_3Sb_2 during the potential for the insertion/extraction of Mg^{2+} ion. Hence, the activity of the Mg_3Bi_2 and the Mg_3Sb_2 is affected by the surface stability forming the passivation layer on oneself. Moreover, the choice of anode and cathode materials for magnesium batteries is extremely limited because Mg^{2+} ion has strong ionic interaction, resulting in difficulty of Mg^{2+} ion diffusion in bulk of structure. Thus, there is a possibility that a stability of bulk in the structure is affected to the activity of the Mg_3Bi_2 and the Mg_3Sb_2.

3-2. Surface stability of Mg_3Bi_2 and Mg_3Sb_2

In order to confirm the surface stability of the Mg_3Bi_2 and the Mg_3Sb_2, I carried out time dependence changes of the powders stored in air by XRD. The XRD pattern for

time dependence changes of the Mg_3Bi_2 powder stored in air were shown in Fig. 4-4 (a). The diffraction patterns were normalized with 101 reflection at 25.4 ° of 2θ. The diffraction pattern of the Mg_3Bi_2 stored in air for 0 hour hardly observed a change by exposing air, compared with the diffraction pattern of the Mg_3Bi_2 in the argon atmosphere. The diffraction pattern in the air for 24 hours also showed the same diffraction pattern in the argon atmosphere. Since I think that the surface activity of the Mg_3Bi_2 is exceedingly slow, I performed addition of water to accelerate a reaction. The diffraction pattern of the Mg_3Bi_2 adding water for 0 hour observed a peak corresponding to bismuth. After 72 hours, the peak corresponding to bismuth was larger than the peak at 101 reflection of the Mg_3Bi_2. Hence, I consider that extremely small amount of the passivation layer is formed at the surface of the Mg_3Bi_2 because the Mg_3Bi_2 showed a phase separation to bismuth metal in the air. Fig. 4-4 (b) shows the XRD pattern for time dependence changes of the Mg_3Sb_2 powder stored in the air. The diffraction patterns were normalized at 101 reflection at 25.5 ° of 2θ. The diffraction patterns of the Mg_3Sb_2 stored in the air showed same diffraction pattern as the pattern of Mg_3Sb_2 in the argon atmosphere. In addition, the diffraction patterns of the Mg_3Sb_2 adding water for 0 hour and 72 hours scarcely had remarkable changes, while the reaction was accelerated. It suggests that the surface of the Mg_3Sb_2 is more stable than that of the Mg_3Bi_2. I think that the passivation layer is formed at the surface of the Mg_3Sb_2 because it did not find a change such as phase separation. Therefore, the surface stability affects the activity of the Mg_3Bi_2 and the Mg_3Sb_2, resulting in the low overpotential and high coulombic efficiency of the Mg_3Bi_2 electrode.

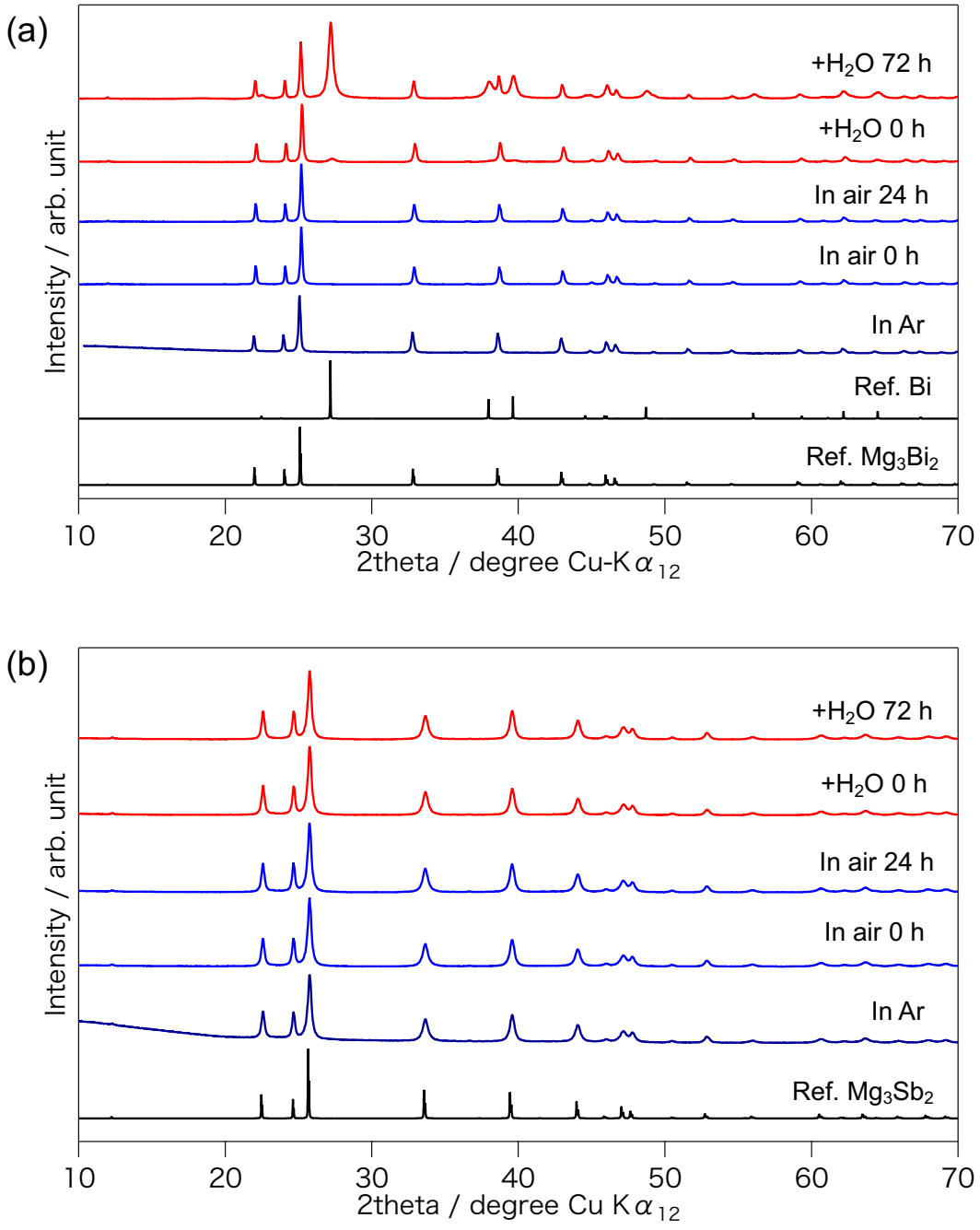

Fig. 4-4 XRD patterns of the Mg_3Bi_2 (a) and Mg_3Sb_2 (b) stored in air. Stored time is noted at right side.

3-3. Bulk stability of the Mg_3Bi_2 and Mg_3Sb_2 structure

Rietveld refinements were carried out for investigation of the bulk stability of the materials. A-type rare earth structure with the *P*-3*m*1 space group was chosen as the structure model. Mg is located at 1*a* site (0, 0, 0) and 2*d* site (0.33333, 0.66667, *z*) with $z \approx 0.63$, and Bi and Sb are located at 2*d* site (0.33333, 0.66667, *z*) with $z \approx 0.22$. The refinement results of the Mg_3Bi_2 and Mg_3Sb_2 as shown in Fig. 4-5, Table 4-I and 4-II. The refinements showed good fit the observed and calculated patterns, because the refinement results of the Mg_3Bi_2 and the Mg_3Sb_2 had the reliable factor, R_{wp} values of 6.19 % and 7.15 %, respectively. The refinements exhibited the refined lattice parameter of a = 4.65349(5) Å, c = 7.38992(9) Å in the Mg_3Bi_2, a = 4.55962(9) Å, c = 7.22933(16) Å in the Mg_3Sb_2. Magnesium atoms of the Mg_3Bi_2 and the Mg_3Sb_2 were occupied at two sites; one is 1*a* site of octahedral site, the other is 2*d* site of tetragonal site. In the case of the Mg_3Bi_2, the magnesium cations existed on 1*a*(0, 0, 0) and 2*d*(0.33333, 0.66667, 0.63187(61)). The magnesium cations of the Mg_3Sb_2 were 1*a*(0, 0, 0) and 2*d*(0.33333, 0.66667, 0.63501(51)). It suggests that 2*d* site of magnesium cation in the Mg_3Sb_2 is shifted, compared with the site of magnesium cation in the Mg_3Bi_2.

Fig. 4-6 show bond lengths of magnesium-bismuth and magnesium-antimony at 2*d* site and 1*a* site in the Mg_3Bi_2 and the Mg_3Sb_2 refined by Rietveld refinement. The bond lengths of magnesium-bismuth and magnesium-antimony at 1*a* site showed similar values (Mg_3Bi_2: 3.158 Å, Mg_3Sb_2: 3.112 Å). However, the bond lengths at 2*d* site were 3.006 Å and 2.888 Å in the Mg_3Bi_2, 2.925 Å and 2.809 Å in the Mg_3Sb_2. It shows that the interaction between magnesium and bismuth is weaker than the interaction between

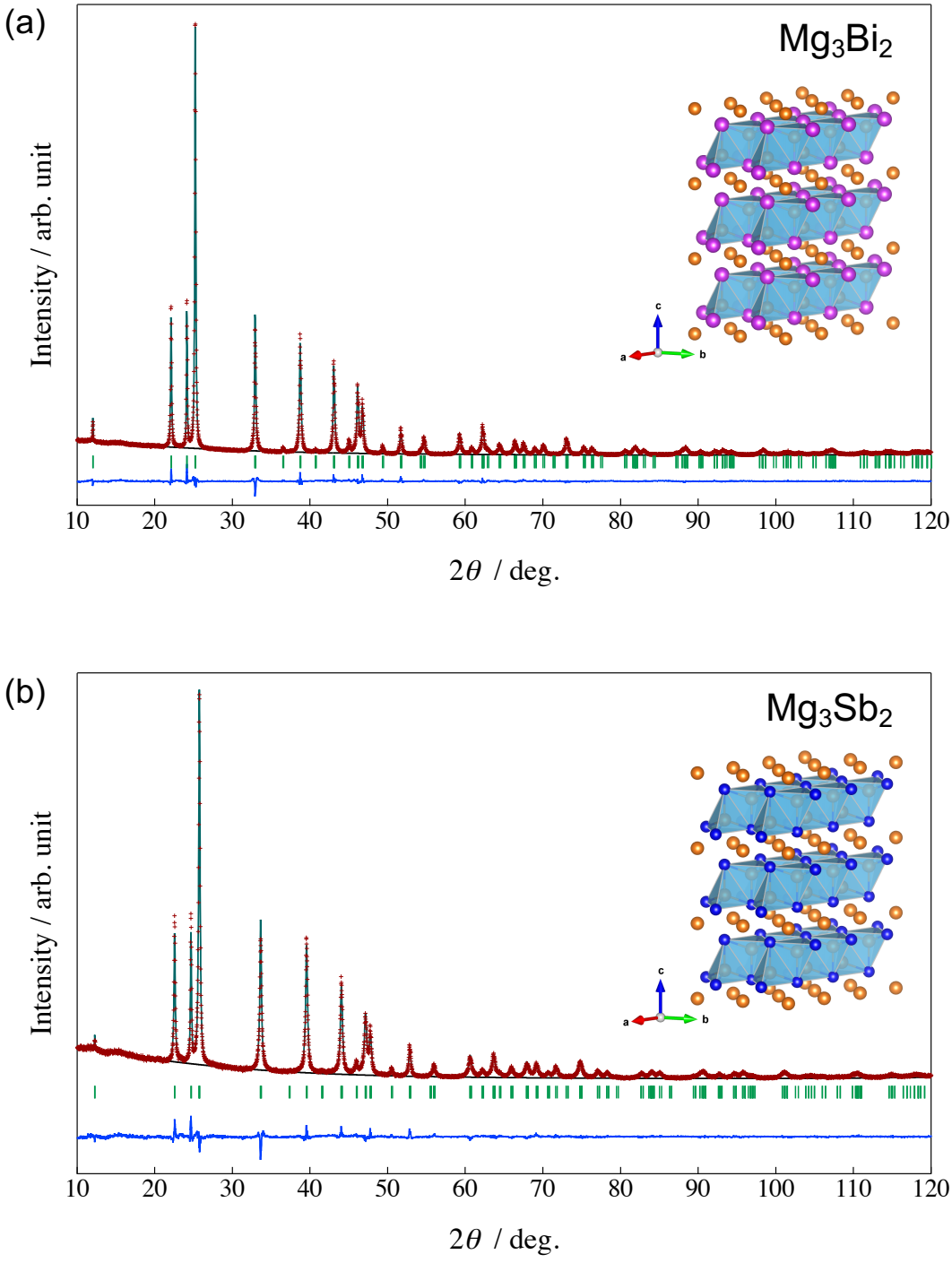

Fig. 4-5 Rietveld refinement results of the Mg_3Bi_2 (a) and Mg_3Sb_2 (b). (+) Observed and (－) calculated values.

Table 4-I X-ray Rietveld refinement result for Mg_3Bi_2. The XRD pattern was fitted using space group of *P*-3*m*1.

Atom	Site	*g*	*x*	*y*	*z*	*B*(Å)
Mg(1)	1*a*	1	0	0	0	1.5
Mg(2)	2*d*	1	0.33333	0.66667	0.63187(61)	1.5
Bi(1)	2*d*	1	0.33333	0.66667	0.22473(10)	0.9

a = 4.65349(5) Å, c = 7.38997(9) Å, R_{wp} = 6.19 %, R_p = 4.74 %, S = 1.45

Table 4-II X-ray Rietveld refinement result for Mg_3Sb_2. The XRD pattern was fitted using space group of *P*-3*m*1.

Atom	Site	*g*	*x*	*y*	*z*	*B*(Å)
Mg(1)	1*a*	1	0	0	0	1.2
Mg(2)	2*d*	1	0.33333	0.66667	0.63501(51)	1.2
Sb(1)	2*d*	1	0.33333	0.66667	0.22979(15)	0.9

a = 4.55963(10) Å, c = 7.22933(16) Å, R_{wp} = 7.15 %, R_p = 5.50 %, S = 1.36

magnesium and antimony. Hence, I consider that the diffusion of Mg cation of the Mg_3Bi_2 is smooth because the magnesium cation is relatively weak interaction with bismuth anion.

In order to evaluate the electron density of the bulk structure of the Mg_3Bi_2 and the Mg_3Sb_2, Maximum-Entropy Method (MEM) analysis were performed. The electron density distribution by MEM analysis results are shown in Fig. 4-7. The electron isosurface level was 3.0 $Å^{-3}$. A three-dimensional electron density distribution of the Mg_3Bi_2 (Fig. 4-7 (b)) had spheres corresponding to magnesium cation and bismuth anion, however, the less distribution was observed in a distance between magnesium cation and bismuth anion. The three-dimensional electron density distribution of Mg_3Sb_2 (Fig. 4-7 (e)) was almost surrounded by the electron, scarcely found positions of magnesium ion and antimony anion. In addition, in order to check the electron density in the structure, two-dimensional electron density distributions sliced at the (010) plane were also shown in Fig. 4-7 (c) and (f). In the distribution of Mg_3Bi_2, the magnesium cation at 2*d* site and bismuth anion were low electron density, whereas the magnesium cation at 1*a* site was high electron density. The distribution of Mg_3Sb_2 was high electron density in the magnesium cation not only 2*d* site but also 1*a* site. It shows that the magnesium cation at 2*d* site of the Mg_3Bi_2 were less interaction with bismuth anion. On the other hand, the magnesium cation at 2*d* site of the Mg_3Sb_2 is strong interaction with antimony. I think that the diffusion capability of the magnesium cation of the Mg_3Bi_2 is smooth, resulting in the high activity of the Mg_3Bi_2 in the conventional ionic electrolyte solution. Thus, the activity of the Mg_3Bi_2 and the Mg_3Sb_2 is also affected by the bulk stability.

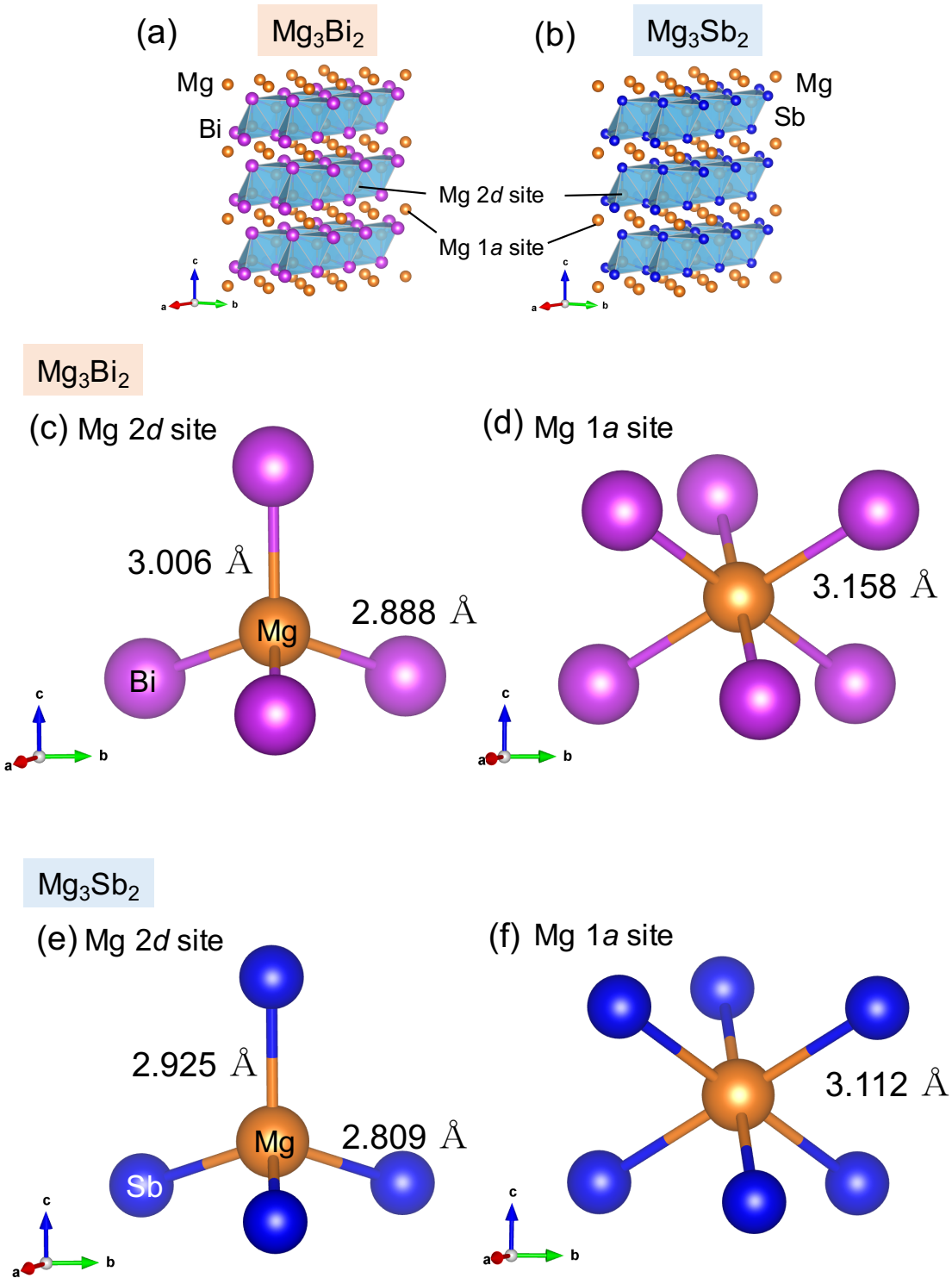

Fig. 4-6 Crystal structure model of the Mg_3Bi_2 (a) and Mg_3Sb_2 (b). The bond length of magnesium-bismuth at 2d site (c) and 1a site (d). The bond length og magnesium-antimony at 2d site (e) and 1a site (f).

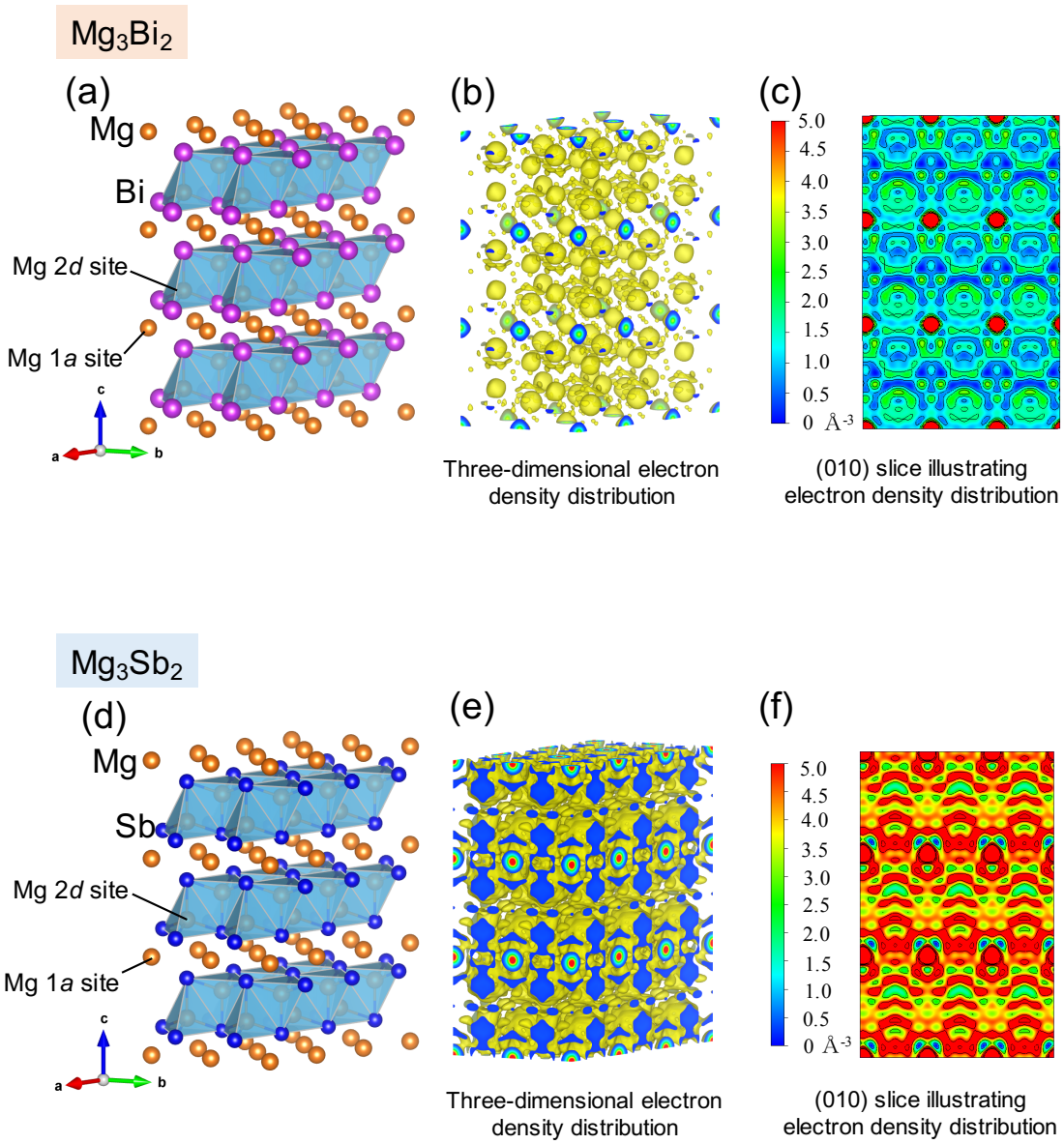

Fig. 4-7 Crystal structure model of the Mg_3Bi_2 (a) and Mg_3Sb_2 (d). The three-dimensional electron density distribution calculated by MEM analysis of the Mg_3Bi_2 (c) and the Mg_3Sb_2 (e). The distribution sliced at (010) plane of the Mg_3Bi_2 (d) and the Mg_3Sb_2 (f).

4-4. Conclusion

In this chapter, I compared the same structure of Mg_3Bi_2 and the Mg_3Sb_2, and investigated why the Mg_3Bi_2 shows reversible insertion and extraction of magnesium cation in the conventional electrolyte solution using $Mg(TFSA)_2$. The Mg_3Bi_2 and the Mg_3Sb_2 were synthesized by conventional solid-state reaction, and identified by XRD pattern. The cyclic voltammetry tests were performed in the 1 M $Mg(TFSA)_2$ in AN. The Mg_3Bi_2 electrode showed high coulombic efficiency of 94.8 % and low overpotential approximately 0.05 V, whereas the Mg_3Sb_2 electrode had low coulombic efficiency of 18.0 % and relatively high overpotential approximately 0.27 V. It is considered that the high electrochemical performance of the Mg_3Bi_2 is affected to the low surface stability and the low bulk stability. The surface stability was investigated by time dependence changes by XRD. The XRD patterns of Mg_3Bi_2 exhibited a phase separation to bismuth in air. However, remarkable changes were scarcely observed in the XRD patterns of Mg_3Sb_2. It suggests that the passivation layer is extremely formed at the surface of the Mg_3Bi_2. I consider that the surface stability by forming passivation layer is substantially affected to the anodes for the magnesium batteries. In order to analyze the bulk stability of the Mg_3Bi_2 and the Mg_3Sb_2, I performed Rietveld refinement for the Mg_3Bi_2 and the Mg_3Sb_2. The refinements showed different Mg 2*d* site values between the Mg_3Bi_2 and the Mg_3Sb_2. In addition, the bond length of magnesium-bismuth at 2*d* site more longer than that of magnesium-antimony, suggesting that the magnesium cation at 2*d* site is relatively weak interaction with bismuth anion. The MEM analyses were also carried

out to check the electron density distribution of the Mg_3Bi_2 and the Mg_3Sb_2. The electron density distribution sliced at (010) plane of the Mg_3Bi_2 showed low electron density between the magnesium cation and the bismuth anion. It shows that the interaction of the magnesium cation and bismuth anion is weak, compared with the interaction of the magnesium cation and antimony anion. I think that the diffusion of the magnesium cation in the Mg_3Bi_2 is smooth due to the weak interaction of 2*d* site. Therefore, I showed that the activity of the Mg_3Bi_2 and the Mg_3Sb_2 relates to the surface and the bulk stability in the structure. I propose that two prospects of the surface stability and the bulk condition in the structure need to search a candidate of new alloy-based anode active materials in the rechargeable magnesium batteries.

General Conclusion

In this thesis, the author focused on the negative electrode-electrolyte interphases for rechargeable lithium and magnesium batteries. In order to obtain a guideline for the next generation negative electrode materials, the author aim to reveal the relationship between condition of the surface film and electrochemical properties of the lithium and magnesium metal. This thesis is a summary of analytical studies of the surface film on the lithium metal, the magnesium metal, lithium-based and magnesium-based alloy anodes. The author shows the results obtained by this investigation to the following summaries.

The relationship between the SEI layer and the surface morphology of the electrodeposited lithium was examined by XPS spectroscopy and *ex situ* FTIR spectroscopy. In the case of using an additive-free electrolyte solution, the lithium negative electrode maintains a very uniform surface morphology during the initial deposition process. However once the total deposition amount increases, the lithium electrode starts to form agglomerated particles of the dendritic lithium. The electrolyte additives FEC, VC and LiBOB eliminate the dendritic growth of the lithium during the electrodeposition process, suggesting that these additives form stable SEI layer at the surface of the lithium negative electrodes. The surface morphology of the FEC showed the most uniform deposits, while the surface morphology VC and LiBOB formed some agglomerated particles consists of dendritic lithium.

General Conclusion

The XPS spectra of additive-free electrolyte solution showed an SEI layer consists of $LiOCO_2R$ and $Li_xPO_yF_z$. Since the electrolyte containing FEC suppress the decomposition of PF_6^- anion, the FEC containing electrolyte could form a thin and uniform SEI layer resulting in the uniform lithium deposition. The XPS spectra of containing VC and LiBOB demonstrated a polymerized layer at the top of the SEI layer. Rigid SEI layer eliminates the dendritic growth of the lithium, however some agglomerated particles consist of the dendritic lithium, are observed around the edge of the electrode. The author concludes that the electrolyte additives are basically effective to eliminate the dendritic growth of the lithium. Thin and flexible SEI layer is the ideal interphase to avoid the dendritic growth of lithium.

The comparative studies of the electrochemical properties of magnesium metal using the EAC electrolyte solution and the ionic electrolyte solution for rechargeable magnesium batteries were conducted. The EAC electrolyte solution showed relatively low overpotential approximately 0.34 V, while the ionic electrolyte solution showed very high overpotential >1.5 V. The coulombic efficiency of the EAC electrolyte solution and the ionic electrolyte solution were 99.7 % and approximately 60 % respectively. Since the magnesium deposited in the ionic electrolyte solution showed poor crystallinity, the passivated surface of the deposited magnesium via decomposition of the electrolyte solution hinders the smooth crystal growth of the magnesium. The *in situ* FTIR spectra for the EAC electrolyte solution was highly reversible during the CV measurement, suggesting that the surface of the Pt electrode was not passivated. On the other hand,

the *in situ* FTIR spectra for the ionic electrolyte solution showed several peaks only at the 1st cathodic scan and no peaks during the following scans. It shows that the electrode surface is passivated during the 1st cathodic scan. The XPS spectra for the magnesium metal immersed in the ionic electrolyte solution proved that TFSA anion in the ionic electrolyte solution was decomposed at the surface of the magnesium metal, resulting in the formation of MgF_2-based passivation layer. Therefore, the high overpotential of the magnesium deposition / dissolution process in the ionic electrolyte solution is caused by the formation of the passivation layer via decomposition of the TFSA anion.

Investigations of relationship between the SEI layer and the cycling performance of the Bi powder electrode using the $LiPF_6$ electrolyte solution and the $LiBH_4$ electrolyte solution were conducted. The charging-discharging curves of the Bi electrode for Li systems demonstrate the two plateaus corresponding to LiBi phase and Li_3Bi phase. The initial lithium insertion capacity of $LiPF_6$ electrolyte is 410 mAh g^{-1}, the lithium extraction capacity is 330 mAh g^{-1}, whereas the insertion / extraction capacity of $LiBH_4$ electrolyte shows the Bi theoretical capacity of 384 mAh g^{-1}. It is indicated that the $LiBH_4$ electrolyte forms the less SEI layer interphase. At the 1 C rate, the $LiBH_4$ electrolyte solution shows high reversibility of 385 mAh g^{-1} at ten cycles, while the $LiPF_6$ electrolyte has poor cyclability of 77 mAh g^{-1} at ten cycles. The prolonged cycle life is concerned with the surface layer on the Bi electrode, because the $LiBH_4$ electrolyte shows highly reversible capacity at forty-five cycles. The SNIFTIR spectra of the $LiPF_6$ electrolyte mostly had the positive peaks corresponding to the electrolyte, suggesting that

the electrolyte is decomposed at 0.3 V vs. Li/Li^+. In contrast, the SNIFTIR spectra of the $LiBH_4$ electrolyte showed the flipped shape peaks assigned the THF and $LiBH_4$, suggesting that the $LiBH_4$ electrolyte is possible to obtain the less SEI layer interphase. The SEM images of the Bi electrode using the $LiPF_6$ and $LiBH_4$ electrolyte after forty-five cycles demonstrated the similar surface morphologies of the pulverized Bi particles. Therefore, the author showed the suppression of the new SEI layer formation on the Bi particles relates to the prolonged cycle life at high rate.

A comparative study using the same structure of Mg_3Bi_2 and the Mg_3Sb_2 were investigated why the Mg_3Bi_2 shows reversible insertion and extraction of magnesium cation in the conventional electrolyte solution using $Mg(TFSA)_2$. The Mg_3Bi_2 electrode showed high coulombic efficiency of 94.8 % and low overpotential approximately 0.1 V, whereas the Mg_3Sb_2 electrode had low coulombic efficiency of 18.0 % and relatively high overpotential approximately 0.27 V. The author consider that the high electrochemical performance of the Mg_3Bi_2 is affected to the surface stability by passivation layer and the bulk stability of the Mg_3Bi_2 and the Mg_3Sb_2. The XRD patterns of Mg_3Bi_2 exhibited a phase separation to bismuth in air. However, remarkable changes were scarcely observed in the XRD patterns of Mg_3Sb_2. It suggests that the passivation layer is extremely formed at the surface of the Mg_3Bi_2. In order to analyze the bulk condition of structure, the author performed Rietveld refinement for the Mg_3Bi_2 and the Mg_3Sb_2. The refinements showed that the bond length of magnesium-bismuth at *2d* site more longer than that of magnesium-antimony, suggesting that the magnesium cation at *2d* site

is relatively weak interaction with bismuth anion. The electron density distribution sliced at (010) plane of the Mg_3Bi_2 showed low electron density between the magnesium cation and the bismuth anion. It shows that the interaction of the magnesium cation and bismuth anion is weak. The author thinks that the diffusion of the magnesium cation in the Mg_3Bi_2 is smooth due to the weak interaction of *2d* site. Therefore, the author showed that the activity of the Mg_3Bi_2 and the Mg_3Sb_2 relates to the surface stability and the bulk condition in the structure.

To summarize these results, the interphases between the negative electrode and electrolyte solutions were affected by the surface film on the negative electrodes. The condition of surface film is connected with the surface morphologies of the deposited lithium and magnesium anode. The cycling performance of alloy anodes also relate with the surface film. For efficiently reversible reaction, the Li metal needs suppression of the decomposed anion and formation of compact SEI layer which is very thin and smooth Li ion conductivity. The surface condition of the Mg metal is necessary that the passivation layer and the surface film by decomposed anion are hardly formed. In the case of lithium-based alloy, the electrolytes solution of forming less SEI layer is need for good cycling performance because the electrolyte solution forming the SEI layer showed poor cycling performance. The magnesium-based intermetallic compounds need the surface and bulk instability for reversible magnesium insertion/extraction.

Therefore, in order to use metal or alloy-based anodes as next generation anodes for the rechargeable batteries, it is necessary to improve the reductive stability of the

electrolyte solutions. This study could be guided for further improvement of anodes for rechargeable lithium and magnesium batteries, and lithium and magnesium ion batteries.

Reference

[1] 2016 Grobal Warming Prevention Plan.

[2] J. B. Goodenough, K.S. Park, *J. Am. Chem. Soc.*, **135** (2013) 1167-1176.

[3] NEDO Battery Road Map 2013.

[4] J. O. Besenhard, M. Winter, *Chem. Phys. Chem.*, **3** (2002) 155-159.

[5] R. Jasinski, High-Energy Batteries (Plenum Press, New York, 1967).

[6] M.S. Whittingham, *Science*, **192** (1976) 1126-1127.

[7] I. Yoshimatsu, T. Hirai, J. Yamaki, *J. Electrochem. Soc.*, **135** (1988) 2422-2427.

[8] M. Arakawa, S. Tobashima, Y. Nemoto, M. Ichimura, *J. Power Sources*, **43-44** (1993) 27-35.

[9] C. Monroe, J. Newman, *J. Electrochem, Soc.*, **150** (2003) A1377.

[10] C. Ling, D. Banerjee, M. Matsui, *Electrochim. Acta*, **76** (2012) 270-274.

[11] E. Peled, *J. Electrochem.Soc.*, **126** (1979) 2047-2051.

[12] E. Peled, D. Golodnitsky, G. Ardel, *J. Electrochem. Soc.*, **144** (1997) L208-L210.

[13] D. Aurbach, M.L. Daroux, P.W. Faguy, E. Yeager, *J. Electrochem. Soc.* **134** (1987) 1611-1620.

[14] D. Aurbach, M.L. Daroux, P.W. Faguy, E. Yeager, *J. Electrochem. Soc.*, **135** (1988) 1863-1871.

[15] D. Aurbach, O. Chusid, *J. Electrochem. Soc.*, **140** (1993) L1-L4.

[16] D. Aurbach, O. Chusid, *J. Electrochem. Soc.*, **140** (1993) L155-L157.

[17] K. Kanamura, S. Siraishi, H. Tamura, Z. Takehara, *J. Electrochem. Soc.*, **141** (1994) 2379-2385.

[18] K. Kanamura, H. Tamura, S. Shiraishi, Z. Takehara, *J. Electrochem. Soc.*, **142** (1995) 340-347.

[19] Y. M. Lee, J. E. Seo, Y. -G. Lee, S. H. Lee, K. Y. Cho, J. -K. Park, *Electrochem. Solid-State Lett.*, **10** (2007) A216-A219.

[20] Y. S. Cohen, Y. Cohen, D. Aurbach, *J. Phys. Chem. B*, **104** (2000) 12282-12291.

[21] R. Mogi, M. Inaba, S.-K. Jeong, Y. Iriyama, T. Abe, Z. Ogumi, *J. Electrochem. Soc.*, **149** (2002) A1578.

[22] D. Aurbach, Y. Cohen, *J. Electrochem. Soc.*, **144** (1997) 3355-3360.

Reference

[23] D. Aurbach, Y. Cohen, *J. Electrochem. Soc.*, **143** (1996) 3525-3532.

[24] Z. Ogumi, *GS News Technical Reports*, **62** (2003) 2-9.

[25] K. Kanamura, S. Shiraishi, Z. Takehara, *J. Electrochem. Soc.*, **143** (1996) 2187-2197.

[26] H. Ota, Y. Sakata, Y. Otake, K. Shima, M. Ue, J. Yamaki, *J. Electrochem. Soc.*, **151** (2004) A1778.

[27] H. Ota, K. Shima, M. Ue, J. Yamaki, *Electrochim. Acta*, **49** (2004) 565-572.

[28] H. Ota, X. Wang, E. Yasukawa, *J. Electrochem. Soc.*, **151** (2004) A427.

[29] H. Sano, H. Sakaebe, H. Matsumoto, *J. Electrochem. Soc.*, **158** (2011) A316-A321.

[30] F. Ding, W. Xu, G.L. Graff, J. Zhang, M.L. Sushko, X. Chen, Y. Shao, M.H. Engelhard, Z. Nie, J. Xiao, X. Liu, P.V. Sushko, J. Liu, J.G. Zhang, *J. Am. Chem. Soc.*, **135** (2013) 4450-4456.

[31] Y. Zhang, J. Qian, W. Xu, S.M. Russell, X. Chen, E. Nasybulin, P. Bhattacharya, M.H. Engelhard, D. Mei, R. Cao, F. Ding, A.V. Cresce, K. Xu, J.G. Zhang, *Nano Lett.*, **14** (2014) 6889-6896.

[32] H. Wang, M. Matsui, H. Kuwata, H. Sonoki, Y. Matsuda, X. Shang, Y. Takeda, O. Yamamoto, N. Imanishi, *Nat. Commun.*, **8** (2017) 15106.

[33] A. Ponrouch, C. Frontera, F. Barde, M.R. Palacin, *Nat. Mater.*, **15** (2016) 169-172.

[34] M. Matsui, *J. Power Sources*, **196** (2011) 7048-7055.

[35] Z. Lu, A. Schechter, M. Moshkovich, D. Aurbach, *J. Electroanal. Chem.*, **466** (1999) 203-217.

[36] D. Aurbach, I. Weissman, Y. Gofer, E. Levi, *Chem. Rec.*, **3** (2003) 61-73.

[37] L.W. Gaddum, H.E. French, *Electrolysis of grignard solutions*, **49** (1927) 1295-1299.

[38] T. D. Gregory, R. J. Hoffman, R. C. Winterton, *J. Electrochem. Soc.*, **137** (1990) 775-780.

[39] D. Aurbach, A. Schechter, M. Moshkovich, Y. Cohen, *J. Electrochem. Soc.*, **148** (2001) A1004.

[40] D. Aurbach, Z. Lu, A. Schechter, Y. Gofer, H. Gizbar, R. Turgeman, Y. Cohen, M. Moshkovich, E. Levi, *Nature*, **407** (2000) 724-727.

[41] D. Aurbach, Y. Gofer, A. Schechter, O. Chusid, H. Gizbar, Y. Cohen, M. Moshkovich, R. Turgeman, *J. Power Sources*, **97-98** (2001) 269-273.

[42] Y. Gofer, R. Turgeman, H. Cohen, D. Aurbach, *Langmuir*, **19** (2003) 2344-2348.

[43] Y. Vestfried, O. Chusid, Y. Goffer, P. Aped, D. Aurbach, *Organometallics*, **26** (2007) 3130-3137.

[44] D. Aurbach, G.S. Suresh, E. Levi, A. Mitelman, O. Mizrahi, O. Chusid, M. Brunelli, *Adv. Mater.*, **19** (2007) 4260-4267.

[45] O. Mizrahi, N. Amir, E. Pollak, O. Chusid, V. Marks, H. Gottlieb, L. Larush, E. Zinigrad, D. Aurbach, *J. Electrochem. Soc.*, **155** (2008) A103.

[46] H. S. Kim, T. S. Arthur, G. D. Allred, J. Zajicek, J. G. Newman, A. E. Rodnyansky, A. G. Oliver, W. C. Boggess, J. Muldoon, *Nat. Commun.*, **2** (2011) 427.

[47] J. Muldoon, C.B. Bucur, A.G. Oliver, T. Sugimoto, M. Matsui, H.S. Kim, G.D. Allred, J. Zajicek, Y. Kotani, *Energy Environ. Sci.*, **5** (2012) 5941.

[48] S. Yagi, A. Tanaka, Y. Ichikawa, T. Ichitsubo, E. Matsubara, *J. Electrochem. Soc.*, **160** (2013) C83-C88.

[49] R. Mohtadi, M. Matsui, T. S. Arthur, S. J. Hwang, *Angew. Chem. Int. Ed. Engl.*, **51** (2012) 9780-9783.

[50] S. -Y. Ha, Y. -W. Lee, S. W. Woo, B. Koo, J. -S. Kim, J. Cho, K. T. Lee, N. -S. Choi, *ACS Appl. Mater. Interfaces*, **6** (2014) 4063-4073.

[51] Y. Orikasa, T. Masese, Y. Koyama, T. Mori, M. Hattori, K. Yamamoto, T. Okado, Z.D. Huang, T. Minato, C. Tassel, J. Kim, Y. Kobayashi, T. Abe, H. Kageyama, Y. Uchimoto, *Sci. Rep.*, **4** (2014) 5622.

[52] T. Fukutsuka, K. Asaka, A. Inoo, R. Yasui, K. Miyazaki, T. Abe, K. Nishio, Y. Uchimoto, *Chem. Lett.*, **43** (2014) 1788-1790.

[53] J. -M. Tarascon, M. Armand, *Nature*, **414** (2001) 359-367.

[54] R. A. Huggins, *J.Power Sources*, **81-82** (1999) 13-19.

[55] M. Wachtler, M. Winter, J. O. Besenhard, *J. Power Sources*, **105** (2002) 151-160.

[56] D. Fauteux, R. Koksbang, *J. Appl. Electrochem.*, **23** (1993) 1-10.

[57] I. Hauke, S. Machill, D. Rahner, K. Wiesener, *J. Power Sources*, **43-44** (1993) 421-427.

[58] H. Tarui, S. Fujitani, *Materia Japan*, **42** (2003) 631-635.

[59] T. Sakai, in *Battery Handbook*, The Committee of Battery Technology, The Electrochemical Society of Japan Editors, Ohmsha, Tokyo (2010), Chapter 2.

[60] J. Li, R. B. Lewis, J. R. Dahn, *Electrochem. Solid-State Lett.*, **10** (2007) A17-A20.

[61] I. Kovalenko, B. Zdyrko, A. Magasinski, B. Hertzberg, Z. Milicev, R. Burtovyy, I. Luzinov, G. Yushin, *Science*, **334**, (2011) 75-79.

[62] M. H. Ryou, J. Kim, I. Lee, S. Kim, Y. K. Jeong, S. Hong, J. H. Ryu, T. S. Kim,

J. K. Park, H. Lee, J. W. Choi, *Adv. Mater.*, **25** (2013) 1571-1576.

[63] H. S. Yang, S. H. Kim, A. G. Kannan, S. K. Kim, C. Park, D. W. Kim, *Langmuir*, **32** (2016) 3300-3307.

[64] C. K. Chan, H. Peng, G. Liu, K. McIlwrath, X. F. Zhang, R. A. Huggins, Y. Cui, *Nat. Nanotech.*, **3** (2008) 31-35.

[65] L.-F. Cui, R. Ruffo, C. K. Chan, H. Peng, Y. Cui, *Nano Lett.*, **9** (2009) 491-495.

[66] H. Kim, M. Seo, M. H. Park, J. Cho, *Angew. Chem. Int. Ed. Engl.*, **49** (2010) 2146-2149.

[67] N.-S. Choi, K. H. Yew, K. Y. Lee, M. Sung, H. Kim, S.-S. Kim, *J. Power Sources*, **161** (2006) 1254-1259.

[68] L. Chen, K. Wang, X. Xie and J. Xie, *J. Power Sources*, **174** (2007) 538-543.

[69] C. K. Chan, R. Ruffo, S. S. Hong, Y. Cui, *J. Power Sources*, **189** (2009) 1132-1140.

[70] B. Philippe, R. Dedryvère, J. Allouche, F. Lindgren, M. Gorgoi, H. Rensmo, D. Gonbeau, K. Edström, *Chem. Mater.*, **24** (2012) 1107-1115.

[71] B. Philippe, R. Dedryvere, M. Gorgoi, H. Rensmo, D. Gonbeau, K. Edstrom, *J. Am. Chem. Soc.*, **135** (2013) 9829-9842.

[72] M. Nie, D. P. Abraham, Y. Chen, A. Bose, B. L. Lucht, *J. Phys. Chem. C*, **117** (2013) 13403-13412.

[73] T. S. Arthur, N. Singh, M. Matsui, *Electrochem. Commun.,* **16** (2012) 103-106.

[74] N. Singh, T. S. Arthur, C. Ling, M. Matsui, F. Mizuno, *Chem. Commun.*, **49** (2013) 149-151.

[75] K. Periyapperuma, T. T. Tran, M. I. Purcell, M. N. Obrovac, *Electrochim. Acta*, **165** (2015) 162-165.

[76] M. Winter, J. O. Besenhard, M. E. Spahr, P. Novak, *Adv. Mater.*, **10** (1998) 725-763.

[77] P. Verma, P. Maire, P. Novák, *Electrochim. Acta*, **55** (2010) 6332-6341.

[78] K. Ushirogata, K. Sodeyama, Y. Okuno, Y. Tateyama, *J. Am. Chem. Soc.*, **135** (2013) 11967-11974.

[79] K. Xu, U. Lee, S.S. Zhang, M. Wood, T.R. Jow, *Electrochem. Solid-State Lett.*, **6** (2003) A144-A148.

[80] A. Benmayza, M. Ramanathan, T. S. Arthur, M. Matsui, F. Mizuno, J. Guo, P. -A. Glans, J. Prakash, *J.Phys. Chem. C*, **117** (2013) 26881-26888.

[81] A. W. Hull, *Physical Review*, **10** (1917) 661-696.

[82] B. D. Culity, *Elements of X-ray Diffraction,* Addison Wesley Pub., Reading, Massachusetts, (1978).

[83] D. Aurbach, R. Turgeman, O. Chusid, Y. Gofer, *Electrochem. Commun.*, **3** (2001) 252-261.

[84] D. N. Karimov, N. I. Sorokin, S. P. Chernov, B. P. Sobolev, *Crystallogr. Rep.*, **59** (2014) 928-932.

[85] O. Tutusaus, R. Mohtadi, T. S. Arthur, F. Mizuno, E. G. Nelson, Y. V. Sevryugina, *Angew. Chem. Int. Ed. Engl.*, **54** (2015) 7900-7904.

[86] H. Kuwata, M. Matsui, N. Imanishi, *J. Electrochem. Soc.*, **164** (2017) A3229-A3236.

[87] M. Matsui, S. Deguchi, H. Kuwata, N. Imanishi, *Electrochemistry*, **83** (2015) 874-878.

[88] K. B. Harvey,N. R. Mcquaker, *Canad. J. Chem.*, **49** (1971) 3282-3286.

List of Publication

Chapter 1

"Surface Layer and Morphology of lithium Metal Electrodes"

Hiroko Kuwata, Hidetoshi Sonoki, Masaki Matsui, Yasuaki Matsuda, and Nobuyuki Imanishi

Electrochemistry, **84(11)** 854-860 (2016).

Chapter 2

"Passivation Layer Formation of Magnesium Metal Negative Electrodes for Rechargeable Magnesium Batteries"

Hiroko Kuwata, Masaki Matsui, and Nobuyuki Imanishi

Journal of The Electrochemical Society, **164**(13) A3229-A3236 (2017).

Chapter 3

"Improved Cycling Performance of Intermetallic Anode by Minimized SEI Layer Formation"

Hiroko Kuwata, Masaki Matsui, Hidetoshi Sonoki, Yusuke Manabe, Nobuyuki Imanishi and Minoru Mizuhata

To be submitted for publication

Chapter 4

"Surface and Bulk Instability of Magnesium-based Intermetallic Anode for Improved Reversibility"

Hiroko Kuwata, Masaki Matsui, Masatsugu Yamauchi, Daisuke Mori, Nobuyuki Imanishi and Minoru Mizuhata

To be submitted for publication

Acknowledgement

The present studies have been performed under Professor Nobuyuki Imanishi, Mie University, and Associate Professor Masaki Matsui, Kobe University.

The author would like to express my sincerest gratitude to Professor Nobuyuki Imanishi for his helpful advice and encouragement on publishing the thesis. The author is grateful to Professor Masataka Kubo, Professor Satoshi Kaneco and Associate Professor Daisuke Mori for advice and suggestions of this thesis. Professor Osamu Yamamoto and Professor Yasuo Takeda give me technical assistance and helpful comments. The author would like to offer my thanks to Professor Minoru Mizuhata, Kobe University, for giving me opportunity to research at Kobe University and useful advice. The author would like to express the deepest appreciation to Associate Professor Masaki Matsui, Kobe University, for his polite guidance, considerable supports and encouragement. The author has had the support of Associate Professor Hideyuki Horino, Mr. Takayuki Ichikawa and Ms. Kayo Nishikawa.

The author would like to show my appreciation to Dr. Takuya Masuda, National Institute for Materials Science, for hard X-ray photoemission spectroscopic measurement. Dr. Aiko Nakao, Institute of Physical and Chemical Research, has been greatly supported for X-ray photoelectron spectroscopic measurement.

Finally, the author would like to thank laboratory members of Imanishi group and Mizuhata group for their assistance.

Hiroko Kuwata